# MAGNETIC FIELD-INDUCED PHASE TRANSFORMATION AND VARIANT REORIENTATION IN $Ni_2MnGa$ AND NiMnCoIn MAGNETIC SHAPE MEMORY ALLOYS

A Dissertation

by

HALUK ERSIN KARACA

Submitted to the Office of Graduate Studies of
Texas A&M University
in partial fulfillment of the requirements for the degree of

DOCTOR OF PHILOSOPHY

August 2007

Major Subject: Mechanical Engineering

# MAGNETIC FIELD-INDUCED PHASE TRANSFORMATION AND VARIANT REORIENTATION IN $Ni_2MnGa$ AND NiMnCoIn MAGNETIC SHAPE MEMORY ALLOYS

A Dissertation

by

HALUK ERSIN KARACA

Submitted to the Office of Graduate Studies of
Texas A&M University
in partial fulfillment of the requirements for the degree of

DOCTOR OF PHILOSOPHY

Approved by:

| | |
|---|---|
| Chair of Committee, | Ibrahim Karaman |
| Committee Members, | Dimitris C. Lagoudas |
| | K. Ted Hartwig |
| | Xinghang Zhang |
| Head of Department, | Dennis L. O'Neal |

August 2007

Major Subject: Mechanical Engineering

# ABSTRACT

Magnetic Field-Induced Phase Transformation and Variant Reorientation in $Ni_2MnGa$ and NiMnCoIn Magnetic Shape Memory Alloys. (August 2007)

Haluk Ersin Karaca, B.S., Bogazici University;

M.S., Texas A&M University

Chair of Advisory Committee: Dr. Ibrahim Karaman

The purpose of this work is to reveal the governing mechanisms responsible for the magnetic field-induced i) martensite reorientation in $Ni_2MnGa$ single crystals, ii) stress-assisted phase transformation in $Ni_2MnGa$ single crystals and iii) phase transformation in NiMnCoIn alloys. The ultimate goal of utilizing these mechanisms is to increase the actuation stress levels in magnetic shape memory alloys (MSMAs). Extensive experimental work on magneto-thermo-mechanical (MTM) characterization of these materials enabled us to i) better understand the ways to increase the actuation stress and strain and decrease the required magnetic field for actuation in MSMAs, ii) determine the effects of main MTM parameters on reversible magnetic field induced phase transformation, such as magnetocrystalline anisotropy energy (MAE), Zeeman energy (ZE), stress hysteresis, thermal hysteresis, critical stress for the stress induced phase transformation and crystal orientation, iii) find out the feasibility of employing polycrystal MSMAs, and iv) formulate a thermodynamical framework to capture the energetics of magnetic field-induced phase transformations in MSMAs.

Magnetic shape memory properties of $Ni_2MnGa$ single crystals were characterized by monitoring magnetic field-induced strain (MFIS) as a function of compressive stress and stress-induced strain as a function of magnetic field. It is revealed that the selection of the operating temperature with respect to martensite start and Curie temperatures is critical in optimizing actuator performance. The actuation

stress of 5 MPa and work output of 157 $kJm^{-3}$ are obtained by the field-induced variant reorientation in NiMnGa alloys.

Reversible and one-way stress-assisted field-induced phase transformations are observed in $Ni_2MnGa$ single crystals under low field magnitudes (<0.7T) and resulted in at least an order of magnitude higher actuation stress levels. It is very promising to provide higher work output levels and operating temperatures than variant reorientation mechanisms in NiMnGa alloys. Reversible field-induced phase transformation and shape memory characteristics of NiMnCoIn single crystals are also studied. Reversible field-induced phase transformation is observed only under high magnetic fields (>4T). Necessary magnetic and mechanical conditions, and materials design and selection guidelines are proposed to search for field-induced phase transformation in other ferromagnetic materials that undergo thermoelastic martensitic phase transformation.

TO
MY FAMILY
AND
HAYRIYE

# ACKNOWLEDGEMENTS

First of all, I sincerely thank and extend my deepest gratitude to my advisor, Prof. Ibrahim Karaman, who gave life to this project, and without his endless encouragement and support this project would not have been completed. Not only did he help me in every aspect of this project but also made me a better person, scientist, and engineer by setting high standards and being an example.

I would like to thank my committee member, Prof. Dimitris Lagoudas for his guidance on how to be a good academician and for offering useful discussions throughout my graduate studies. I am also thankful to Prof. Ted Hartwig and Prof. Xinghang Zhang, for being on my committee and for their invaluable advice.

I express my gratitude to Prof. Yuriy Chumlyakov for his very helpful suggestions and guidance, sharing his deep knowledge on shape memory alloys and providing us with the single crystals used in this study. I also thank him for his hospitality during my Russia trip. Special thanks go to Dr. Hans Maier and his students for their fruitful collaboration on my research. I would like to appreciate the help I received from Dr. Yang Ren on synchrotron high energy X-ray measurements and their analysis.

My years at Texas A&M would certainly not have been the same without the wonderful group of people I have had the opportunity to work with. I would like to thank my officemates and colleagues; Burak Basaran, Dr. Guney Yapici, Benat Kockar, Andrew Brewer, Dr. Mohammed Haouaoui, Joseph Mather, Bryan Bagley, Yang Cao, James Monroe, Hans-Gerd Lambers, Dr. Suveen Mathaudhu and Osman Anderoglu for providing a good environment, both academic and social. Mr. Burak Basaran is specially thanked for his contributions in this research project and his great friendship. We spent days and nights to fix and build the experimental setup and perform experiments.

I would also like to thank Ferdi Karadas, Dr. Mert and Selma Atilhan, Dr. Fatih Mutlu, Serkan Ozel, Hamza Anderoglu, Suleyman Ciftci, Orkun Toros, Ziya Gur, Renat

Schaykutdinov, Dr. Kerem Cakirer, Yildirim and Gokcen Dogan and many others for their wonderful friendship that made my life in Texas so enjoyable. Special thanks to my soccer teammates, especially to the ones in our “Legendary” Kaisers, Istanbull and Galatasaray teams; that we have became champions so many times in intramural tournaments, mini world cups and BCS Soccer League. I also thank my old friends, Necdet Tek, Harun Kurkcu, Davut Otar, Aydin Buyukhelvaci and Harun Asa for their long-lasting friendship.

Last but not least, I would like to thank my parents, Muzaffer and Seyide Karaca for their continuous love and support. They sacrificed a lot for me and my brother. Their strong motivation and endless trust are the reasons for my success in every aspect of my life. Also, my brother, Erdem Karaca, and his wife, Zekiye Karaca, are thanked for always being one step ahead of me, sharing their invaluable experience, and simply, always being there when I needed them. I also thank Miss Hayriye Cetin for her friendship, love, support and encouragement in the concluding stage of my graduate study.

# TABLE OF CONTENTS

Page

ABSTRACT ..... iii

DEDICATION ..... v

ACKNOWLEDGEMENTS ..... vi

TABLE OF CONTENTS ..... viii

LIST OF FIGURES ..... x

LIST OF TABLES ..... xvii

CHAPTER

I INTRODUCTION ..... 1

1.1 Motivation and Objectives ..... 1
1.2 Active Materials ..... 4
1.3 Fundamental Magnetics Background ..... 9
1.4 Magnetocrystalline Anisotropy Energy ..... 12
1.5 Magnetic Domains ..... 15
1.6 Magnetic Shape Memory Alloys ..... 17
1.6.1 Magnetic Field-Induced Variant Reorientation ..... 17
1.6.2 Magnetic Field-Induced Phase Transformation ..... 19
1.6.3 Stress-Assisted Magnetic Field-Induced Phase Transformation in MSMAs ..... 20
1.7 Brief History and Crystal Structures of NiMnGa ..... 21
1.8 Brief History and Crystal Structures of NiMnCoIn ..... 25

II EXPERIMENTAL PROCEDURES ..... 27

III MAGNETIC FIELD-INDUCED MARTENSITE REORIENTATION IN $Ni_2MnGa$ ALLOYS ..... 33

3.1 Magnetization Results ..... 33
3.2 Conventional Shape Memory Effect ..... 36
3.3 Magnetic Field-Induced Strain by Variant Reorientation under Constant Stress ..... 37
3.4 Strain Response under Incremental Magnetic Field ..... 44
3.5 Magneto-Microstructural Mechanisms for Variant Reorientation ..... 47
3.6 Effect of Magnetic Field Rate on Magnetic Field-Induced Strain ..... 51
3.7 Stress-Induced Martensite Reorientation under Constant Magnetic Field ..... 53

CHAPTER Page

IV STRESS-ASSISTED FIELD-INDUCED PHASE TRANSFORMATION IN $Ni_2MnGa$ SINGLE CRYSTALS ..... 58

4.1 Pseudoelastic Response ..... 58
4.2 Isobaric Thermal Cycling ..... 59
4.3 Stress-Temperature Phase Diagram ..... 62
4.4 Effect of Magnetic Field on Pseudoelasticity Response ..... 64
4.5 Magnetic Field-Induced Phase Transformation for the First Stage Transformation ..... 67
4.6 Magnetic Field-Induced Phase Transformation for the Second Stage Transformation ..... 72
4.7 Magneto-Microstructural Mechanisms for Magnetic Field-Induced Phase Transformation ..... 75
4.8 Mechanical Conditions for Reversible and One-Way Field-Induced Phase Transformation ..... 78
4.9 Effect of MAE on Phase Transformations in NiMnGa Alloys ..... 82
4.10 Actuation Stress and Work Output ..... 90

V PHASE TRANSFORMATION IN NiMnCoIn ALLOYS ..... 93

5.1 Magnetization Results ..... 93
5.2 Effect of Magnetic Field on the Pseudoelastic Response of NiMnCoIn Alloys ..... 102
5.3 Synchrotron X-ray Results ..... 105
5.4 Theoretical Transformation Strain and Detwinning Strain in NiMnCoIn Alloys ..... 109
5.5 Prediction of Magnetostress in NiMnCoIn Alloys ..... 113
5.6 Optical Microscopy and Compositional Analysis of NiMnCoIn Alloys 115

VI A THERMODYNAMICAL FRAMEWORK FOR MAGNETIC FIELD-INDUCED PHASE TRANSFORMATION ..... 119

VII SUMMARY AND CONCLUSIONS ..... 131

REFERENCES ..... 135

VITA ..... 141

# LIST OF FIGURES


Page

Figure 1.1 Shape memory and two-way shape memory effect in shape memory alloys ..... 8

Figure 1.2 Demonstration of the magnetic moment associated with (a) an orbiting electron and (b) a spinning electron ..... 10

Figure 1.3 The magnetization versus applied magnetic field response along the [100], [110] and [111] orientations of iron (bcc) and nickel ..... 13

Figure 1.4 Magnetization versus applied field responses of three martensite structures of NiMnGa alloys along the a, b and c axes ..... 15

Figure 1.5 Domain structures of NiMnGa alloys determined using a) the magnetic garnet film technique and b) scanning electron microscopy images ..... 16

Figure 1.6 Effect of applied magnetic field, H, a) on the reorientation of the martensite twin variants and b) on phase transformation in MSMAs ..... 18

Figure 1.7 Stress-induced phase transformation and variant reorientation response of $Ni_2MnGa$ single crystal of the present work at -40 and -90 ˚C, respectively ..... 22

Figure 1.8 $L2_1$ structure of NiMnGa alloy ..... 23

Figure 2.1 Schematic of the magneto-thermo-mechanical setup with an electromagnet and a capacitive displacement sensor used in this study ..... 29

Figure 2.2 A picture of magneto-thermo-mechanical experimental test setup ..... 30

Figure 2.3 A plot of the representative data obtained during the magneto-thermo-mechanical experiments. The stress is applied and kept constant, temperature is kept constant, magnetic field is ramped and the strain response is measured ..... 31

Figure 3.1 Magnetization as a function of temperature under magnetic field of 200 Gauss, as well as its derivative showing the transformation temperatures for the parent to I-phase to 10M martensite transformation sequence ..... 34

Figure 3.2 a) Evolution of magnetization as a function of temperature under constant magnetic fields of 200 G, 500 G and 10 000 G. b) Change in magnetization with applied magnetic field at -125 °C and 25 °C in fully martensitic and austenitic phases, respectively ..... 35

Page

Figure 3.3 Cooling-heating response of $Ni_{51.1}Mn_{24.0}Ga_{24.9}$ single crystal under a compressive load of 10 MPa along the [100] orientation..... 36

Figure 3.4 Evolution of strain in the $Ni_{51.1}Mn_{24.0}Ga_{24.9}$ single crystals as a function of magnetic field under different constant compressive stress levels at -95 $^{o}$C. Three cycles are shown. a) Increased stress levels from 2 to 6 MPa, b) decreased stress levels from 5 MPa to 1 MPa. Only selected cases are shown for clarity ..... 39

Figure 3.5 Magnetic field-induced strain response during the a) first and b) second magnetic field cycles under constant stress levels ..... 41

Figure 3.6 Comparison of maximum MFIS as a function of stress for the current study and literature data. A grid of constant actuation work output hyperbolas ranging from 10 to 180 $kJm^{-3}$ has been superimposed..... 43

Figure 3.7 Two schematics to identify the blocking stress levels for two cases with the same $T_c$ but different $M_s$ and operating temperatures: a) $M_s$ temperature is high and b) $M_s$ temperature is low, $T_o$ is kept close to $M_s$..... 45

Figure 3.8 Incremental applied magnetic field experiment results under constant stress of 3 MPa. a) MFIS response with applied magnetic field magnitude increased from 2 kG to 16 kG with increments of 2 kG. Maximum and irrevocable strain levels are shown on the right column, b) MFIS (left) and applied magnetic field (right) responses with time..... 46

Figure 3.9 A schematic of the magneto- and microstructural mechanisms for variant reorientation mechanism in MSMAs ..... 48

Figure 3.10 a) Effect of magnetic field rate on the MFIS evolution under 3 MPa showing two-stage reorientation, b) maximum and first stage MFIS magnitudes as a function of field rate..... 52

Figure 3.11 MFIS response of the $Ni_{51.1}Mn_{24.0}Ga_{24.9}$ single crystals under 2 MPa constant stress with magnetic field rate of 50 G/sec showing two step reorientation behavior in detail ..... 54

Figure 3.12 Effect of magnetic field on the stress-strain response the $Ni_{51.1}Mn_{24.0}Ga_{24.9}$ single crystals during martensite reorientation. The test temperature was -95 °C ..... 54

Figure 3.13 Stress-strain response of the $Ni_{51.1}Mn_{24.0}Ga_{24.9}$ single crystals under a constant magnetic field of 16 kG at -95 °C. The loading was interrupted at selected strain levels for better understanding of strain and hysteresis evolution ..... 57

Page

Figure 3.14 Magnetostress as a function of applied magnetic field for NiMnGa single crystals with different martensite modulation. ..... 57

Figure 4.1 Schematics of reversible martensitic phase transformation upon cycling (a) temperature in conventional shape memory alloys and (b) magnetic field in magnetic shape memory alloys due to field-induced phase transformation. In both cases the stress is kept constant during the phase transformation..... 60

Figure 4.2 Pseudoelastic response of $Ni_{51.1}Mn_{24.0}Ga_{24.9}$ single crystals as a function of temperature under compression along the [100] orientation. The critical stress for inducing transformation increases with temperature for the second stage while it decreases for the first stage ..... 61

Figure 4.3 Thermal cycling response under a compressive stress of 20 MPa illustrating the parent phase to X-phase to I-phase to 10M martensite transformation sequence in detail ..... 62

Figure 4.4 Stress-temperature diagram for $Ni_{51.1}Mn_{24.0}Ga_{24.9}$ illustrating the multiple phase transformations ..... 63

Figure 4.5 Effect of magnetic field on the pseudoelastic response of the $Ni_{51.1}Mn_{24.0}Ga_{24.9}$ single crystals at -70 ˚C. The critical stress levels for inducing the phase transformation increase with field up to a certain level and saturate at higher fields. The inset shows the change in the critical stresses with applied magnetic field for the first and second stages. ..... 65

Figure 4.6 Pseudoelastic response of $Ni_{51.1}Mn_{24.0}Ga_{24.9}$ single crystals as a function of temperature and magnetic field under compression along the [100] orientation. $\sigma_c$: Critical stress for the onset of phase transformation ..... 67

Figure 4.7 (a) The pseudoelastic response of $Ni_{51.1}Mn_{24.0}Ga_{24.9}$ at -60 ˚C under zero (solid lines) and 1.6 T applied magnetic field (dotted lines), (b) Temperature dependence of the critical stress levels and stress hysteresis during the first stage transformation with and without magnetic field. ..... 69

Page

Figure 4.8 Demonstration of the stress-assisted reversible (cyclic) field-induced phase transformation at low field magnitudes at -55 ˚C. Data in (a) and (b) are from the same experiments. The number sequence demonstrates the loading path ..... 71

Figure 4.9 Demonstration of the reversible (cyclic) field-induced phase transformation at low field magnitudes in $Ni_{51.1}Mn_{24.0}Ga_{24.9}$ single crystals at -50 °C, a) stress vs. strain and b) corresponding strain vs. magnetic field response ..... 73

Figure 4.10 Demonstration of the field-induced one-way shape memory effect via X to 10M martensitic transformation or vice versa at low field magnitudes. Data in (a) and (b) are from the same experiments. The number sequence demonstrates the loading path ..... 74

Figure 4.11 Schematics of the reversible magnetic field-induced phase transformation under a constant stress level. (a) Stress vs. strain and (b) corresponding strain vs. magnetic field response ..... 76

Figure 4.12 Schematic of the magnetic field-induced forward and reverse phase transformation under different constant stress levels. (a) stress vs. strain and (b) corresponding strain vs. magnetic field response ..... 79

Figure 4.13 a) Actuation stress ranges for the reversible and one-way field-induced phase transformations in between I-phase and X-phase as a function of temperature. (b) Stress hysteresis and magnetostress in the second stage phase transformation as a function of temperature. The figure is divided into three regions depending on the type of the parent phase as X→10M, I→10M and P→10M phase transformation regions ..... 81

Figure 4.14 Two schematics showing two different paths to induce austenite to single variant and magnetic domain martensite phase transformation. (a) Magnetic field is applied prior to the stress loading, (b) magnetic field is applied after stress induced phase transformation ..... 84

Figure 4.15 A schematic to explain effect of magnetic field on the phase transformation of MSMA polycrystals with a) ferromagnetic and b) paramagnetic austenite phase ..... 85

Page

Figure 4.16 Effect of magnetic field on a single crystal in three different configurations, (a) austenite and martensite are ferromagnetic and field is applied parallel to compressive stress, (b) austenite is paramagnetic, martensite is ferromagnetic and field is applied parallel to compressive stress, (c) austenite is paramagnetic, martensite is ferromagnetic and field is applied perpendicular to compressive stress ..... 88

Figure 4.17 MFIS and total work output vs. the actuation stress plots showing the literature data obtained to date utilizing field-induced martensite reorientation mechanism and the present results of field-induced reversible and irreversible phase transformations in NiMnGa MSMAs. The figure also shows a region of MFIS, actuation stress and work output that might possibly be achieved utilizing the simple guidelines introduced here and optimizing the suggested parameters. A grid of constant mechanical work output hyperbolas ranging from 2 and 2000 $kJm^{-3}$ has been superimposed. Logarithmic scale is used for both axes for easy comparison ..... 92

Figure 5.1 The change in magnetization with temperature under constant applied magnetic field of 500 Oe for the as-cast polycrystal, as-grown single crystal and heat-treated single crystal of $Ni_{45.7}Mn_{35.6}Co_{4.8}In_{13.8}$ alloy. The decrease and increase in magnetization during cooling and heating indicate forward and reverse transformations respectively. The Curie temperature is 390 K ..... 94

Figure 5.2 Magnetization as a function of temperature under 0.05 T and its temperature derivative for NiMnCoIn, a) batch 1 and b) batch 2 single crystals. Each batch has grown with the same initial nominal composition of 45Ni-36.5Mn-5Co-13.5In (in at. %) ..... 95

Figure 5.3 Change in magnetization of batch 2 $Ni_{45.7}Mn_{35.6}Co_{4.8}In_{13.8}$ single crystal as a function of a) temperature under constant applied magnetic field and b) as applied magnetic field at 140 K and 220 K ..... 97

Figure 5.4 Change in magnetization of batch 1 $Ni_{45.7}Mn_{35.6}Co_{4.8}In_{13.8}$ single crystals as a function of a) temperature under constant applied magnetic field and b) applied magnetic field at 50, 150, 200 and 220 K, and c) magnetization versus temperature curves for the data shown in (b) where the fields are ramped after cooling down to set temperatures under 0.05T ..... 98

Page

Figure 5.5 Change in magnetization of batch 1 $Ni_{45.7}Mn_{35.6}Co_{4.8}In_{13.8}$ single crystal as a function of a) temperature and b) applied magnetic field. Sample is cooled down from 300 K to 50 K. The number sequence demonstrates the loading path ..... 101

Figure 5.6 Pseudoelastic response under compression along the [100] orientation of the $Ni_{45.7}Mn_{35.6}Co_{4.8}In_{13.8}$ batch 2 single crystal at 0, 20 and 50 ˚C ..... 102

Figure 5.7 Effect of magnetic field on the pseudoelastic response and the critical stress for the field-induced phase transformation of $Ni_{45.7}Mn_{35.6}Co_{4.8}In_{13.8}$ [100](011) batch 2 single crystal at 0 ˚C ..... 103

Figure 5.8 Magnetostress as a function of magnetic field for the $Ni_{45.7}Mn_{35.6}Co_{4.8}In_{13.8}$ [100](011) batch 2 single crystal determined at 4% strain from the curves shown in Figure 5.7. The sample exhibits ~30 MPa magnetostress under 1.6T magnetic field ..... 104

Figure 5.9 a) The diffraction image plate and b) the corresponding 2-D intensity versus 2θ graph of the $Ni_{45.7}Mn_{35.6}Co_{4.8}In_{13.8}$ single crystal at 300 K. The crystal structure is determined to be $L2_1$ ..... 105

Figure 5.10 a) The diffraction image plate and b) the corresponding 2-D intensity versus 2θ graph of the $Ni_{45.7}Mn_{35.6}Co_{4.8}In_{13.8}$ single crystal at 180 K. The crystal structure determined to be 12M where the modulations are marked..... 106

Figure 5.11 2-D intensity versus 2θ plots of the $Ni_{45.7}Mn_{35.6}Co_{4.8}In_{13.8}$ single crystals between 200 K and 300 K during a) cooling and b) heating under no magnetic field ..... 107

Figure 5.12 2-D intensity versus 2θ plots of $Ni_{45.7}Mn_{35.6}Co_{4.8}In_{13.8}$ single crystals at 200 K a) magnetic field is applied from 0 T to 7 T and b) field is unloaded from 7 T to 0 T with 1 T intervals..... 108

Figure 5.13 Twin (n) and habit (m) planes, and twin shear (a) and macroscopic shear (b) of martensite..... 110

Figure 5.14 Optical micrograph of the heat treated $Ni_{45.7}Mn_{35.6}Co_{4.8}In_{13.8}$ [100](110) single crystal. Formation of second phase is evident..... 117

Figure 5.15 Electron back scattering image of the NiMnCoIn [100](110) heat treated single crystal..... 118

Figure 6.1 The chemical free energies of austenite and martensite phase as a function of temperature. Gibbs free energy curves are presented straight by assuming $\Delta H$ and $\Delta S$ are independent of temperature..... 120

Page

Figure 6.2 Schematics of possible magnetization vs. applied magnetic field responses and illustration of available magnetic energy contributions for four possible cases in magnetic shape memory alloys, a) martensite variant reorientation as in NiMnGa, b) field-induced phase transformation as in NiMnCoIn alloys, c) stress-assisted field-induced phase transformation as in the present NiMnGa alloys, and d) a more general case for field-induced phase transformation between two phases with different saturation magnetizations and magnetocrystalline anisotropy energies ..... 124

Figure 6.3 Gibbs free energy curves of parent and martensite phases of NiMnGa alloy as a function of temperature considering the effect of magnetic energy contributions ..... 125

Figure 6.4 Gibbs free energy curves of parent and martensite phases of NiMnCoIn alloy as a function of temperature considering the effect of magnetic energy contributions ..... 129

# LIST OF TABLES

Page

Table 1.1 Comparison of actuation strain, stress and operating frequencies of active materials. PT: phase transformation ..... 9

Table 1.2 Summary of lattice parameters, cell volume, transformation strain, detwinning stress, MAE and MFIS of three types of martensite structures. In the table 5M, T and 7M stand for 10M, non-modulated and 14M martensitic structures ..... 14

Table 2.1 Text matrix showing the possible experiments that could be performed using the magneto-thermo-mechanical setup shown in Figure 2.2 and their targeted outputs. MFI: magnetic field induced, MFIPT: magnetic field induced phase transformation..... 32

Table 5.1 Volume fraction, habit plane, transformation shear and twinning direction for $Ni_{45.7}Mn_{35.6}Co_{4.8}In_{13.8}$ single crystals determined by energy minimization method..... 112

Table 5.2 Comparison of experimentally observed and theoretically calculated phase transformation strains for $Ni_{45.7}Mn_{35.6}Co_{4.8}In_{13.8}$ single crystals along the three orientations ..... 112

Table 5.3 Orientation dependence of magnetostress as a function of applied field. * indicates the experimental values where all others are theoretical values..... 114

# CHAPTER I

# INTRODUCTION

## 1.1 Motivation and Objectives

Shape memory alloys with ferromagnetic austenite and/or martensite phases are called as ferromagnetic shape memory alloys (FSMA). If an external shape change is triggered when magnetic field is applied due to the structural mechanism other than magnetostriction, the term "magnetic shape memory alloys" term is used for this class of FSMA alloys. MSMAs have attracted an increasing interest due to their unique actuation, sensing and power generation capabilities [1-4]. They offer the possibility of both large actuation strains, comparable to those of conventional SMAs and response frequencies in the kHz regime [2, 3]. MSMAs are strong candidates for actuator and sensor applications since magnetic energy can be converted efficiently to mechanical energy or vice a versa. The ability to produce a few percent field induced strains at frequencies on the order of 1 kHz [4] makes MSMAs suitable for a wide range of applications.

For actuation applications, an ideal MSMA must have the following properties:

1. High actuation stress
2. High actuation strain
3. Low required magnetic field for actuation
4. High operating temperature and range
5. High frequency response
6. Low cost

The main goal of this study is to improve the actuation properties of FSMAs for an ideal MSMA actuator by introducing a new actuation mechanism or utilizing the existing one, and develop certain materials selection guidelines to achieve high actuation stress and operating temperature, and more specifically; to increase actuation stress and maximum

---

This dissertation follows the style and format of Acta Materialia.

operating temperature in NiMnGa alloys and determine the potential of NiMnCoIn alloys as actuators, decrease the required magnetic field for actuation and investigate the possible use of polycrystals of NiMnCoIn alloys.

The most commonly observed magnetic field induced strain is based on the rearrangement of martensite variants by detwinning upon magnetic field application [5-8]. $Ni_2MnGa$ alloys can produce strains up to 10%, require low magnetic field for actuation and its frequency range is in the kHz regime, however, it is very brittle, high strains can only be observed in single crystals, its maximum operating temperature is limited by transformation temperatures and most importantly, has very low actuation stress level (<2 MPa).

One of the main objectives of this study is to reveal the governing material parameters that are critical for increasing the actuation stress levels using martensite variant reorientation mechanism in $Ni_2MnGa$ alloys. In order to observe MFIS by variant reorientation, there are two major requirements: low stress for detwinning and high MAE which are also among the determining factors for the actuation stress magnitudes. Generally, for MSMAs, the detwinning stress is very low as compared to the stress required for dislocation slip. Low detwinning stress can be achieved by compositional adjustments and modifications to the martensite structure, i.e. modulation [9, 10]. In principal, the MAE can be increased by increasing the saturation magnetization and Curie temperature ($T_c$). It is reported that Curie temperature of NiMnGa alloys is around 50-100 ˚C [11, 12] and saturation magnetization is a weak function of composition [13]. The easiest way to increase the MAE is then to choose an operating temperature ($T_o$) significantly lower than $T_c$ since the MAE increases with decreasing temperature below $T_c$, i.e. with increasing $T_c - T_o$. However, detwinning stress also increases with decreasing temperature below transformation temperatures. Therefore, it is critical to understand and quantify the relationship between MAE, detwinning stress, $T_o$, $T_c$ and transformation temperatures to select materials and operating temperatures for obtaining high blocking and magnetostress.

In many studies, the MFIS response was reported only during the first magnetic field loading-unloading cycle since the goal has been the maximization of the MFIS. However, it is important to capture the degree of irrecoverable strain during cyclic field loading as a function of stress for practical applications and understanding the governing mechanisms. In this study, both first cycle (magnetoplasticity response) and higher number of cyclic response of NiMnGa single crystals are investigated as a function of stress and magnetic field.

Variant reorientation mechanism can only be observed at temperatures lower than the transformation temperatures. In shape memory alloys (SMAs), it is possible to induce phase transformation by temperature and stress. In this study, instead of temperature, magnetic field induced phase transformation under constant applied stress will be investigated in NiMnGa alloys as a new actuation mechanism for MSMAs. Conditions for reversible and one-way stress-assisted field-induced phase transformations in NiMnGa alloys and the actuation and work output levels by this new mechanism will be revealed. Possible magneto-microstructural mechanisms and necessary magnetic and mechanical conditions to accomplish field-induced phase transformation will be discussed.

High MFIS is observed only in single crystals of NiMnGa alloys since the main source of available magnetic energy is MAE and polycrystals of NiMnGa alloys are very brittle. Moreover, MAE is orientation dependent and after reaching a critical magnetic field, it doesn't increase with further increase of magnetic field. NiMnCoIn alloys employ the Zeeman energy (the difference of saturation magnetization of transforming phases) as the main source for actuation. Zeeman energy is relatively orientation insensitive, providing the opportunity to employ NiMnCoIn polycrystals for actuator applications [14]. Additionally, Zeeman energy increases continuously with field so does the actuation stress [15]. However, the required magnetic field for phase transformation in NiMnCoIn alloys is very high for practical applications (> 4T) [14]. In this work, field-induced phase transformation in NiMnCoIn alloys will be investigated and possible ways to decrease the required magnetic field will be provided. Initially, shape memory

properties of NiMnCoIn single crystals are characterized since the critical magnetic field for phase transformation depends on transformation strain and critical stress for phase transformation, which are orientation dependent. Without proper understanding of SMA characteristics of NiMnCoIn it is not possible to fully understand the MSMA properties of this alloy.

A thermodynamical description will be introduced to understand magnetic energy contributions to trigger the phase transformation. Materials design and selection guidelines are proposed to search for new ferromagnetic materials that undergo thermoelastic martensitic phase transformation.

## 1.2 Active Materials

Active materials undergo a substantial change in one or more properties in response to a change in external conditions such as applied loads, altering temperature, electrical and magnetic fields. Piezoelectrics, magnetostrictives, shape memory alloys and recently discovered magnetic shape memory alloys are the main active materials groups that have been utilized for practical applications. These materials can transform one form of energy into another. In addition, they are capable of direct and inverse effects leading to applications as both actuators and sensors. An ideal active material would be the one that has high-frequency response, large strain and force outputs, high durability and low cost. Each active group stated above has advantages or disadvantages as compared to the others.

Piezoelectric materials are the most commonly used smart materials. They present two distinct characteristics; i) the “direct” piezoelectric effect occurs when a piezoelectric material subjected to a mechanical stress becomes electrically charged and ii) the “converse” piezoelectric effect occurs when the piezoelectric material becomes strained when placed in an electric field [16, 17]. Thus, these devices can be used to detect strain, movement, force, pressure, or vibration by developing appropriate electrical responses and the ability to induce strain can be used to generate a movement, force, pressure, or vibration by applying a suitable electric field. The most popular

commercial piezoelectric materials are lead zirconate titanate (PZT) and polyvinylidene fluoride (PVDF) [16]. Piezoelectric materials can produce strains of 0.18% (PZT) and 0.1% (PVDF) when exposed to an electric field in the frequency range of up to 100 kHz [16]. They have found numerous applications as both actuators and sensors e.g accelerometers, force transducers, ultrasonic motors, helicopter rotor blades[17]. Microscopically, in piezoelectric materials with the application of an electric field or stress, the off-center charged ion in a tetragonal unit cell moves from one axis to another [16, 18]. As the ion changes position it causes strain in the material. Poling is required in order to observe bulk strain in piezoelectrics [16].

Magnetostrictive materials can convert energy between the magnetic and elastic states. Due to the bidirectional nature of this energy exchange, magnetostrictive materials can be employed for both actuation and sensing. Alloys based on the transition metals, iron, nickel, and cobalt, in combination with certain rare-earth elements are currently employed in actuator and sensor systems in a broad range of industrial, biomedical, and defense applications e.g clamps, shakers, direct-drive motors, loudspeakers, helical line hydrophones [16, 17]. Because magnetostriction is an inherent property of ferromagnetic materials, it does not degrade over time as do some poled piezoelectric substances. Due to the required solenoid and related magnetic circuit components, magnetostrictive transducers are usually larger and bulkier than their piezoelectric or electrostrictive counterparts. Hence, they are employed primarily in applications that require high strains and forces but where weight is not an issue. One additional consideration is that the most technologically advanced magnetostrictive materials are costly to manufacture.

Terfenol-D is the most popular commercially available magnetostrictive material. The highest room temperature magnetostriction for Terfenol-D is 1,6 % at a moderate saturation field of 0.16 MA/m [16]. Terfenol-D is expensive to produce and is highly brittle [17, 18]. Recently discovered Galfenol system is more ductile and have higher strength than Terfonol-D but it can produce lower strains of about 0.03 % [19].

Moreover, its high permeability results in low cut-off frequencies due to eddy currents [19].

Microscopically, in magnetostrictive materials when a magnetic field is applied and an electron spin tries to align with it, the orbit of that electron also tends to be reoriented. But because the orbit is strongly coupled to the crystal lattice, the orbit resists the rotation of the spin axis. Thus, the energy required to rotate the spin system of a domain away from the preferred orientations is the energy required to overcome spin–orbit coupling. When magnetic field rotates the spins, the orbital moments rotate, and results in considerable distortion, and hence magnetostriction [16, 20]. The change in sample dimensions in the direction of applied field is called Joule magnetostriction. The Villari effect is the change in magnetization due to applied stress and is inverse of Joule magnetostriction. Magnetostrictives can be used as sensors and power harvesters due to the Villari effect [16].

Shape memory alloys (SMAs) are another class of smart materials that can produce very high recoverable strains (up to 20%) as a result of reversible martensitic phase transformation. Martensitic transformations (MTs) are first order, diffusionless, shear (displacive) solid state structural changes and can be triggered by temperature change, applied stress or magnetic field. The high temperature phase, austenite, transforms to low temperature and lower symmetry phase, martensite, and vice versa. The critical temperatures where the austenite transforms to martensite during cooling are named martensite start ($M_s$) and finish ($M_f$) temperatures where the temperature where martensite transforms to austenite during heating are called austenite start ($A_s$) and finish ($A_f$) temperatures.

MTs can be classified in two categories; thermoelastic and nonthermoelastic. For thermoelastic MTs; the transformation temperature hysteresis is small, the interface between parent and martensite is mobile and the transformation is crystallogrophically reversible [21]. For nonthermoelastic MTs, the transformation temperature hysteresis is large, the interface between the martensite and parent phase is immobile, and once the

martensite grows to some critical size, the reverse transformation takes place by renucleation of parent phase.

There are two deformation types in shape memory alloys which lead to high recoverable strains: variant reorientation (VR) of martensite and stress induced martensite. When shape memory alloys cooled down under zero stress, parent phase transforms to martensite and martensite variants form self-accommodating structures to minimize the macroscopic volume change. The applied stress biases the self accommodating structure and favors the growth of selected martensite variants among the others. When this biased structure is heated above $A_f$ temperature, it recovers back to its original shape which is called shape memory effect (SME). If self-accommodated structure is permanently biased (generally by forming dislocations and internal stresses), large macroscopic strain will be induced with forward and back transformations which is called two-way shape memory effect (TWSME) [22]. Figure 1.1 shows a schematic of SME and TWSME and pseudoelasticity (PE) in shape memory alloys.

It is well known that deformation of austenite in the range of $A_f$ to a certain temperature ($M_d$) results in stress induced martensitic transformation (SIM). Favored martensite variants form and during unloading, these martensite variants transform back to austenite since they are not chemically stable at that temperature. This deformation behavior is called pseudoelasticity or superelasticity. Pseudoelasticity is a more generic term than superelasticity. It encompasses also rubber like behavior which is observed in some SMAs when the bars in martensite phase are bent and aged to recover its original shape. Shortly, pseudoelasticity can be used for both martensite and austenite phases where superelasticity is used for parent phase only. As the temperature increases the stress needed for transformation also increases exceeding the stress for dislocation slip which deteriorates the pseudoelastic response. Deformations at temperatures higher than $M_d$ do not lead to stress induced transformation because dislocation slip is the only deformation mechanism.

Nitinol (Ni-Ti) is the most well known SMA which has been discovered by Buehler and his co-workers at the U.S Naval Ordinance Laboratory (NOL) in 1962 [23].

NiTi alloys can produce strains up to 8%, can be deformed easily and biocompatible [16, 17]. They have used in plenty of applications such as couplings, actuators, sensors, stents, guide wires, dampers etc. Cu-based shape memory alloys are also studied extensively since they are cheaper than NiTi. However, in these alloys aging might occur even at room temperature and it deteriorates the shape memory properties. Also their high elastic anisotropy restricts their usage in polycrystal forms [21].

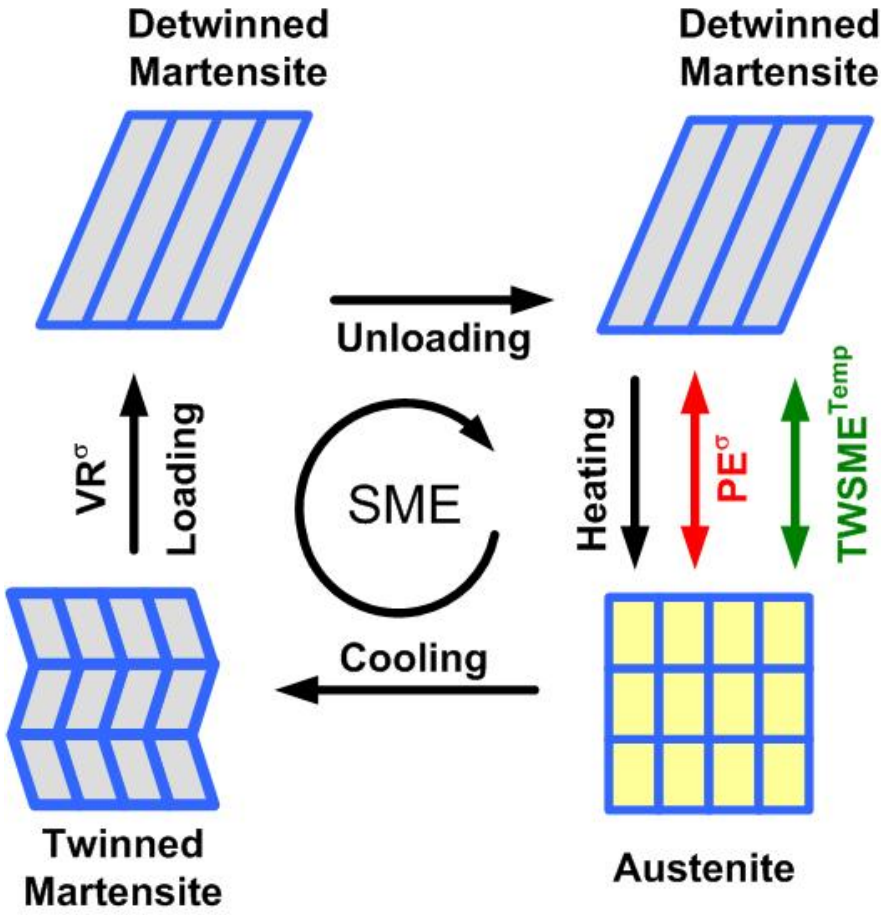


**Figure 1.1** Shape memory and two-way shape memory effect in shape memory alloys.

Table 1.1 shows the comparison of some active materials in terms of actuation strain, stress and frequency [24]. PZT is compact and light weight, operates over large

temperature range, function at high frequencies. It has excellent stability and fast response to applied voltage and no wear or tear on the element. However it is brittle, produces small strains compared to SMAs and magnetostrictives, cannot withstand high shear and tension, can become depolarized under high voltages or temperature [17, 24]. Terfenol-D, a magnetostrictive material, has fast response time (μsec), high Curie temperature, relatively high strain and force capabilities compared to piezoelectrics, no aging effects, can operate over large temperature range. However, it also has low tensile strengths, it is brittle and costly due to rare earth metals involved and in order to produce magnetic field intensive equipment is required [17, 24]. NiTi, a shape memory alloy, has good ductility, large stroke, force and work outputs but low operating frequency range [17, 21, 24].

**Table 1.1** Comparison of actuation strain, stress and operating frequencies of active materials [24]. PT: phase transformation.

| | | | Strain % | Stress MPa | Operating Frequency Hz |
|---|---|---|---|---|---|
| Heat | Shape-Memory Alloy (NiTi) | | 2-8 | 400 | 1 |
| Electric Field | Ferroelectric | | 0.1 | 3 | 100.000 |
| | Piezoelectric (PZT) | | 0.2 | 70 | 100.000 |
| Magnetic Field | Magnetostrictive (Terfenol-D) | | 0.2 | 80 | 10.000 |
| | MSMA ($Ni_2MnGa$) | VR | 5-10 | 5 | 1.000 |
| | | PT | 0.5-4 | 20-100 | |

## 1.3 Fundamental Magnetics Background

The macroscopic magnetic properties of materials are a result of magnetic moments associated with individual electrons. There are two sources of magnetic

moments: i) Electron's orbital motion around the nucleus: Being a moving charge, an electron may be considered to be a small current loop, generating a very small magnetic field, and having a magnetic moment along its axis of rotation, as schematically illustrated in Figure 1.2.a [25]. ii) Each electron may also be thought of as spinning around an axis: The other magnetic moment originates from this electron spin, which is directed along the spin axis as shown in Figure 1.2.b [25]. Spin magnetic moments may be only in an "up" direction or in an antiparallel "down" direction. Thus each electron in an atom may be thought of as being a small magnet having permanent orbital and spin magnetic moments.

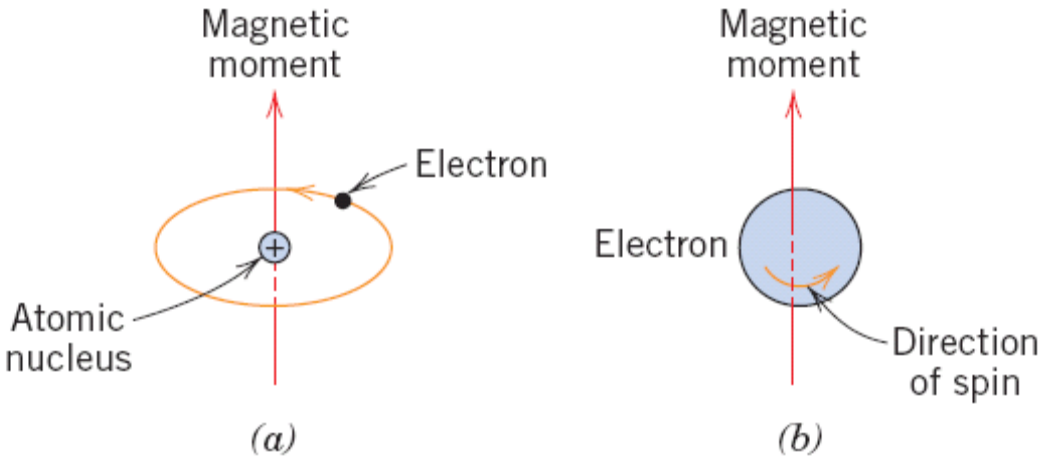


**Figure 1.2** Demonstration of the magnetic moment associated with (a) an orbiting electron and (b) a spinning electron [25].

The most fundamental magnetic moment is the Bohr magneton, $\mu_B$, which is 9.27 x $10^{-24}$ A.$m^2$ of magnitude [25]. For each electron in an atom, the spin magnetic moment is $\mp\mu_B$ (plus for spin up, minus for spin down). Furthermore, the orbital magnetic moment contribution is equal to $m_l.\mu_B$, $m_l$ is the magnetic quantum number of the electron [25].

The externally applied magnetic field, sometimes called the magnetic field strength, is designated by *H*. The magnetic induction, or magnetic flux density, denoted by *B*, represents the magnitude of the internal field strength within a substance that is subjected to an *H* field. Both *B* and *H* are field vectors, being characterized not only by magnitude, but also by direction in space. Another field quantity, *M*, called the magnetization of the solid, is defined by the expression [15];

$$B = \mu_0 H + \mu_0 M \qquad (1.1)$$

where $\mu_0$ is the permeability of a vacuum, a universal constant, which has a value of $4\pi \times 10^{-7}$ ($1.257 \times 10^{-6}$) H/m [25].

Diamagnetism is a very weak form of magnetism that is nonpermanent and persists only while an external field is being applied. It is induced by a change in the orbital motion of electrons due to an applied magnetic field. The magnitude of the induced magnetic moment is extremely small, and in a direction opposite to that of the applied field [25]. In paramagnetic materials there is only partial cancellation of the moments leaving the atom with a net moment [25]. In the absence of an external magnetic field, the orientations of these atomic magnetic moments are random, such that a piece of material possesses no net macroscopic magnetization. When a field is applied to a paramagnetic material, the atomic moments align themselves with the field to an extent determined by the magnitude of the field and the temperature. In ferromagnetic materials, an additional alignment of the moments due to quantum mechanical exchange forces occurs when the material is cooled below a critical temperature $T_c$, the Curie temperature [15, 25]. They possess a permanent magnetic moment in the absence of an external field, and manifest very large and permanent magnetizations [15].

Ferromagnetic materials are composed of small-volume regions, named as magnetic domains in which there is a mutual alignment in the same direction of all magnetic dipole moments and they magnetized to their saturation magnetization ($M^s$)[15]. Adjacent domains are separated by domain boundaries or walls, across which the direction of magnetization gradually changes. In an unmagnetized state, the total

magnetization of samples is zero due to formation of multiple magnetic domain formation where the magnetization vectors cancel each other.

### 1.4 Magnetocrystalline Anisotropy Energy

The magnetization vector in domains tends to point along the certain crystal orientation, called easy axis. The work required to rotate the magnetization from the easy axis along the applied magnetic field direction is called magnetocrystalline anisotropy energy [26]. Figure 1.3 shows the magnetization as a function of crystal orientation and applied magnetic field of iron and nickel [25]. At the initial stage total magnetization is zero and can be considered as multiple domains formed with their magnetization oriented along the easy axis e.g. [100] direction for iron. If the field is applied along the easy axis there will be only domain wall motion favoring the domains aligned along the applied field which generally requires low fields. If the field is applied in any other direction then in addition to domain wall motion, magnetization rotation will take place.

It is clear from the Figure 1.3 that magnetization depends on the crystallographic direction and applied field magnitude. The easy axes of iron and nickel are [100] and [111], respectively. The orientation where the MAE is largest called the hard axis and the hard axes of iron and nickel are [111] and [100], respectively. The magnetization response in any other orientation will be between these two extreme cases. The maximum MAE is shown by $K_u$ and it can be determined by calculating the area between the M-H curves of easy and hard axes.

Magnetic anisotropy energy for a uniaxial crystal is given by [15];

$$E_{anis} = K_{u0} + K_{u1}\sin^2\theta + K_{u2}\sin^4\theta \tag{1.2}$$

where $K_{ui}$ are the anisotropy constants and $\theta$ is the angle with respect to crystal axis. For cubic materials the expression for anisotropy energy can be written as [15];

$$E_{anis} = K_0 + K_1(\alpha_1^2\alpha_2^2 + \alpha_1^2\alpha_3^2 + \alpha_2^2\alpha_3^2) + K_2(\alpha_1^2\alpha_2^2\alpha_3^2) \tag{1.3}$$

where $\alpha_i$ 's are the direction cosines of the magnetization along the cubic axes and $K_i$'s are the anisotropy constants. $K_1$ and $K_2$ can be used to characterize the magnetic properties of the material. For example, $K_1$ is positive for iron and negative for nickel so

easy axes are [100] and [111], orientations respectively. For tetragonal symmetry MAE can be expressed as [27];

$$E_{anis} = K_{u1}\sin^2\theta + K_{u2}\sin^4\theta + K_{u2}\sin^4\theta\cos^4 4\varphi \qquad (1.4)$$

where $\theta$ and $\varphi$ are polar coordinates. If $K_{u1}$ is positive the crystal has an easy axis along the c-axis which is the case for 10M martensite of NiMnGa alloys. If $K_{u1}$ is negative and $K_{u1}<-2K_{u2}$, the crystal has an easy plane of magnetization, in which the ab-plane is the easy plane and the c axis is the hard magnetization direction as in the case of nonmodulated martensite of NiMNGa alloys [28, 29]. For an orthorhombic crystal, the magnetic anisotropy energy is expressed using directional cosines $\alpha_i$ as [30];

$$E_{anis} = K_1\alpha_1^2 + K_2\alpha_2^2 + K_3\alpha_3^2 + K_4(\alpha_1^2\alpha_2^2) + K_5\alpha_2^4 \qquad (1.5)$$

Straka *et al.* [30] reported that for 14 M martensite of NiMnGa alloy the *c*-axis ([0 0 1] direction) is easy axis of magnetization, i.e. $K_3\approx 0$, *b*-axis is mid-hard axis ($K_2=0.9\times10^5$ Jm$^{-3}$), and long *a*-axis is hard axis ($K_1=1.7\times10^5$ Jm$^{-3}$) of magnetization.

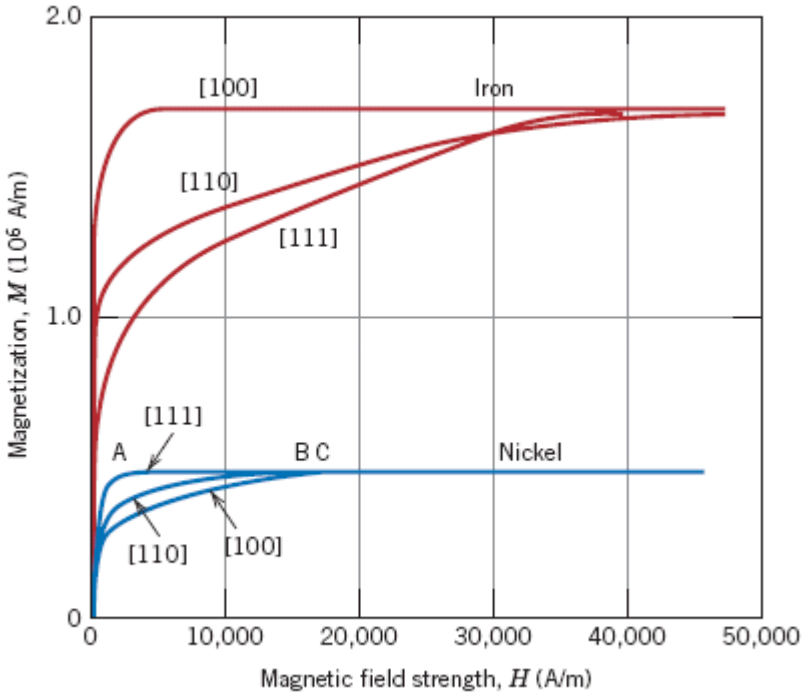


**Figure 1.3** The magnetization versus applied magnetic field response along the [100], [110] and [111] orientations of iron (bcc) and nickel [25].

It is important to note that saturation magnetization is temperature dependent and decreases with increasing temperature so does the anisotropy constants [28, 30]. Sozinov *et al.* [28] reported the room temperature anisotropy constants, lattice parameters, theoretical detwinning strain ($\varepsilon_o$), detwinning stresses and observed MFIS values of three martensite types of NiMnGa alloys as shown in Table 1.2 and the magnetization vs. applied field responses are shown in Figure 1.4

**Table 1.2** Summary of lattice parameters, cell volume, transformation strain, detwinning stress, MAE and MFIS of three types of martensite structures [28]. In the table, 5M, T and 7M stand for 10M, non-modulated, and 14M martensitic structures.

| Martensite type | 5M ($c/a<1$) | T ($c/a>1$) | 7M ($a>b>c$) |
|---|---|---|---|
| Composition, at. % (±0.5%) | $Ni_{49.2}$ $Mn_{29.6}$ $Ga_{21.2}$ | $Ni_{52.1}$ $Mn_{27.3}$ $Ga_{20.6}$ | $Ni_{48.8}$ $Mn_{29.7}$ $Ga_{21.5}$ |
| Lattice parameters, nm | $a$=0.594 $b$=0.594 $c$=0.559 | $a$=0.546 $b$=0.546 $c$=0.658 | $a$=0.619 $b$=0.580 $c$=0.553 |
| Cell volume, $nm^3$ | 0.197 | 0.196 | 0.199 |
| $\varepsilon_0 = (1 - c/a)$ % | 5.89 | 20.5 | 10.66 |
| $\sigma^s$, MPa | 1 | 12-20 | 1.1 |
| $\sigma^f$, MPa | 2.1 | 12-20 | 1.9 |
| $(\mu_0 M_s)$, T | 0.6±0.05 | 0.6±0.05 | 0.6±0.05 |
| Magnetic anisotropy, $10^5$ J/$m^3$ | 1.45 ($K_u$) | -2.03 ($K_u$) | 1.6 ($K_a$) 0.7 ($K_b$) |
| MSM strain, % | 5.8 | Less than 0.02 | 9.4 |

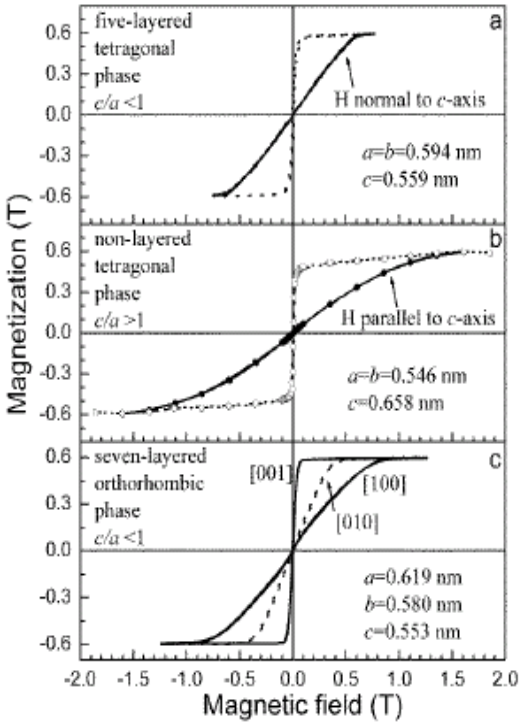


**Figure 1.4** Magnetization versus applied field responses of three martensite structures of NiMnGa alloys along the a, b and c axes [28].

### 1.5 Magnetic Domains

As stated earlier under no magnetic field the total magnetization of a ferromagnetic material is zero due to formation of magnetic domains. Magnetic domains form to reduce the magnetization of the material by reducing the magnetostatic energy [15]. However the formation of magnetic domain results in an increase in domain wall length which costs energy. The thickness of domains walls are determined by the exchange and anisotropy energy and can range from 10nm to several μm [15].

Magnetic domain structure of NiMnGa is reported by James *et al.* [31] observation is using a magnetic force microscopy. They revealed a hierarchical domain structure with a herring-bone pattern, i.e. the 180˚ domains formed in each martensite variant. Figure 1.5 shows the similar structures observed by several researchers using various techniques [32, 33]. Pan *et al.* [34] studied the evolution of a hierarchical domain

structure with a herring-bone pattern under an applied field. The application of a small field (1-2 kOe) results in formation of a firtree pattern meeting at the twin boundaries. The application of an intermediate field (4-5 kOe) in the easy direction of one twin variant caused the magnetization vector of the neighboring twin variants to rotate a little and the firtree pattern to localise at the twin boundaries. With larger fields (8-9 kOe), the magnetization vector that was previously orthogonal to the field will rotate in the field direction and eliminate domain structure within a variant, so each twin band coincides with one magnetic domain.

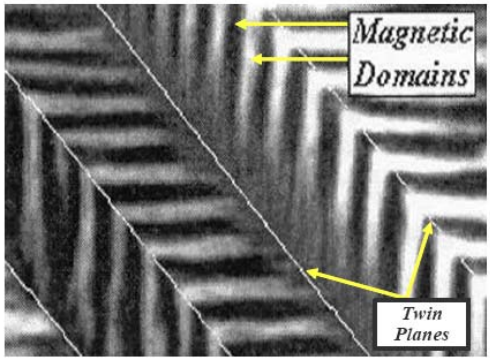


(a)

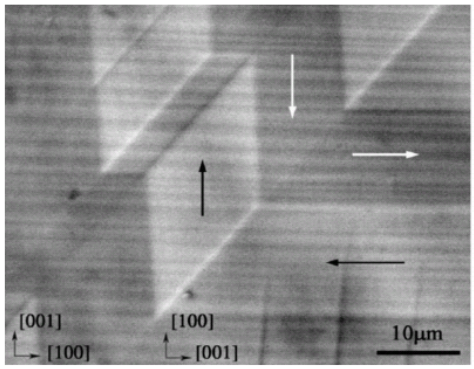


(b)

**Figure 1.5** Domain structures of NiMnGa alloys determined using a) the magnetic garnet film technique [35] and b) scanning electron microscopy images [33].

## 1.6 Magnetic Shape Memory Alloys

### 1.6.1 Magnetic Field-Induced Variant Reorientation

The most commonly observed magnetic field induced strain is based on the rearrangement of martensite variants by detwinning [5-8]. NiMnGa alloys are the most widely explored MSMAs [4, 7] among others such as FePt [36] , FePd [5, 37], CoNiAl [38-40], CoNiGa [41], CoNi [42], NiFeGa [43, 44], NiFeGaCo [45] due to their low stress requirements for detwinning and high magnetocrystalline anisotropy energy.

When there is no external magnetic field, magnetic domains have a tendency to orient along the easy axis of magnetization. If a magnetic field is applied along a direction other than the easy axis, the magnetization direction of the domains will rotate from their easy axis towards the applied field direction. The energy required for the magnetization rotation from the easy axis to the applied field direction is given by the magnetocrystalline anisotropy energy.

If the MAE is higher than the energy needed for detwinning, variant reorientation can occur. The variant with the easy axis of magnetization along the applied field direction can grow in the expense of others resulting in a net MFIS [8]. Figure 1.6 shows a schematic for field induced variant reorientation mechanisms of MSMAs. Initially the total magnetization of the sample is zero. Each twin has internal 180˚ magnetic domains where their magnetization directions are in opposite directions. As the strength of applied magnetic field increases, instead of rotation of magnetization along the applied field twin motion occurs to align and some external strain can be detected. If MAE is large and the stress needed for twin motion is low enough it is possible to obtain single variant of martensite with applied magnetic field. In order to maximize the MFIS in NiMnGa single crystal, a single variant with c-axis along the compression direction reorients to another single variant with c-axis along the applied field perpendicular to compressive axis.

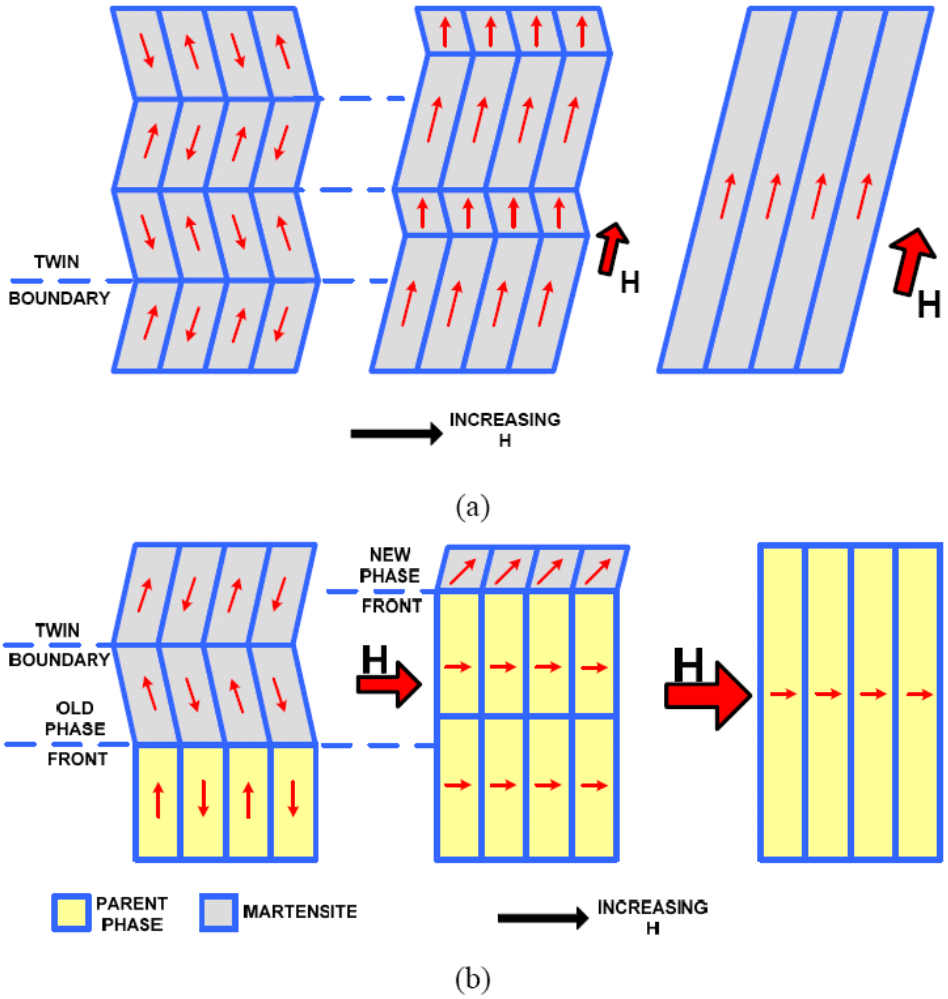


**Figure 1.6** Effect of applied magnetic field, H, a) on the reorientation of the martensite twin variants and b) on phase transformation in MSMAs.

There are two main parameters other than the MFIS level that are used to quantify the performance of MSMAs. The first one is the blocking stress or maximum actuation stress, i.e. the external stress level above which magnetic field induced reorientation is not possible. Magnetostress, the second parameter, is defined as the increase in stress required for detwinning under a constant magnetic field. One of the main issues in development of MSMAs is low blocking and magnetostress levels (<2 MPa) observed [13, 46], which impedes the utilization of these alloys in practical applications where high actuation forces are required. The maximum MFIS of NiMnGa

alloys reported to date is approximately 6% in 10M martensite [13, 46] and 10% in 14M martensite [47].

MFIS by variant reorientation in NiMnGa alloys can be easily reversible after the removal of magnetic field, if the stress and field are applied perpendicular to each other or the field is applied along two perpendicular axes. In literature, there are only few systematic investigations on the reversible magnetic field induced strain response of NiMnGa alloys under different applied stress levels [26, 46, 48]. Tickle [26] reported 2% MFIS with a blocking stress of 4-6 MPa at -18 ˚C, where Murray *et al*. [46] and Heczko *et al*. [48] reported 6% MFIS with a blocking stress of 2 MPa at 25 ˚C.

### 1.6.2 Magnetic Field-Induced Phase Transformation

The second possible mechanism to induce large MFIS is the magnetic field-induced phase transformation. Figure 1.6.b shows a schematic for field induced phase transformation. As magnetic field applied or removed phase front between martensite and austenite phases can move and one phase can transform to another one. The necessary conditions for field induced phase transformations and whether austenite transforms to martensite or vise versa with applied field will be discussed in details later.

The main requirement for the field-induced phase transformation is that the magnetic driving energy must be sufficient to move the phase front. The irreversible field-induced martensitic phase transformation has been detected in several ferromagnetic materials, especially in iron based alloys such as Fe-C and Fe-Ni [36, 49-51], under very high field magnitudes (>15 Tesla) without any report of observed MFIS levels. It was shown that applied magnetic field changes the transformation temperatures, transformation behavior and transformed structures [51]. Certain Fe-Ni-Co-Ti alloys demonstrated reversible field-induced martensitic transformation but only under the application of a high pulsed magnetic field (~30 Tesla) [36]. Obviously, the need for giant magnetic fields severely limits the use in actual applications.

Similar to the iron based alloys, applied magnetic field increases the transformation temperatures of NiMnGa alloys when austenite is paramagnetic and

martensite is ferromagnetic [52]. Cherechukin *et al.* [52] used this fact to indirectly obtain MFIS by phase transformation. They heated the specimen up to a temperature between the austenite finish temperatures with $A_f^H$ and without magnetic field $A_f$ while the field was applied in martensite. When the field was removed at this temperature phase transformation from martensite to austenite occurred since martensite was no longer stable at that temperature. MFIS induced by this method was also irreversible upon the reapplication of the field.

Recently, field-induced reversible phase transformation in NiMn(In,Sn) based alloys by using the fact that applied magnetic field suppresses the transformation temperatures in the amount more than thermal hysteresis under zero field [14, 53, 54]. In other words, $A_f^H$ is lower than martensite start temperature under zero field, $M_s$. Applying magnetic field at a temperature between $A_f^H$ and $M_s$ results in reversible MFIS. In this mechanism, the required magnetic field for phase transformation was more than 4 Tesla which is still quite high for practical applications.

### 1.6.3 Stress-Assisted Magnetic Field-Induced Phase Transformation in MSMAs

NiMnGa alloys are unique in the sense that they demonstrate composition, orientation and stress state dependent multi-stage martensitic transformations [55, 56]. Depending on the composition, single crystal orientation, and temperature, they can experience the complete or part of the following four stage transformation sequence, i.e. $L2_1$ parent to intermediate to 10M tetragonal to 14M orthorhombic (or monoclinic) to nonmodulated (2M) tetragonal martensitic transformations [55, 56]. Even though the field-induced microstructural changes in each martensitic phase were studied relatively in detail, there are only a few reports on the field-induced intermartensitic phase transformations.

Available magnetic energy for triggering phase front motion in MSMAs are usually small. The stress levels that stem from the available magnetic energy in MSMAs are only a few MPas [26, 46]. On the other hand, the critical stresses required for stress–

induced phase transformation are at least on the order of tens of MPas. Figure 1.7 shows stress versus strain response of stress induced variant reorientation and phase transformation in NiMnGa single crystal at -90 and -40 ˚C, respectively. Therefore, the possibility of inducing phase transformation using magnetic field has usually been neglected in MSMAs due to the large difference between these two stress levels. Only in a few recent studies, mechanical stress and magnetic field were applied simultaneously to induce phase transformation [57, 58]. In these studies, the specimens, initially in austenitic phase, were mechanically loaded until partial stress induced martensitic transformation has occurred, then magnetic field was applied and MFIS was recorded. Murray *et al.* [57] reported 0.2% strain by martensite to austenite phase transformation under 108 MPa while Jeong *et al.* [58] reported 0.82% strain by austenite to martensite phase transformation under 126 MPa compressive stress both in polycrystalline NiMnGa alloys. The MFIS reported by Jeong *et al.* [58] was not recovered upon the removal of the field while it is not clear whether the one reported by Murray *et al.* [57] was recovered. It is important to note that in the aforementioned studies, austenite was ferromagnetic in the former case while it was paramagnetic in the latter one. In this study, it will be shown that the applied field can result in austenite to martensite phase transformation or vice versa, depending on the saturation magnetization, MAE and directions of applied magnetic field and stress state (tension or compression).

### 1.7 Brief History and Crystal Structures of NiMnGa

Webster and his colleagues were the first to report the phase transformation and magnetic properties of NiMnGa in 1984 [59]. This work is followed by the works of Kokorin and Chernenko and they focused on thermally and stress induced martensitic transformation and characterization of premartensitic phase in collaboration with researchers from Spain.

In 1996, Ullakko *et al*.[6] showed 0.2% MFIS under 0.6 T at 265 K based on the variant reorientation for the fist time in NiMnGa alloys. James and Wuttig [5] reported necessary conditions for observing MFIS by variant reorientation mechanism and

reported 0.5% strain in FePd alloy. O'Handley [8] introduced his modeling approach in 1998 for twin boundary and phase boundary motions. Tickle and James [60] focused on maximizing the MFIS via biasing the initial martensite structure with stress and reorienting single martensite variant to another one and reported 4% strain in NiMnGa. Murray *et al.* [46] increased the MFIS to 6% and approached the theoretical c/a limit for 10M martensite structure they have investigated. Later, Hezcko [48] and many other groups have also observed strains close to theoretical limit. In 2002, Sozinov *et al.* [47] reported 9.5% MFIS in the 14M martensite of NiMnGa alloys. Later Mullner *et al.* [61] reported cyclic 9.7% MFIS in the14M martensite by rotating the magnetic field around the sample. The theoretical strain for non modulated tetragonal martensite structure is 20% but only very small MFIS is observed in this structure due to high detwinning stress [62, 63].

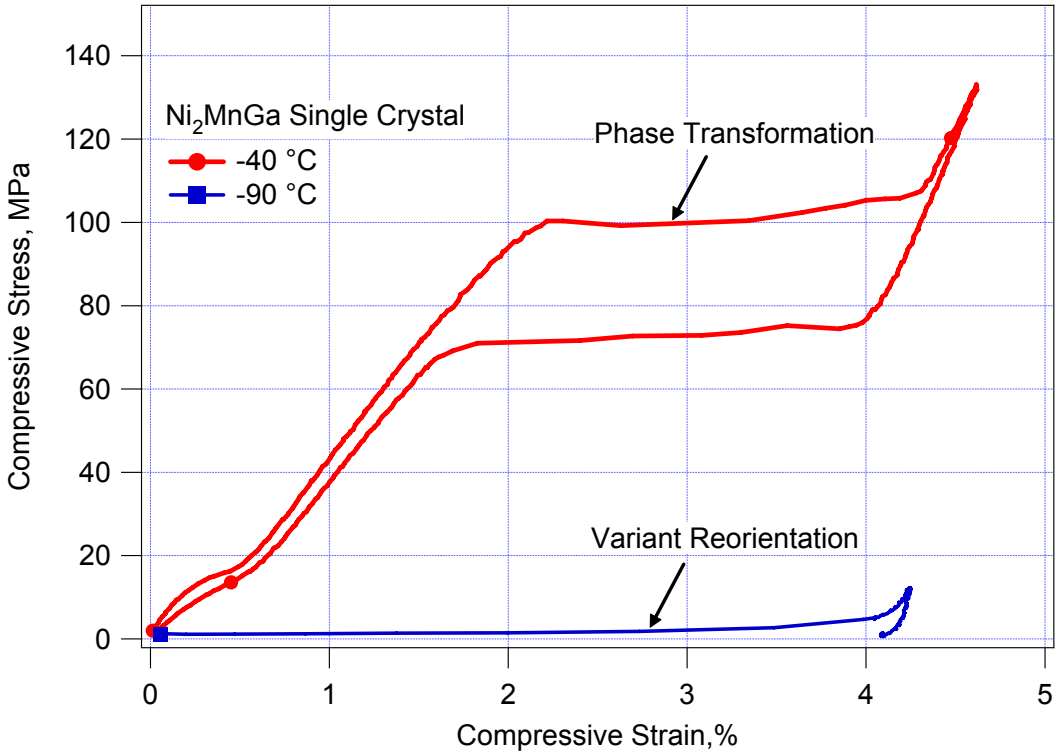


**Figure 1.7** Stress-induced phase transformation and variant reorientation response of $Ni_2MnGa$ single crystal of the present work at -40 and -90 ˚C, respectively.

The high temperature phase of NiMnGa has a cubic structure of B2 ($Pm\bar{3}m$) for temperatures higher than 1073K [64]. This crystal structure transforms to $L2_1$ Heusler type structure ($Fm\bar{3}m$) by a second-order phase transformation at a composition dependent temperature (~1073K) [65, 66]. The lattice parameter of $L2_1$ structure is around 0.582 nm and it is composition and temperature dependent [67]. Figure 1.8 shows the $L2_1$ structure of $Ni_2MnGa$ where Mn atoms occupy the 4a position, Ni the 4c position and Ga the 4b position in the stoichiometric composition.

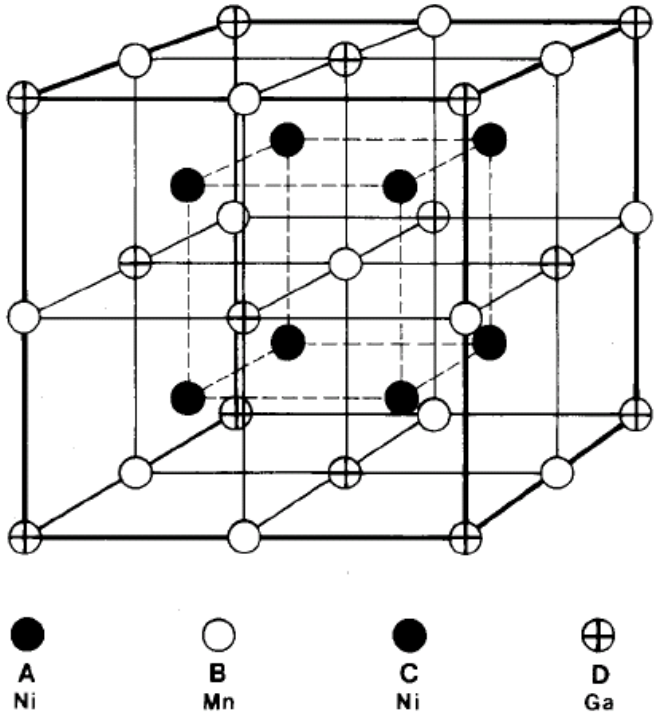


**Figure 1.8** $L2_1$ structure of NiMnGa alloy [59].

The crystal structure of the martensite phase in NiMnGa alloys depends on the composition and temperature [68, 69]. Martensitic structure type, transformation and

Curie temperatures are determined to be functions of electron to atom ratio (e/a) of the alloy and can be determined by multiplying the number of valence electrons with atomic percentage of each element. The valence electron numbers are 10, 7 and 3 for Ni, Mn and Ga, respectively. Depending on the composition, $L2_1$ structure transforms to 10M, 14M or 2M structure. There seems to be an order for the intermartensitic transformations and if the transformation temperature from parent phase (P) to martensite is low (<250 K) a premartensitic phase (I) might be observed. The sequence of transformations can be summarized as $P \rightarrow I \rightarrow 10M \rightarrow 14M \rightarrow 2M$ . A more detailed review on the effect of composition and premartensitic phases can be found in refs [29, 70].

During martensitic transformation in NiMnGa alloys, the (110) plane undergoes a periodic shuffling in the $[1\bar{1}0]$ direction. If the crystal structure is 10M or 14M than every 5$^{th}$ or 7$^{th}$ (110) plane remains in its original position. The average lattices of 10M and 14M structures are approximately tetragonal (c/a<1) and orthorhombic (c/a<1). The crystal structure of non-modulated T is tetragonal with c/a>1.

Premartensitic phase which is also known as precursor pheonema is observed on shape memory alloys at temperatures close to phase transformation and originates from electron-phonon coupling [29]. It has been shown that premartensitic phase transition for NiMnGa alloy is composition dependent, a first-order transition originated by the magnetoelastic coupling between the magnetization and the $TA_2$ phonon [71-73]. Zhao [29] classified the NiMnGa alloys in three regions whether tweed-like and premartensitic phenomena occurs prior to transformation or not. If e/a ratio is less than 7.6 and $M_s$ is lower than room temperature, both premartensitic and tweed phases can be observed. HRTEM and TEM images proved the existence of tweed structure and premartensitic phase with the extra spots observed in the electron diffraction patterns [74, 75]. Brown *et al.* [56] investigated the phase transformation of $Ni_2MnGa$ with high resolution neutron powder diffraction and single crystal measurements and revealed that before phase transformation from austenite to martensite, premartensitic phase with orthorhombic unit cell occurs. Gonzalez-Comas *et al.* [71] reported that elastic constants show significant softening at the intermediate phase transition and magnetic field and applied stress result

in an increase of all the elastic constants. They also revealed that premartensitic transition under stress occurs with thermal hysteresis.

### 1.8 Brief History and Crystal Structures of NiMnCoIn

In recent years a new FSMAs, called as meta-magnetic shape memory alloys, are emerged by substituting Ga with In, Sn or Sb and sometimes with the addition of Co [14, 53, 54, 76, 77]. Heusler type $Ni_2MnX$ alloys have been investigated for their magnetic properties [78]. In 2004, Sutou *et al.* [77] investigated these alloys for their potential to demonstrate MFIS. In 2006, Kainuma *et al.* [14] reported that in a NiMnCoIn alloy, ferromagnetic parent phase transforms to paramagnetic martensite phase and with increased applied magnetic field magnitude transformation temperatures decrease. They have been able to show reversible phase transformation under the magnetic fields larger than 4 Tesla where martensite transformed to austenite and the critical magnetic field for phase transformation shown to be depend on temperature. They have also reported one-way 3% MFIS in a predeformed single crystal sample with the applied field of 4T. They reported that the parent and martensite phases have the $L2_1$ Heusler-type ordered structure where $a$ = 0.5978 nm and the 14M modulated structure where $a$ = 0.4349 nm, $b$ = 0.2811 nm, $c$ = 2.9892 nm and $\beta$= 93.24°, respectively [14]. Later, they have also observed the same behavior in NiCoMnSn polycrystalline alloy and reported about 1% one-way and 0.3% reversible MFIS [53]. Wang *et al.* [79] observed reversible MFIS in a NiMnCoIn alloy under 50 MPa which is one orders of magnitude higher than the actuation stress in NiMnGa alloys and they determined the martensite to be 14M. Recently Kerenke *et al.* [80] reported 0.12 % reversible MFIS in NiMnIn alloys with the required applied magnetic field of 4T . They have also reported the crystal structure is similar to NiMnGa where the parent phase has $L2_1$ structure with $a$=0.6011 nm and martensite has 10 M modulated martensite structure having a monoclinic unit cell with $\gamma$=86.97° and lattice constants $a$=0.4398 nm, $b$=0.5635 nm, and $c$=2.1720 nm [80].

There have been only a few experiments conducted on NiMnCoIn alloy system although they have a very promising potential to be used as MSMA with high actuation output. There has not been a systematic study on shape memory properties of parent phase, effect of magnetic and heat treatments on phase transformations.

# CHAPTER II
# EXPERIMENTAL PROCEDURES

Ingots of NiMnGa and NiMnCoIn with nominal compositions of 50Ni-25Mn-25Ga and 45Ni-36.5Mn-5Co-13.5In (in at. %) were prepared using vacuum induction melting. Bridgman technique was employed to grow single crystals in a He atmosphere. The composition of the single crystals was determined to be $Ni_{51.1}Mn_{24.0}Ga_{24.9}$ using inductively coupled plasma-atomic emission spectrometry (ICP-AES) and $Ni_{45.7}Mn_{35.6}Co_{4.8}In_{13.8}$ by using wavelength-dispersive spectroscopy (WDS) method. The difference between the nominal and actual compositions is probably due to the Mn evaporation during single crystal growth [77]. The single crystal samples were cut into rectangular prisms with dimensions of 4 mm x 4 mm x 8 mm using electro-discharge machining to assure that both magnetic field and stress can be applied along known crystallographic directions. The face normals of the samples were along [100], [011], and $[01\bar{1}]$ directions in the austenite phase ($L2_1$ ordered structure). Unless it is specified otherwise, compressive stress was applied along the [100] orientation, while the field was applied along the [011] direction. The $Ni_{51.1}Mn_{24.0}Ga_{24.9}$ single crystals have a 10M tetragonal structure in martensite as evidenced by the strain levels achieved upon martensite reorientation. Prior to testing all NiMnCoIn samples were heat treated at 900˚ C for 24 hours and quenched in water.

The optical images of NiMnCoIn samples are taken after they were mechanically polished and, then etched in 75ml HCl, 75ml ethanol, 15g $CuSO_4$ and 10ml distilled water solution. Compositional analysis of the precipitates and the matrix of tha NiMnCoIn alloy was carried out on a four spectrometer Cameca SX50 electron microprobe at an accelerating voltage of 15 KV and a beam current of 10 nA. All quantitative work employed the WDS method.

A Quantum Design Superconducting Quantum Interference Device (SQUID) magnetometer, model MPMS-XL, was used to measure the magnetization of the crystals

as a function of temperature under different constant applied magnetic fields, and magnetization as a function of applied magnetic field at different temperatures.

The in situ high-magnetic field Synchrotron-based high-energy (115 keV) x-ray diffraction experiments were conducted at the 11-ID-C beamline at the Advanced Photon Source, Argonne National Laboratory using a superconducting magnet (7 T Oxford Instrument) installed on the beamline with a temperature range of 320–4 K. The diffraction spots were recorded using a two-dimensional (2D) image plate detector (Mar345). The magnetic field was applied parallel to the incident x-ray beam.

A custom-designed magneto-thermo-mechanical setup was used to characterize the samples' response. A schematic and a picture of the MTM setup are shown in Figures 2.1 and 2.2, respectively. This experimental setup consists of four main subsystems: a servo-hydraulic load frame, custom-built compression grips, custom-built thermal control system, and an electromagnet. An MTS 810 Material Testing System, is capable of applying 250 kN of force is used as the main frame. Force is measured using a variaty of different load cells depending upon the type of experiment to increase the accuracy. The load cells were a 500 lbf. Interface model 1010ACK-500-B and 2500 lbf. Interface model 1010ACK-2.5K-B. Custom-built nonmagnetic Cu-Be grips with alumina inserts at the tips or Ti6Al-4V grips and inserts are designed and attached to the MTS system. A nonmagnetic capacitive displacement probe, Capacitec model HCP-75-21943, with a linear range of 0-1.25 mm was attached to the inserts to measure the change in length between the end points of the specimen. Strain is calculated by dividing the change in length to the initial length of the sample. A Lake Shore Model EM4-CS, electro-magnet was attached to the test frame to generate uniform magnetic fields up to 1.6 kG in a 2.5cm x 2.5cm x 2.5 cm volume with a controllable magnetic field generation rate. Magnetic field measurements were performed by a Lake Shore model 450 gaussmeter equipped with a Lake Shore high sensitivity cryogenic transverse Hall probe. Resolution of the probe was ±0.0001 kG within ±30 kG range. It was positioned away from the specimen lying perpendicular to the magnetic field lines in between the pole pieces of the electromagnet.

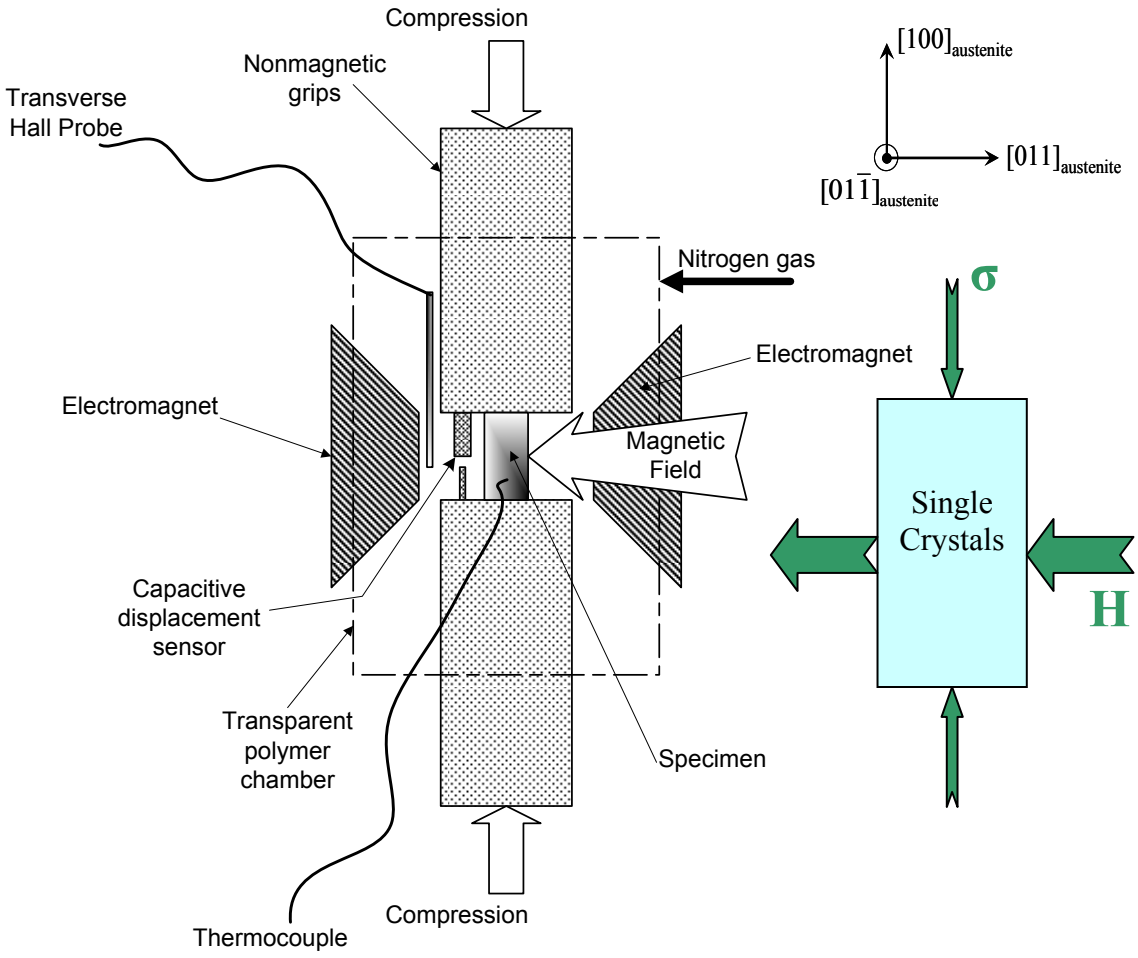


**Figure 2.1** Schematic of the magneto-thermo-mechanical setup with an electromagnet and a capacitive displacement sensor used in this study.

An Omega CN8200 series temperature controller was used to ensure stable cooling rates with T type nonmagnetic thermocouples attached to both the specimen and nonmagnetic grips. A Jefferson brand cryogenic grade ON/OFF solenoid valve commanded by the temperature controller was used to control the flow of nitrogen gas into the polymer (lexan) box surrounding the specimen or channeled through a pair of Cu coil windings press-fit to both the upper and lower grips. The heating is done either by simply letting the system heat up to room temperature by convection or using a pair

of heaters (Watlow, STB2C2AA-4). The heaters where the resistive elements are mica encapsulated and an austenitic stainless steel clamps the whole assembly are securely fastened around the Cu coil windings on both the upper and lower grips. The temperature could be controlled from 250˚ C down to -110 ˚C using this setup.

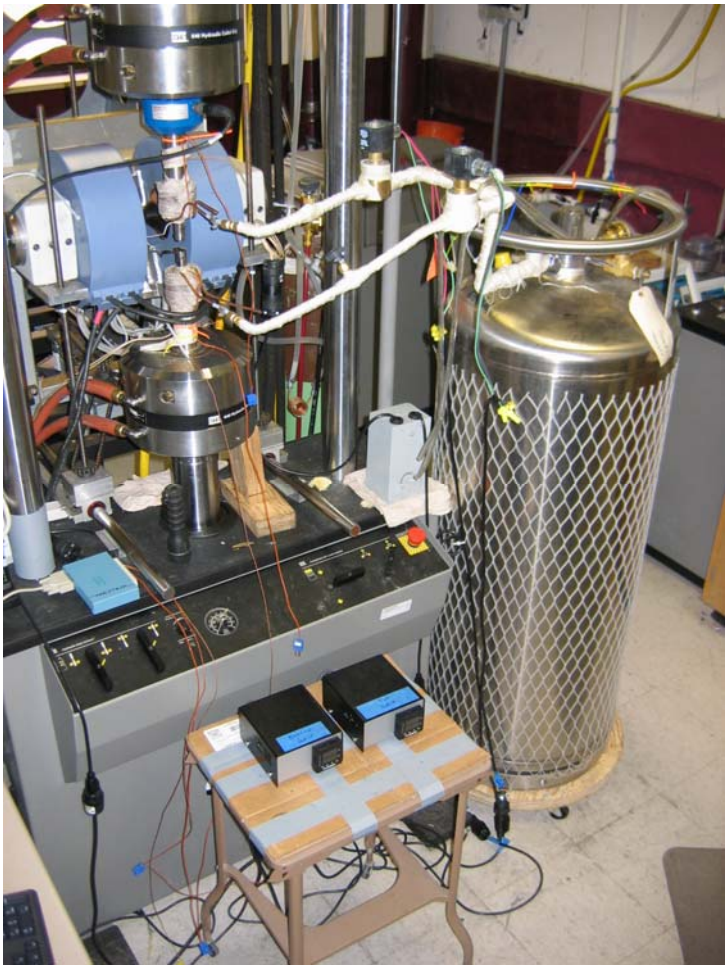

**Figure 2.2** A picture of magneto-thermo-mechanical experimental test setup.

Figure 2.3 shows a representative set of data obtained during a typical MTM experiment using this setup. The stress is applied and kept constant, temperature is kept constant, magnetic field is ramped and strain response is measured. The steup makes it possible to control three of the four variables (stress, strain, magnetic field and

temperature) and their rates simultaneously and allow monitoring the response from the last one. A test matrix is constructed for the possible experiments that can be conducted using the MTM setup as a function of test temperature, the state of the aforementioned four parameters, and in some cases, their rates, as shown in Table 2.1. The table also includes the effects or properties that each experiment targets to determine. Additionally, orientation dependence, cyclic response and effects of training can also be added as additional parameters to the table. In the present study most of these possible experiments are conducted and corresponding properties are revealed as listed in the table.

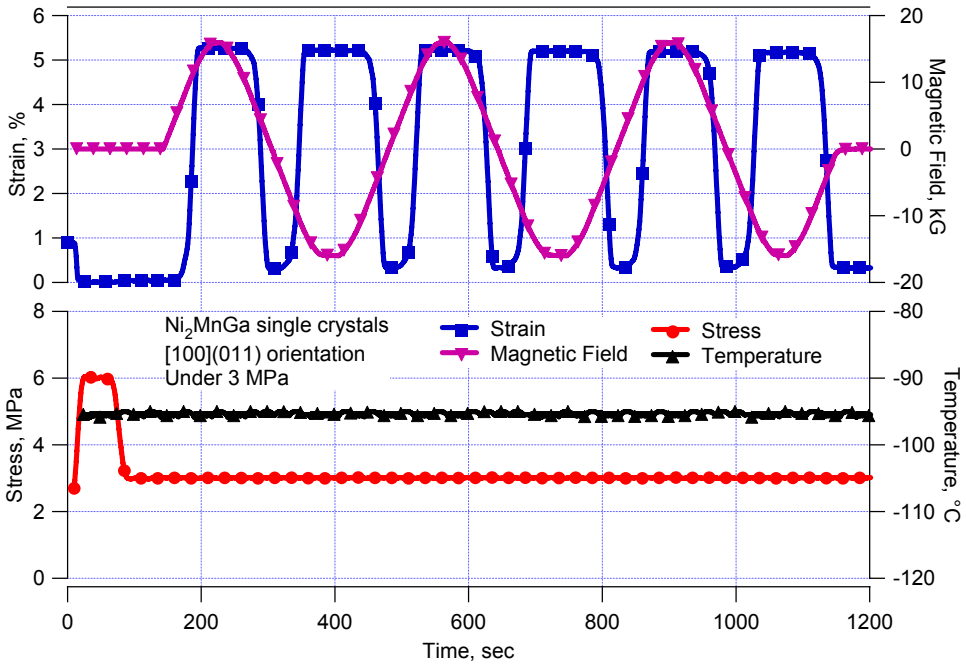


**Figure 2.3.** A plot of the representative data obtained during the magneto-thermo-mechanical experiments. The stress is applied and kept constant, temperature is kept constant, magnetic field is ramped and the strain response is measured.

**Table 2.1** Text matrix showing the possible experiments that could be performed using the magneto-thermo-mechanical setup shown in Figure 2.2 and their targeted outputs. MFI: magnetic field induced, MFIPT: magnetic field induced phase transformation.

| Temp | σ | H | ε | T | done | Target Output |
|---|---|---|---|---|---|---|
| $<M_f$ or $<A_s$ | Fixed | Variable | Measured | Fixed | Y | Butterfly curves |
| $<M_f$ or $<A_s$ | Variable | Fixed | Measured | Fixed | Y | Magneto-superelastic curve |
| $<M_f$ or $<A_s$ | Fixed | Variable f(Ṙ) | Measured | Fixed | Y | Magnetic Field Rate Effect |
| $<M_f$ or $<A_s$ | Measured | Variable | Fixed | Fixed | N | MFI Stress |
| $>A_f$ | Fixed | Variable | Measured | Fixed | Y | MFI phase transformation |
| $>A_f$ | Variable | Fixed | Measured | Fixed | Y | Effect of H on PE Curves |
| $>A_f$ | Measured | Variable | Fixed | Fixed | N | MFI Stress |
| | Fixed | Fixed | Measured | Variable | N | Magnetic Field-T and Stress-T Phase Diagrams |
| $>A_f$ | Variable | Fixed | Incremental | Fixed | N | Effect of Strain on Hysteresis |
| $M_s<T<A_f$ | Variable | Fixed | Measured | Fixed | Y | MFIPT VR |

# CHAPTER III
# MAGNETIC FIELD-INDUCED MARTENSITE REORIENTATION IN $Ni_2MnGa$ ALLOYS

## 3.1 Magnetization Results

Figure 3.1 shows the magnetization of $Ni_{51.1}Mn_{24.0}Ga_{24.9}$ as a function of temperature under a low applied magnetic field of 200 Gauss (G) determined in the SQUID. 200 G is low enough that it will not change the transformation temperatures. As temperature decreases, austenite transforms to martensite confirmed by a decrease in magnetization due to higher MAE of martensite than austenite. When heated, martensite transforms back to austenite as its evident from the increase in magnetization. This transformation occurs in a hysteretic manner which is a characteristic behavior of shape memory alloys. Magnetization response is differentiated with respect to temperature and the resulting curve is also shown in the figure. This curve is similar to the differential scanning calorimetry response of a conventional shape memory alloy which is widely used to determine the transformation temperatures. The dM/dT curve illustrates two separate phase transformations. The high temperature, very shallow peak with no thermal hysteresis represents the transformation from the parent phase to the I-phase, premartensitic phase, which occurs before phase transformation in some SMAs, as discussed in the introduction section. The low temperature, sharper peaks represent the phase transformation from the I-phase to 10M martensite or vice versa. The transformation temperatures for the I-phase to 10M were found using this curve to be -60, -100, -92 and -47 °C for $M_s$, $M_f$, $A_s$ and $A_f$ temperatures, respectively.

Figure 3.2.a exhibits the magnetization of the $Ni_{51.1}Mn_{24.0}Ga_{24.9}$ single crystals as a function of temperature under constant field magnitudes demonstrating the effect of magnetic field on the phase transformation temperatures. The measurements were conduted by cycling the temperature between -120 °C and 20 °C. Under 200 G, transformation starts at -60 °C and finishes at -100 °C. When the magnetic field is increased to 10 kG transformation starts at at -58 °C and finishes at -88 °C. The drop in

magnetization during the forward phase transformation (transformation upon cooling) under low magnetic field magnitudes stems from the higher magnetic anisotropy of martensite [81]. When the field is increased to 10 kG, there is still a magnetization hysteresis loop between forward and backward phase transformations, however, this time magnetization increases during the forward transformation. This increase possibly stems from the higher saturation magnetization of martensite than that of austenite at the same temperature. Figure 3.2.b shows the magnetization versus applied field response of $Ni_{51.1}Mn_{24.0}Ga_{24.9}$ single crystal at 25 ˚C and -125 ˚C, at austenite and martensite phases, respectively. Saturation magnetization and critical field for saturation are higher for martensite than austenite due to low temperature and high MAE. The step-like behavior on the martensite magnetization curve of Figure 3.2.b in between 3 kG and 6 kG (marked by arrows) can be attributed to the variant reorientation due to applied magnetic field.

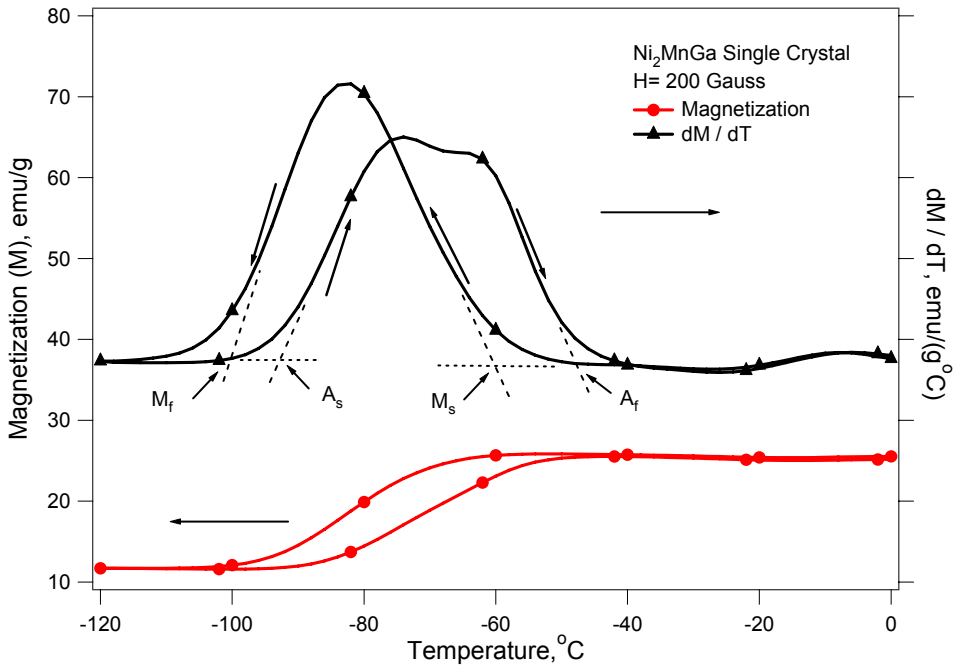


**Figure 3.1** Magnetization as a function of temperature under magnetic field of 200 Gauss, as well as its derivative showing the transformation temperatures for the parent to I-phase to 10M martensite transformation sequence.

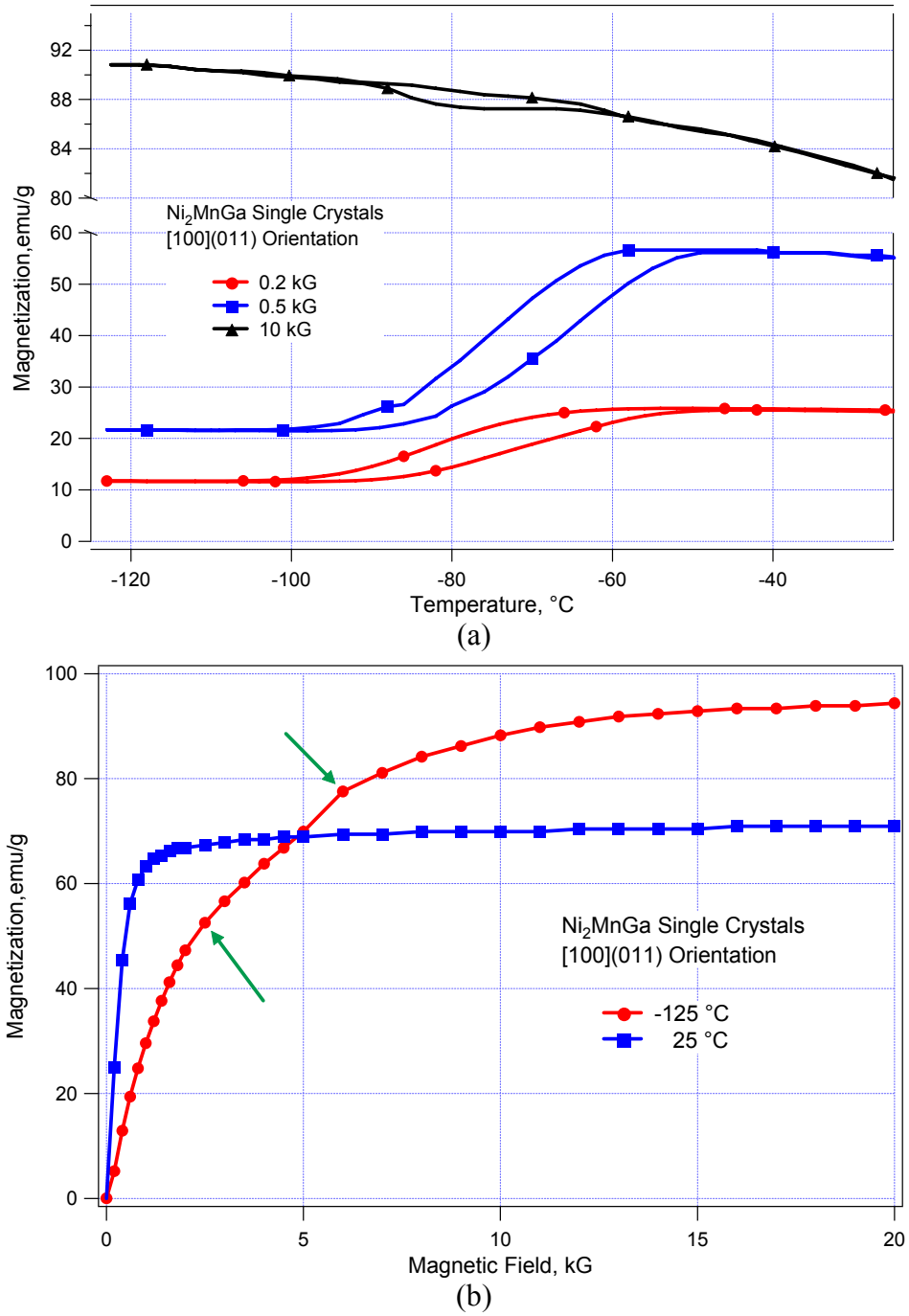


**Figure 3.2.** a) Evolution of magnetization as a function of temperature under constant magnetic fields of 200 G, 500 G and 10 000 G. b) Change in magnetization with applied magnetic field at -125 °C and 25 °C in fully martensitic and austenitic phases, respectively.

### 3.2 Conventional Shape Memory Effect

As discussed in Chapter I, thermal cyclic under stress results in selection of certain variants and external strain can be observed. Figure 3.3 shows cooling heating response of a $Ni_{51.1}Mn_{24.0}Ga_{24.9}$ single crystal where 10 MPa is applied along the [100] orientation initially at 25 ˚C under no magnetic field. Since the detwinning stress of 10M martensite is relatively low applied stress results in formation of a single variant of tetragonal martensite with short c-axis along the applied stress and as a result, 3.8 % macroscopic strain is observed under 10 MPa. Higher stress values do not increase the strain magnitude. The austenite to martensite transformation temperature is around -80 ˚C while the back transformation occurs at -67 ˚C. The strain response changes from a continuous to a sudden jump type behavior when stress is applied. This behavior indicates the formation and fast movement of a single martensite variant and insignificant barrier to the phase front motion.

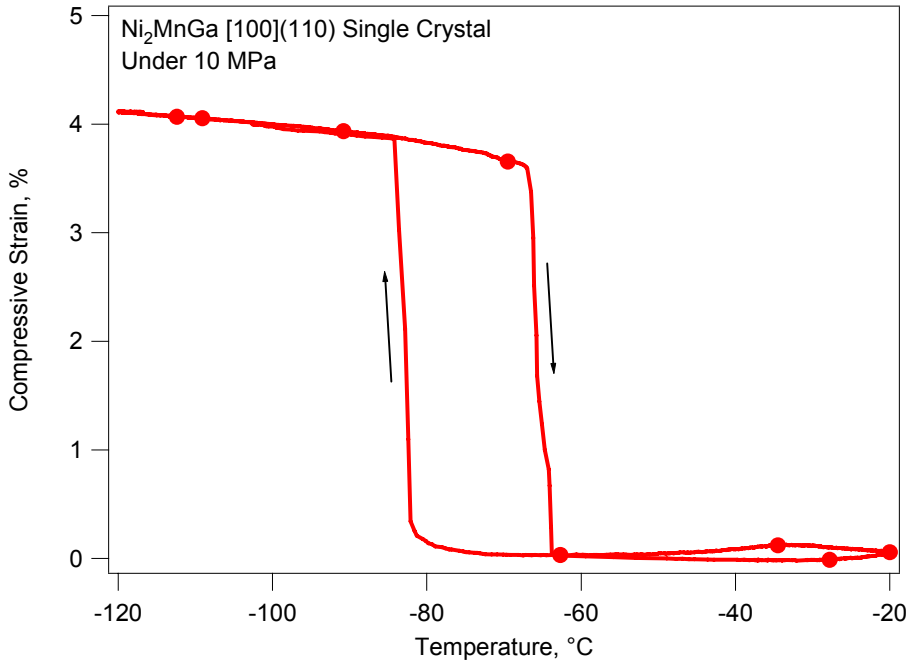


**Figure 3.3** Cooling-heating response of $Ni_{51.1}Mn_{24.0}Ga_{24.9}$ single crystal under a compressive load of 10 MPa along the [100] orientation.

It is possible to calculate theoretical maximum strain for austenite to martensite phase transformation from lattice correspondence and lattice parameters of austenite and martensite. If the stress applied during cooling is enough for single variant formation, a single variant of martensite with the shortest axis along the applied stress direction can be obtained. In our experiments the stress direction was [100]. If we use the lattice parameters of $a_m$= 0.595 nm $c_m$=0.560 nm for10M martensite and $a_a$= 0.584 nm for austenite theoretical phase transformation strain can be determined as [48];

$$\frac{a_a - a_m}{a_a} = 4.1\% \qquad (3.1)$$

Lattice parameter of austenite is used in denominator since the strain is measured in the experiments with respect to austenite as the reference configuration.

The theoretical value for maximum strain for phase transformation, 4.1 %, is close to the obtained experimental value of 3.8 % which indicates the high quality of the single crystals. It is also important to note that lattice parameters of phases, especially for 10M structure are functions of temperature which could help to explain the small difference.

### 3.3 Magnetic Field-Induced Strain by Variant Reorientation under Constant Stress

The evolution of MFIS with applied magnetic field under constant compressive stress and temperature are shown in Figures 3.4.a and 3.4.b for increasing and decreasing stress levels from 2 MPa to 6 MPa and 5 MPa to 1 MPa, respectively. Before each test, the stress of 6 MPa was applied and unloaded to the desired stress level in order to obtain the same single variant martensite morphology. 6 MPa was sufficient to restore the initial strain level under each stress was set to zero in the figures for ease of comparison. A total of three magnetic field cycles were applied between 16 kG and -16 kG. The response under both increasing and decreasing stress levels are presented to show that there is no significant change in the strain and hysteresis trends.

In Figure 3.4, there is a significant difference between the first and second cycle responses although the difference between the second and third cycles is negligible

under all stress levels. The first cycle under 2 MPa marked in Figure 3.4.a is the first variant reorientation step of the virgin sample. In this case, the magnetic field level is 5 kG higher for the onset of the reorientation than the ones in the following cycles. This is attributed to the difficulty of nucleation of a new variant during the first cycle which vanishes with field training.

The MFIS response is a typical butterfly response which is also observed in ferroelectric crystals [82]. The curves are symmetric since the magnetic force on a twinning dislocation is insensitive to the sign of the magnetic field [83]. As the applied magnetic field is increased, MFIS starts to evolve after a certain threshold field is reached and stops at a higher field magnitude. Further field increase does not affect the MFIS. Since the maximum strain from magnetostriction is only about 0.01% [32], the observed MFIS is solely due to martensite reorientation. Maximum strain levels and critical fields for the reorientation start and finish depend on the applied stress level. As a rule of thump, as the stress level increases, MFIS decreases since available magnetic field energy is spent by the mechanical energy from the applied stress and the energy required for twin boundary motion. The higher the opposing mechanical energy is, the lower the energy is used for detwinning. Depending on the stress levels, when the magnetic field is reduced and switched off, martensite variant favored by the field reorients back to the original variant favored by the stress. From Figure 3.4.b, it is clear that 1 MPa is not sufficient for full back reorientation, at least 3 MPa is needed. Therefore, the detwinning stress can be estimated as in between 1 to 3 MPa.

To better understand the cycle effect, the first and second cycle responses are plotted separately in Figure 3.5.a and 3.5.b, respectively. Although the maximum MFIS decreases with stress level for the first cycle, it surprisingly increases first and then decreases in the second cycle. Moreover, the maximum MFIS for the first cycle is always greater than the one for the second cycle. The blocking stress is about 5 MPa. The irrecoverable MFIS which is the MFIS difference between the first and second cycles decreases with stress level and vanishes completely for the stress levels of 5 MPa

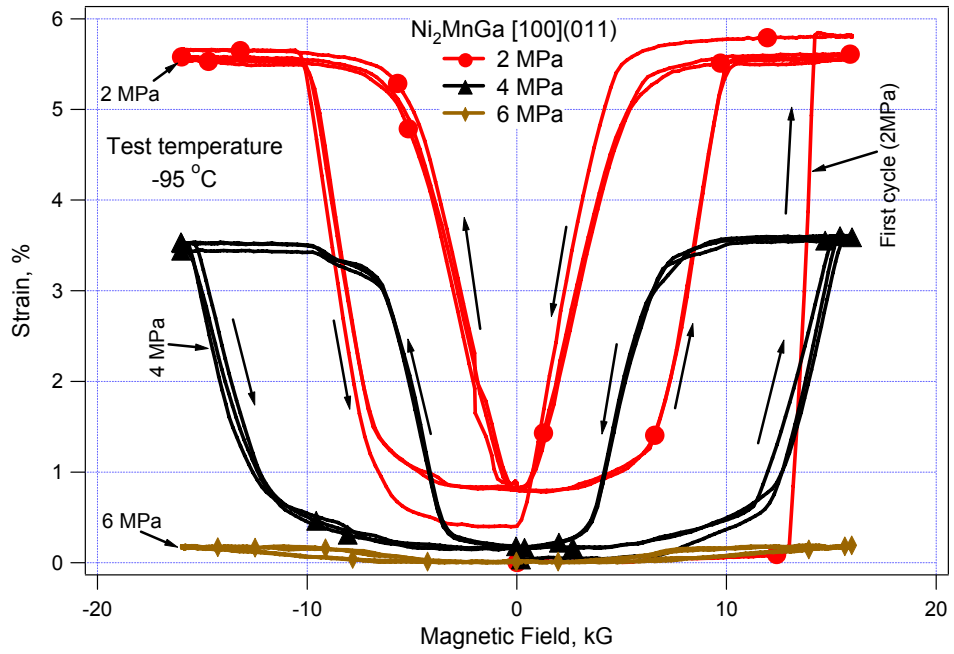


**Figure 3.4** Evolution of strain in the $Ni_{51.1}Mn_{24.0}Ga_{24.9}$ single crystals as a function of magnetic field under different constant compressive stress levels at -95 °C. Three cycles are shown. a) Increased stress levels from 2 to 6 MPa, b) decreased stress levels from 5 MPa to 1 MPa. Only selected cases are shown for clarity.

and higher. It is also clear in Figure 3.5.b that the critical magnetic field needed for martensite reorientation increases with stress magnitude.

The measured first and second cycle MFIS data have been collected to construct the maximum MFIS vs. stress plot shown in Fig. 3.6. Previously reported MFIS levels are also included for comparison [26, 31, 46, 48]. The overall highest first cycle MFIS of approximately 6.0 % was measured by Murray et al. [46], under 0.8 MPa, while in the present study the maximum MFIS of about 5.8% was measured under 1and 2 MPa. The general trend of all the plotted curves is that the first cycle MFIS decreases with increasing stress levels, until, at the blocking stress level, no strain related to variant reorientation is induced by the magnetic field. For the second cycle, MFIS increases from 3.2% to 4.9% as the stress increases from 1 MPa to 2 MPa. MFIS under 2 and 3 MPa are the same and further increase in stress decreases the MFIS magnitude. For stress levels higher than 4 MPa, the first and second cycle responses coincide. The difference in the MFIS for the first and second cycle stems from the fact that the stress levels are not sufficient for full back reorientation upon unloading the field after the first cycle. The strain magnitudes around 4-6 % under 2-4 MPa in the present study are the highest reported so far [26, 31, 46, 48].

Theoretical maximum martensite reorientation strain can be obtained by transformation of single variant martensite with short axis along the compression direction to another single variant martensite with long axis along the compression direction and vice versa. If the given parameters ($a_m$= 0.595 nm $c_m$=0.560 nm for10M martensite and $a_a$= 0.584 nm for austenite [48]) are used maximum strain for martensite reorientation is;

$$\frac{a_m - c_m}{a_a} = 6.0\,\% \qquad (3.2)$$

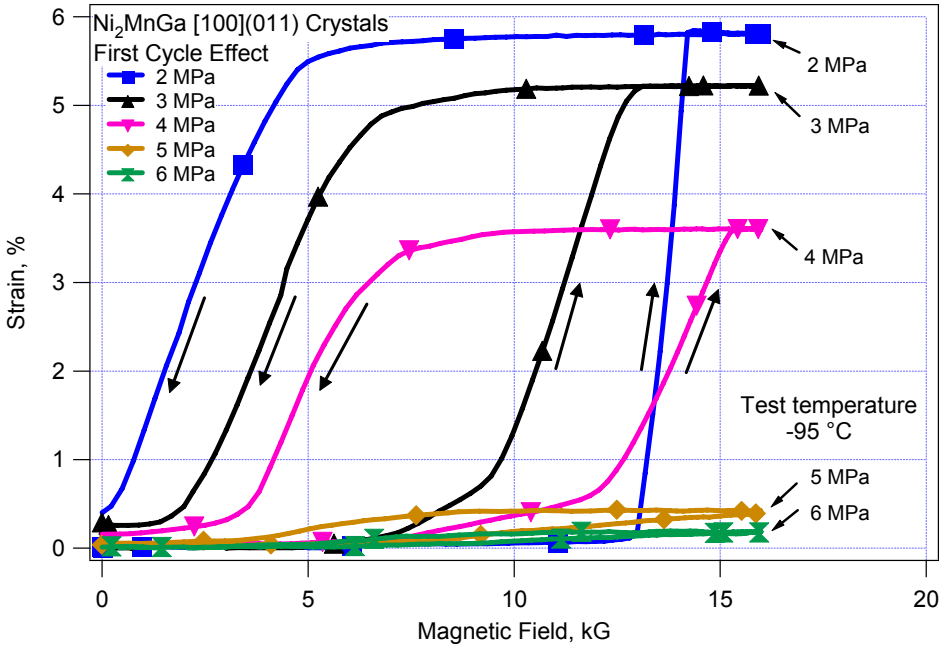


(a)

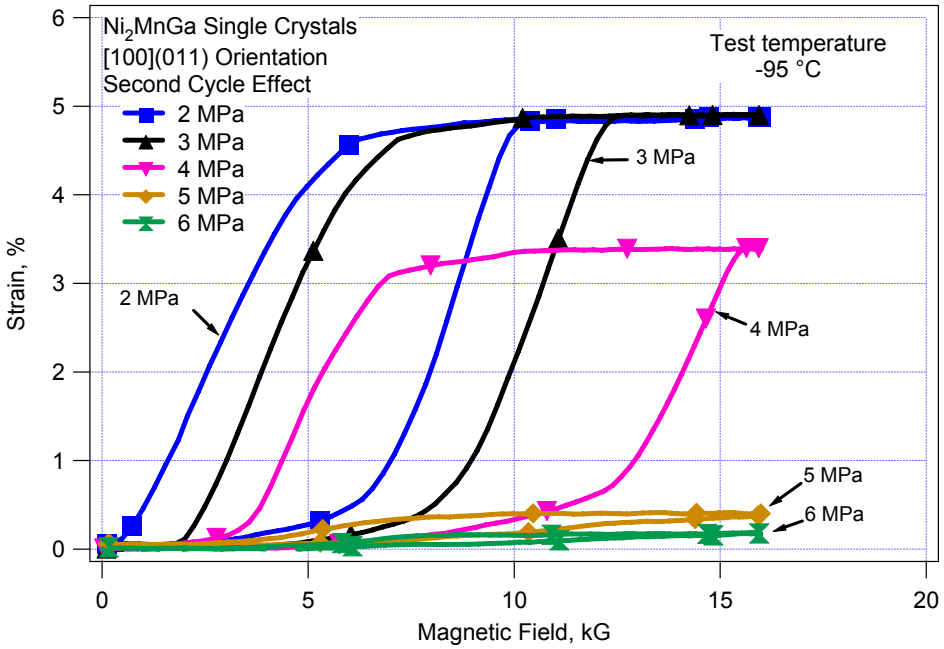


(b)

**Figure 3.5** Magnetic field-induced strain response during the a) first and b) second magnetic field cycles under constant stress levels.

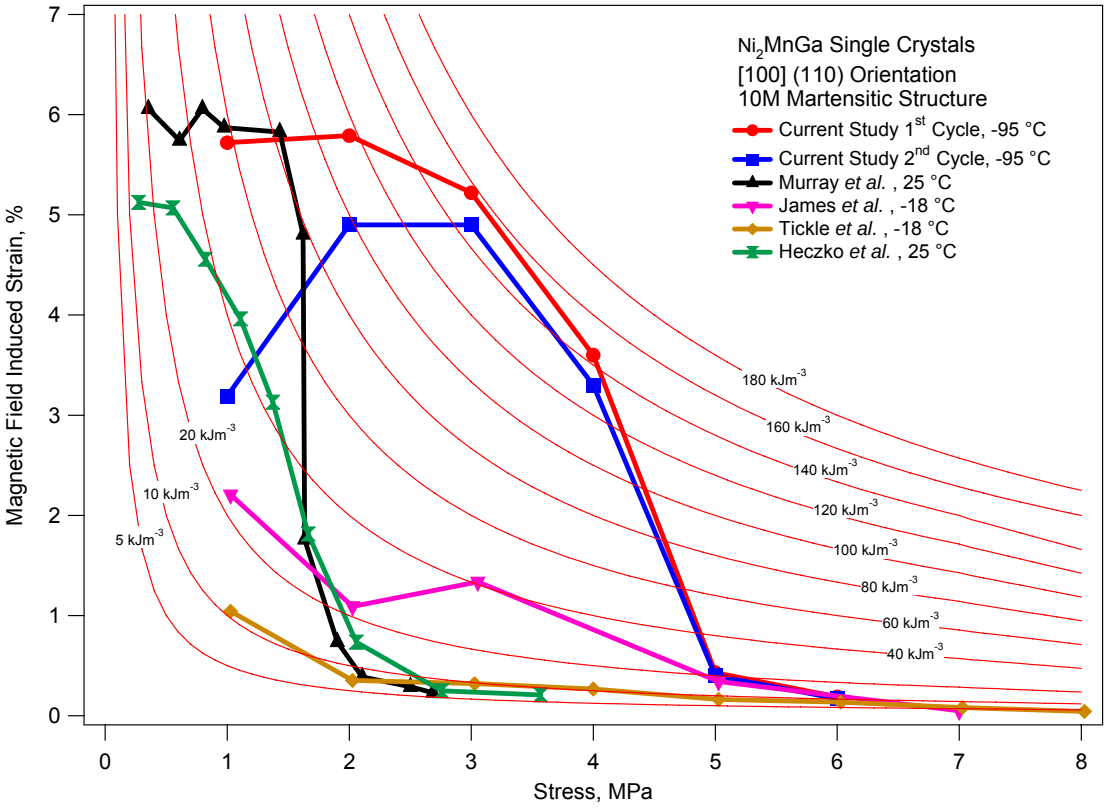


**Figure 3.6** Comparison of maximum MFIS as a function of stress for the current study and literature data. A grid of constant actuation work output hyperbolas ranging from 10 to 180 $kJm^{-3}$ has been superimposed.

Higher values could be obtained if single variant martensite with easy axis along the measured direction is set as the reference. For this case, the maximum strain for the reorientation is;

$$\frac{a_m - c_m}{c_m} = 6.25\,\% \qquad (3.3)$$

In our results austenite is taken as the reference configuration since there is always a possibility not to form only one single variant of martensite with transformation. Theoretical values for maximum strain for martensite reorientation, 6 %, and phase transformation, 4.1 %, are very close to the obtained experimental values 5.8 % and 3.8 %, respectively.

The blocking stress in the experiments conducted at room temperature by Murray *et al*. [46] and Heczko *et al.* [48] is about 2 MPa where it is around 5 MPa in the present study. The results reported by Tickle *et al.* [26] show a similar blocking stress level but the maximum MFIS of 2% is considerably lower. The blocking stress, however, is not easily identified, since at very low strain levels ordinary magnetostriction of MSMA materials can no longer be neglected [5, 84].

The stress levels and maximum MFIS only provide limited information about the actuation performance of these materials. A better measure is the actuation work output per unit volume, $W = \sigma \times \mathrm{MFIS}_{max}$, where $\sigma$ is the stress, held constant during the experiment, and $\mathrm{MFIS}_{max}$ is defined at that given stress. To compare the actuation performance of some of the published $Ni_2MnGa$ MSMA compositions with the present results, we considered the mechanical work output per unit volume as a figure of merit and added to Figure 3.6.

The maximum work output for the present composition is calculated to be 157 $kJm^{-3}$ and 147 $kJm^{-3}$ for the first and second cycles, respectively, whereas the compositions studied by Murray *et al*. [26, 46, 48], Heczko *et al.* [48] and Tickle [26, 46, 48]have maximum work outputs of 83 $kJm^{-3}$, 44 $kJm^{-3}$ and 41 $kJm^{-3}$, respectively. This represents an increase in the actuation work output of more than 100 % in the present study.

The major difference between the present case and the prior studies is the operating temperature and martensite start temperature. Although the compositions are slightly different, the saturation magnetization and $T_c$ do not change significantly with composition in near Heusler compositions of NiMnGa [11, 12]. Since there is a large gap between $T_c$ and $T_o$ as compared to the $T_c$-$T_o$ window in the previous studies, the MAE must be significantly higher in the present case. Moreover, the $T_o$ is right below the martensite finish temperature, and thus, the detwinning stress is at its minimum possible value. Since the applied magnetic field has to overcome the externally applied stress and detwinning stress, the minimum detwinning stress maximizes the blocking stress with available stored MAE. Figure 3.7 shows two schematics to identify the

blocking stress levels for two cases with the same Curie temperature but different $M_s$ and operating temperatures. In Figure 3.7.a $M_s$ is high and $T_o$ is chosen to be close $M_s$. The upper line (red) shows the detwinning stress which increases as temperature decreases. The lower curve (blue) shows the magnetostress calculated by dividing the $K_u$ with $\varepsilon_0$, the transformation strain. Magnetostress increases as temperature decreases since saturation magnetization increases as temperature decreases [28, 30]. In this case both the $T_c$ -$T_o$ and $M_s$-$T_o$ are small resulting in both low magnetostress, $\sigma_{mag}$, and detwinning stress, $\sigma_{detwin}$. The blocking stress can be defined as $\sigma_{mag}$- $\sigma_{detwin}$ and shown in the figure as operating stress range. It is clear that, as far as $\sigma_{mag} > \sigma_{detwin}$ MFIS can be obtained and with decreasing temperature blocking stress decreases due to more rapid increase in detwinning stress than magnetostress. After certain temperature MFIS cannot be obtained. Thus, simply decreasing the temperature will not improve blocking stress levels. Figure 3.7.b shows the schematic for a sample with the same $T_c$ but lower $M_s$ and $T_o$. In this case $T_c$ -$T_o$ is large and $M_s$-$T_o$ is small resulting in high $\sigma_{mag}$ and low $\sigma_{detwin}$, thus a high blocking stress. Magnetostress curve is held constant while detwinning stress curve is shifted to lower temperatures since $T_c$ is considered to be constant while $M_s$ shifted to lower temperature.

### 3.4 Strain Response under Incremental Magnetic Field

In order to better understand the evolution of MFIS and irrecoverable strain with applied magnetic field, magnetic field is cycled between zero and the incrementally increasing field magnitude under constant stress of 3 MPa. Starting from 2 kG, the maximum applied magnetic field is increased 1 kG at every cycle and eventually reached to 16 kG. 3 MPa is chosen due to its high maximum first and second cycle strains and low strain difference between the first and second cycles. Figure 3.8.a shows the incremental evolution of MFIS with incrementally increased applied magnetic field. Maximum MFIS and irrecoverable strain values are also included in the figure as a function of maximum applied magnetic field magnitude. Figure 3.8.b shows MFIS and applied magnetic field as a function of time.

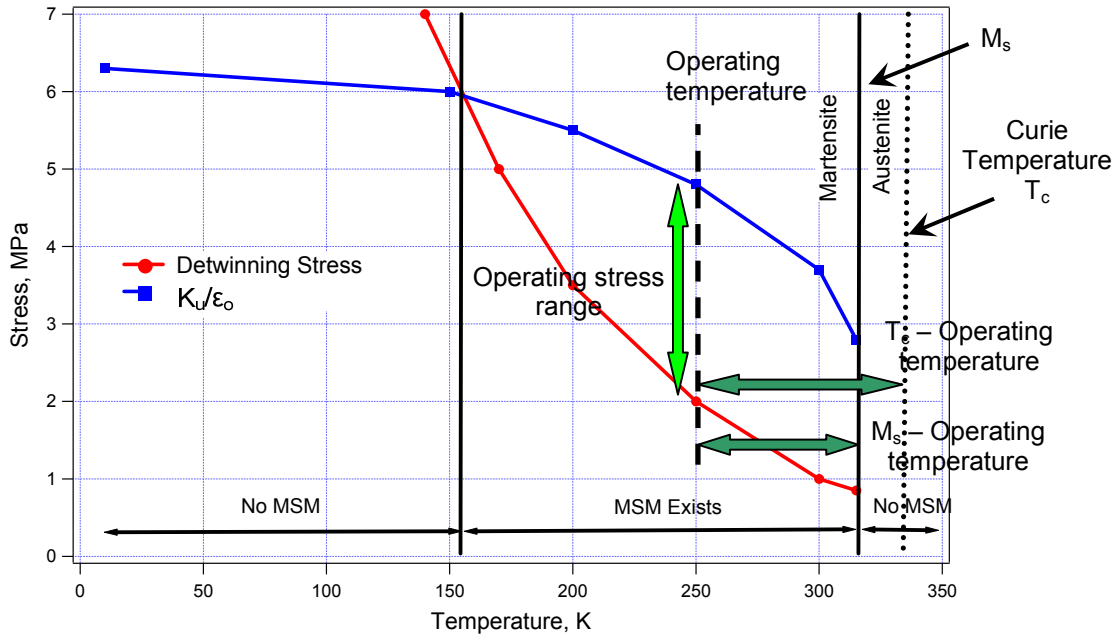


(a)

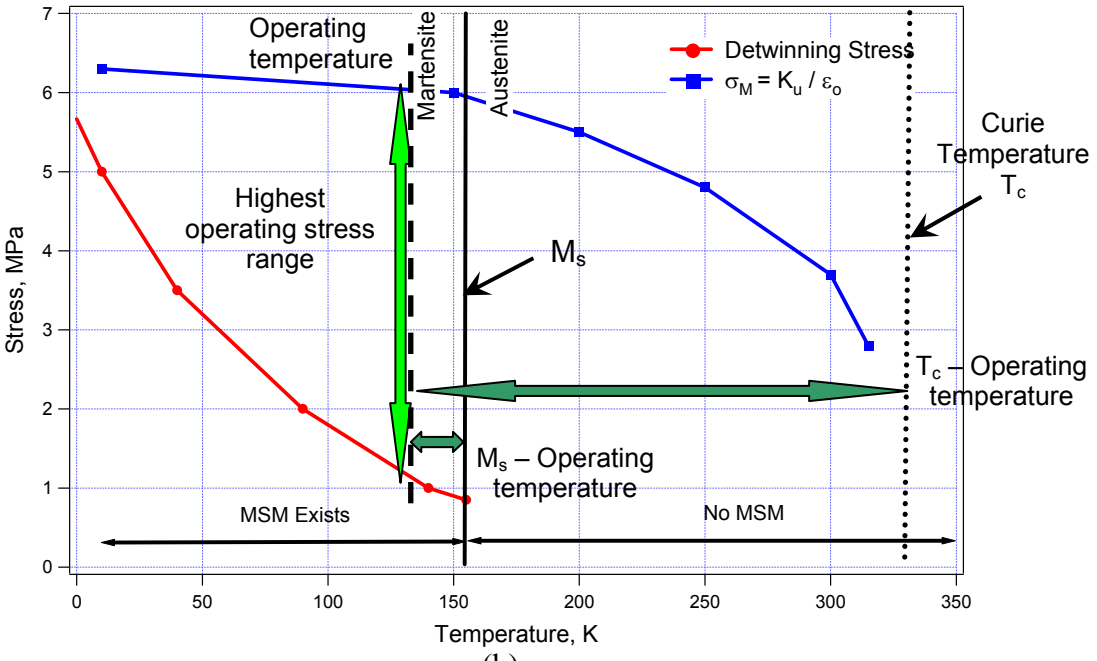


(b)

**Figure 3.7** Two schematics to identify the blocking stress levels for two cases with the same $T_c$ but different $M_s$ and operating temperatures: a) $M_s$ temperature is high and b) $M_s$ temperature is low, $T_o$ is kept close to $M_s$.

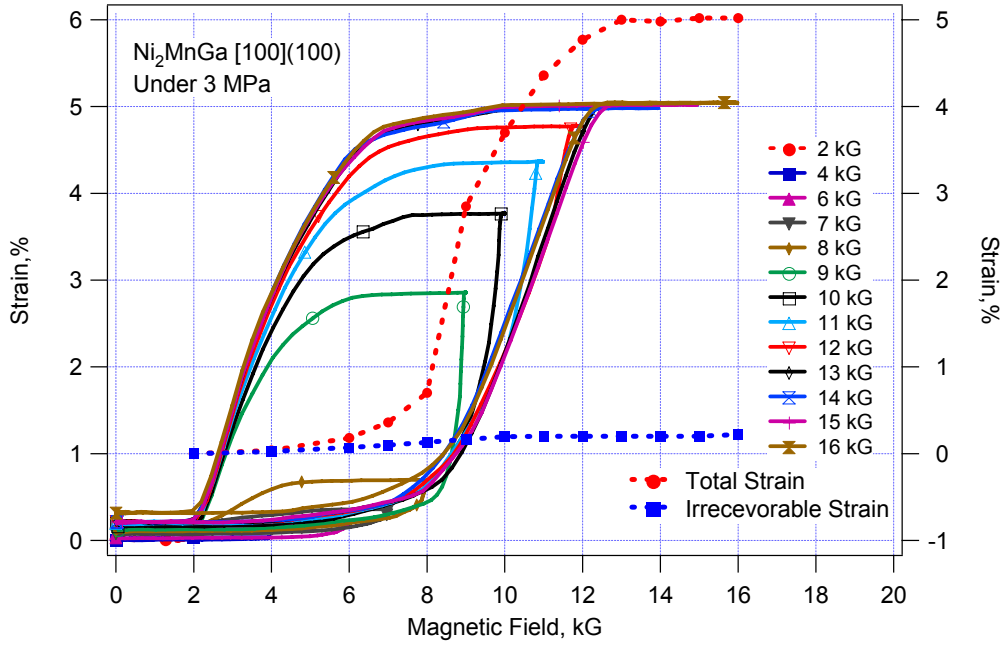


(a)

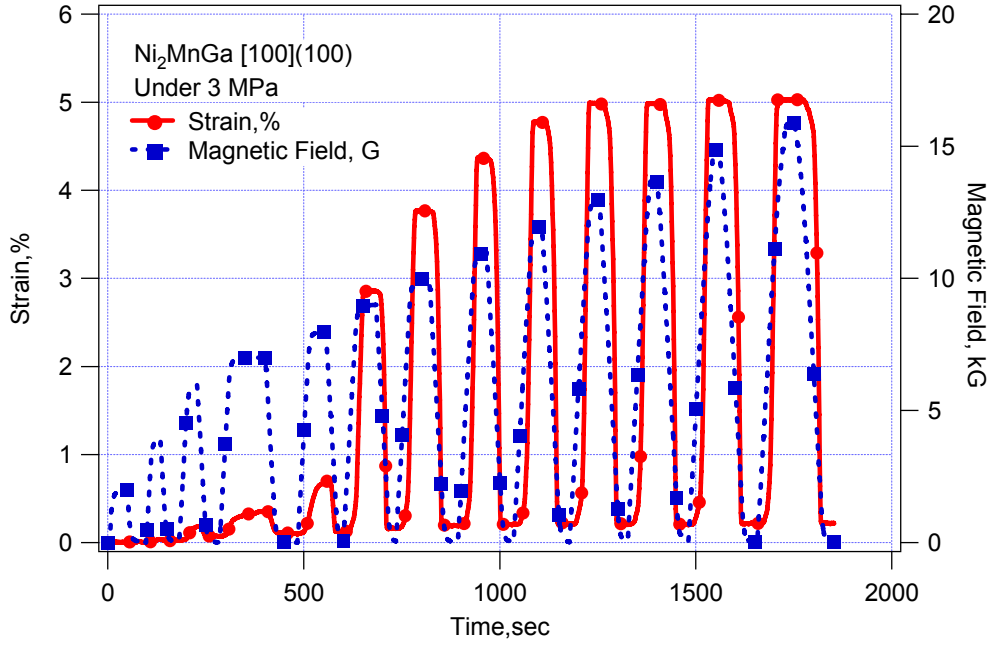


(b)

**Figure 3.8** Incremental applied magnetic field experiment results under constant stress of 3 MPa. a) MFIS response with applied magnetic field magnitude increased from 2 kG to 16 kG with increments of 2 kG. Maximum and irrevocable strain levels are shown on the right column, b) MFIS (left) and applied magnetic field (right) responses with time.

As expected, MFIS increases with fields above 6 kG and reaches saturation at 13 kG . MFIS increases from 0.68 % to 2.85 % between the fields of 8 kG and 9 kG and reaches to maximum strain of 5.05 % at 13 kG. Irrecoverable strain starts after 6 kG and saturates at 10 kG with maximum magnitude of 0.2 %. It is important to note that, the strain continues to increase when the magnetic field is reached to 9 kG and held constant. Glavatska *et al.* [85] reported that NiMnGa gradually deforms under constant magnetic field in a manner analogous to mechanical creep. The continuation of strain evolution may be related to the inertial effects of the twin boundary motion and creep-like behavior of MSMAs.

### 3.5 Magneto-Microstructural Mechanisms for Variant Reorientation

To better understand the MFIS evolution, Figure 3.9 shows a schematic for the magnetic field induced variant reorientation mechanism of MSMAs. The MFIS and the corresponding magnetization (along the applied magnetic field) vs. magnetic field responses are also included in the figure [86]. Initially, the single crystal is austenitic at room temperature as shown by #1. If the sample is cooled down under no external stress, a self accommodating martensite structure forms and, thus, the dimensions of the sample do not change, shown as #2a. Externally applied stress (compressive in the present case) after cooling favors the variant with the short axis along the compressive stress direction and eventually a single variant martensite is obtained, shown as #3a, resulting in a net compressive strain ($\varepsilon_{3a}$). The same single variant martensite (variant 1) can be obtained if enough compressive stress is applied during cooling from austenite.

In terms of magnetization, the magnetic domains, in which the magnetization direction is along the short axis (easy axis) of the tetragonal martensite in the $Ni_2MnGa$ alloys, form during phase transformation. The direction of the domains can alter 180˚ since the overall magnetization must vanish under no magnetic field. For the single variant case shown as #3b, vertical magnetic domains are present after cooling under stress. For the multivariant case shown as #2a, more complex structure with twins and magnetic domains forms as shown by #2b. When a magnetic field perpendicular to the

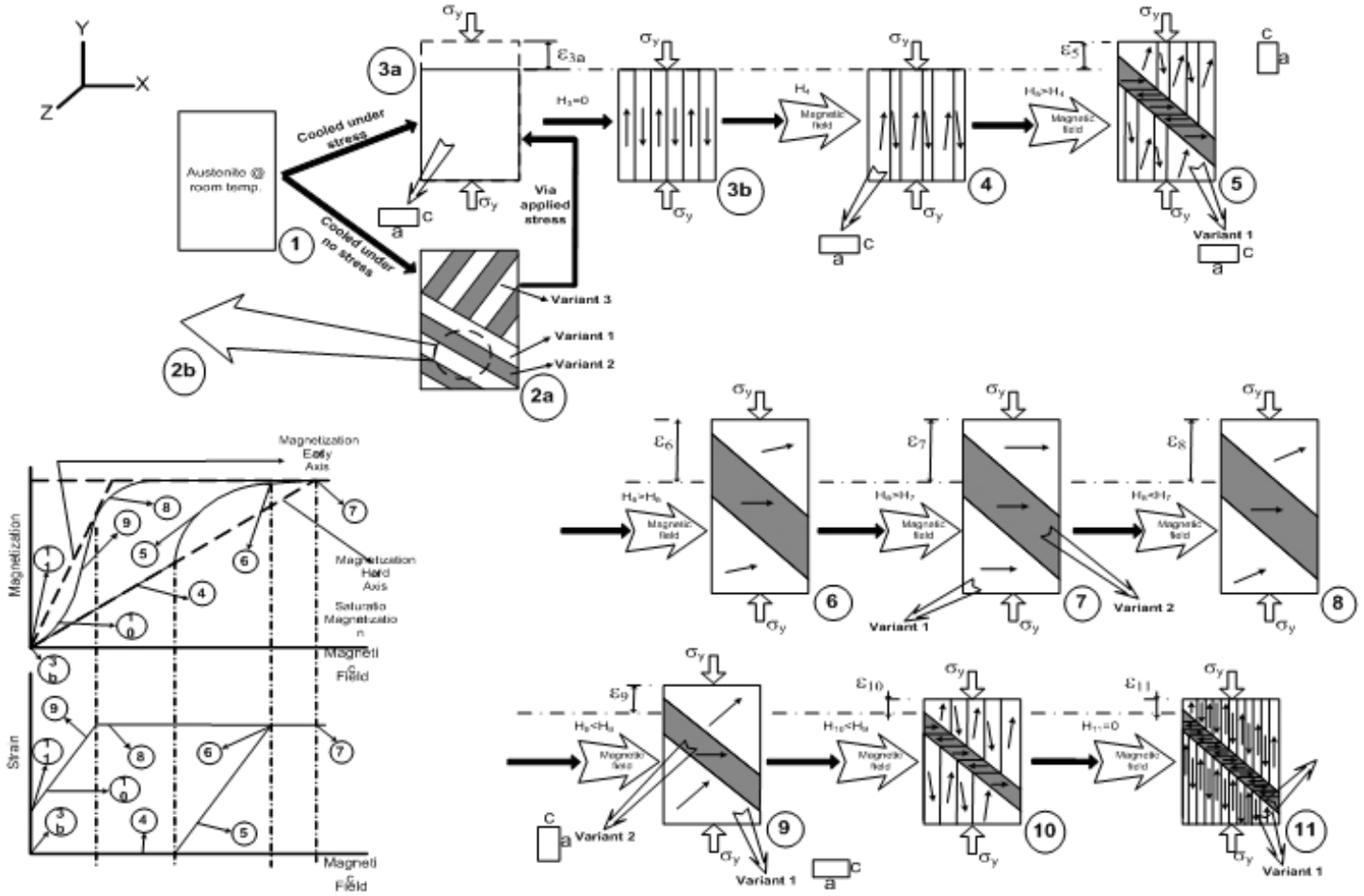


**Figure 3.9** A schematic of the magneto- and microstructural mechanisms for variant reorientation mechanism in MSMAs

compression direction is applied both domain wall motion and magnetization rotation occur, shown as #4 [87, 88]. It is known that relatively low magnetic field magnitudes are required for domain wall motion as compared to that for variant reorientation [34, 89]. Consequently, domain wall motion and magnetization rotation take place simultaneously before martensite reorientation starts around 5 kG.

When the energy required for detwinning is smaller than the MAE, another martensite variant (variant 2) with easy axis along the applied field direction is induced, as shown by #5. The magnetization direction of variant 1 further rotates at #5 with respect to #4 since the field magnitude is higher. The magnetization response in the schematic follows the magnetization path for the hard axis until the variant 2 starts to nucleate. Since the easy axis of the variant 2 is along the measured magnetization direction, total magnetization increases rapidly with the evolution of MFIS. The volume fraction of the second variant increases with further field increase and the case #6 shows the magneto and microstructural configuration when the reorientation process stops.

It is important to note that, as the volume fraction of the variant 2 increases, anisotropy energy decreases because it depends on the volume fraction of the variant 1. On the other hand, further increase in magnetic field results in more magnetization rotation in the variant 1 which leads to an increase in the MAE. These two effects oppose each other and at some point cause the reorientation process to cease before completion even if the magnetization rotation still continues with increasing magnetic field.

The incomplete reorientation can be attributed to the difference between the nucleation and propagation barriers for new variants. In NiMnGa and ordered martensites in other shape memory alloys, new variant nucleation is much more difficult than propagation and the propagation usually occurs in a Lüders' type fashion. In the present case, once the second variant nucleates, the energy required for the propagation is much less than the one for the nucleation and thus, the propagation occurs relatively fast. This reduces the volume fraction of the variant 1 and thus MAE in a much faster rate than the increase in MAE due to the magnetization rotation. Moreover, as the

reorientation strain increases, it becomes more and more difficult to complete the reorientation. Therefore, the increase in MAE due to the magnetization rotation may not compensate the opposing energy from the externally applied stress, strain hardening effect, decrease in MAE due to volume fraction change and some other effects such as internal barriers, boundary and surface interactions to complete the reorientation process (the case #6). Thus, the observed MFIS level can be less than the theoretical strain and further increase in magnetic field may not increase the strain level.

When the field magnitude reaches the saturation magnetic field of the hard axis, the magnetization direction of the variant 1 completely rotates towards the applied field direction, shown as #7. When magnetic field starts to decrease, the applied stress works against the field and lattice friction. Magnetization direction of the variant 1 rotates towards the easy axis direction as shown by the case #8 and MAE decreases. After a threshold value, the MAE may not be sufficient to favor the second variant anymore and the reorientation of the variant 2 to the variant 1 could start as shown by the case # 9. Further decrease in magnetic field increases the volume fraction of the first variant. After reaching a certain field magnitude, magnetic domains may form as shown by the case # 10. Decreasing the magnetic field below a blocking magnitude which is a function of the applied stress level does not result in any further reorientation of martensite. Final microstructural configuration is shown as the case # 11. The irrecoverable strain, i.e. $\varepsilon_{11}$, is proportional to the volume fraction of the residual second variant and depends on the applied stress level.

During the second magnetic field cycle, the reorientation mechanism is similar to the one for the first cycle. The structural evolution follows the path from the case #11 to the case #7 during the magnetic field loading and from the case #7 to the case #11 during unloading leading to fully recoverable reorientation. The third cycle response is the same as the second cycle response without considerable differences in the hysteresis or irrecoverable strains.

### 3.6 Effect of Magnetic Field Rate on Magnetic Field-Induced Strain

Different field rates were applied to monitor the rate effect on the evolution of MFIS under 3 MPa. Initially two cycles between zero and 16 kG were conducted with a field rate of 250 G/sec to stabilize the hysteresis loops. Then, the field rate was set between 25 G/sec and 500 G/sec and one cycle was recorded at each rate. In Figure 3.10.a, the response changes from one-step reorientation to two-step as the field rate decreases. The strain magnitude decreases from 5.2% to 4.6% as the rate decreases from 500 G/sec to 25 G/sec. Moreover, the magnetic hysteresis has a tendency to increase with the field rate. Figure 3.10.b shows the maximum cyclic MFIS magnitudes for the first and total transformation as a function of field rate. The field rate also determines whether the reorientation is one-stage or two-stage. For the rates lower than 150 G/sec, the reorientation is two-step which is shown by a dotted line in the figure. The MFIS for the first step also increases with the field rate.

Figure 3.11 shows the MFIS response with field rate of 50 G/sec during the cyclic behavior under 2 MPa. In the first cycle magnetic field is reversed at the end of the first stage reorientation and in the second cycle maximum field of 11 kG is applied. When the field is unloaded in the first cycle after reaching the end of first step, the back reorientation starts at 4 kG and completes at 1.2 kG. If the field is unloaded from 11 kG after completing the second step reorientation then the first back reorientation step starts at 7 kG and finishes at 3 kG while the second step back transformation starts at 2.5 kG and finishes at 1.2 kG. Magnetic field hysteresis for both stages is very close.

The observed rate dependency can be attributed to the difference between the nucleation and propagation barrier strengths for twins. At lower rates, the reduction in MAE due to both the twin boundary motion and the decrease in the volume fraction of the variant 1, (initial variant), occurs in a much faster rate than the increase in MAE due to the magnetization rotation in the variant 1. The two-stage reorientation is observed because once some propagation occurs and the MAE is quickly reduced, the propagation stops due to this fast reduction. Higher field levels are required to increase the MAE to

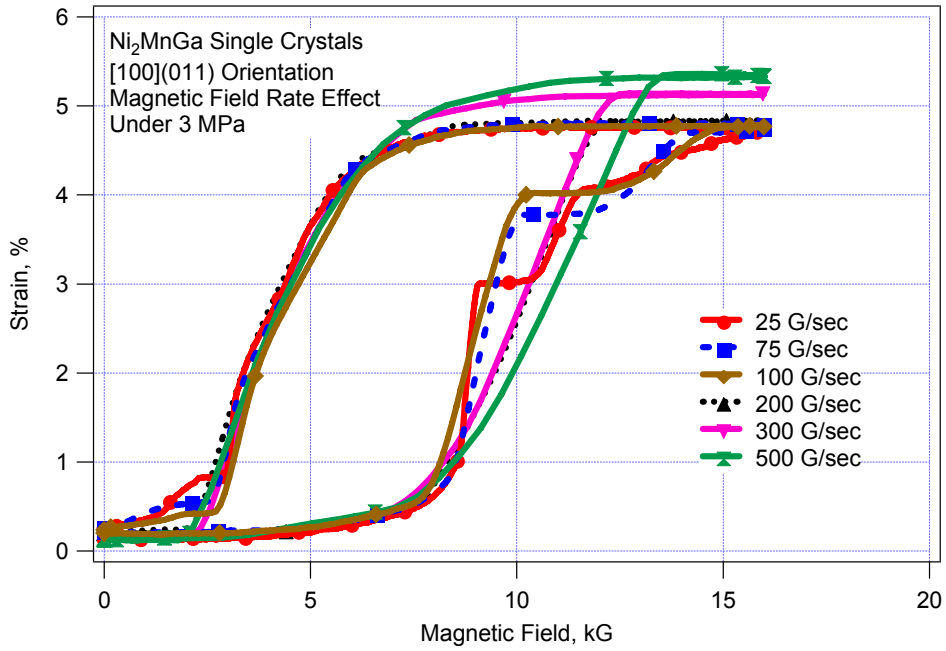


(a)

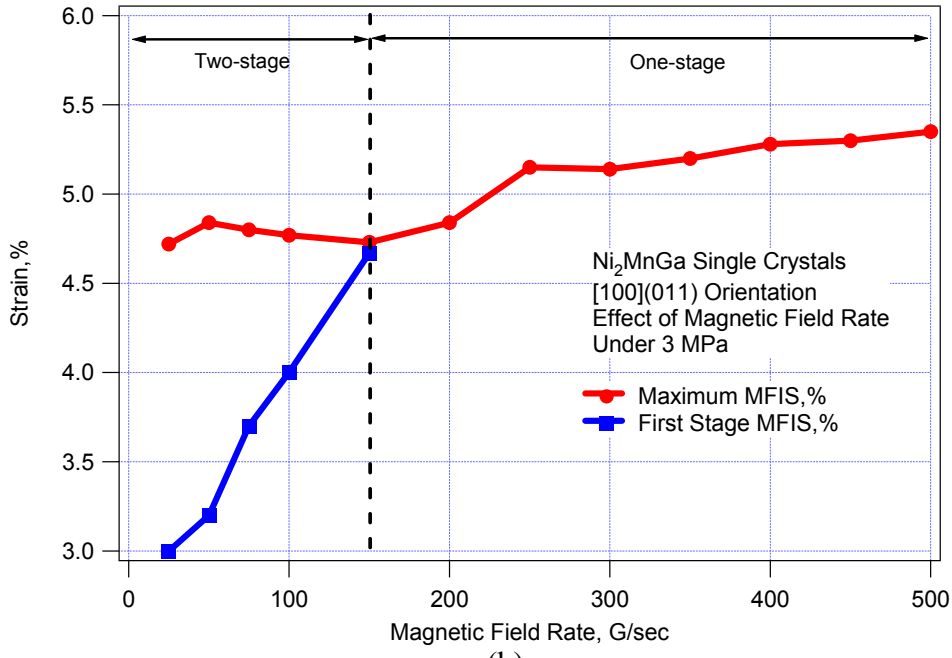


(b)

**Figure 3.10** a) Effect of magnetic field rate on the MFIS evolution under 3 MPa showing two-stage reorientation, b) maximum and first stage MFIS magnitudes as a function of field rate.

sufficient levels for the propagation to start again because more energy is needed than the one required for the propagation itself. If the field rate is sufficiently high, the magnetization rotation occurs faster. Thus, at higher field rates, accompanying magnetization rotation and increase in MAE can compensate the decrease in energy due to the volume fraction change. This leads to the observation of one step reorientation and higher strain levels as compared to the response under low field rates since the available energy is not spent for restarting the propagation. The creep-like behavior observed in NiMnGa alloys is neglected due to short time span in these experiments.

### 3.7 Stress-Induced Martensite Reorientation under Constant Magnetic Field

In this section, instead of holding stress constant and applying magnetic field as in the previous sections, compressive stress is applied under constant applied magnetic field with a rate of 0.2 MPa/sec.

Figure 3.12 shows the effect of magnetic field on the stress-strain behavior of martensite at -95 ºC. Prior to each experiment, single variant martensite was obtained by applying 16 kG under 1MPa as a reference starting point. Then the magnetic field was set to the desired field magnitude and maximum stress of 14 MPa was applied in each case. The applied magnetic field magnitude was decreased 2 kG after each test but for clarity only selected responses are shown. Starting strains for the 4 kG and 0 G cases are not at zero since some back transformation occurred during decreasing the magnetic field from 16 kG to 4 kG and 0 kG.

In Figure 3.12, when stress is applied, there is an elastic deformation of single variant martensite followed by the reorientation to the second variant and elastic deformation of the second variant. It is clear that, the applied field shifts the stress levels considerably up. The stress-strain behavior under magnetic fields at and above 8 kG is similar to the rubber-like or pseudoelastic response of shape memory alloys. The incomplete back transformation under 4 kG and 0 kG cases are completed when a magnetic field of 16 kG is applied after unloading.

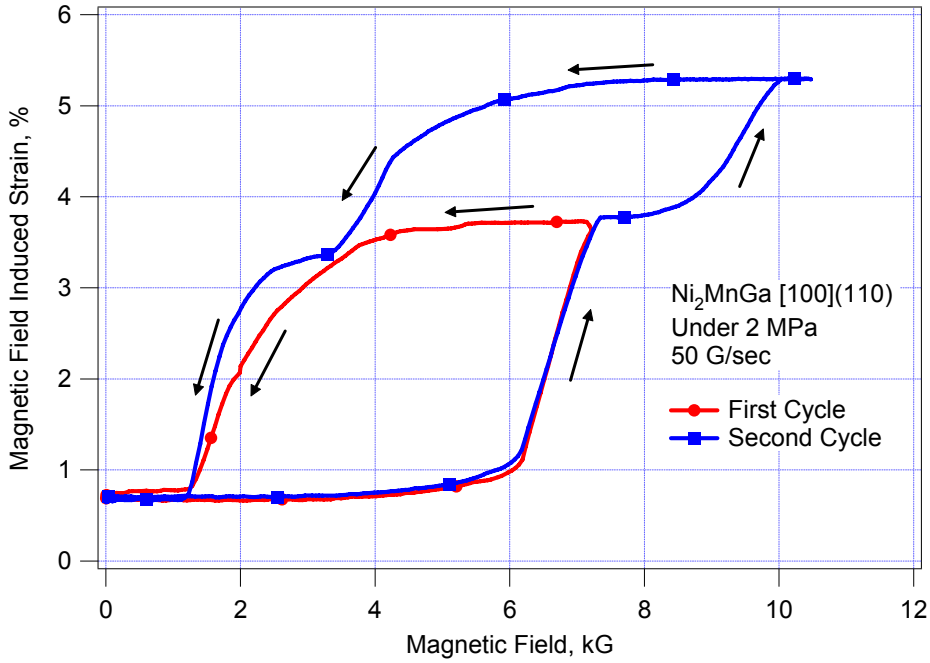


**Figure 3.11** MFIS response of the $Ni_{51.1}Mn_{24.0}Ga_{24.9}$ single crystals under 2 MPa constant stress with magnetic field rate of 50 G/sec showing two step reorientation behavior in detail.

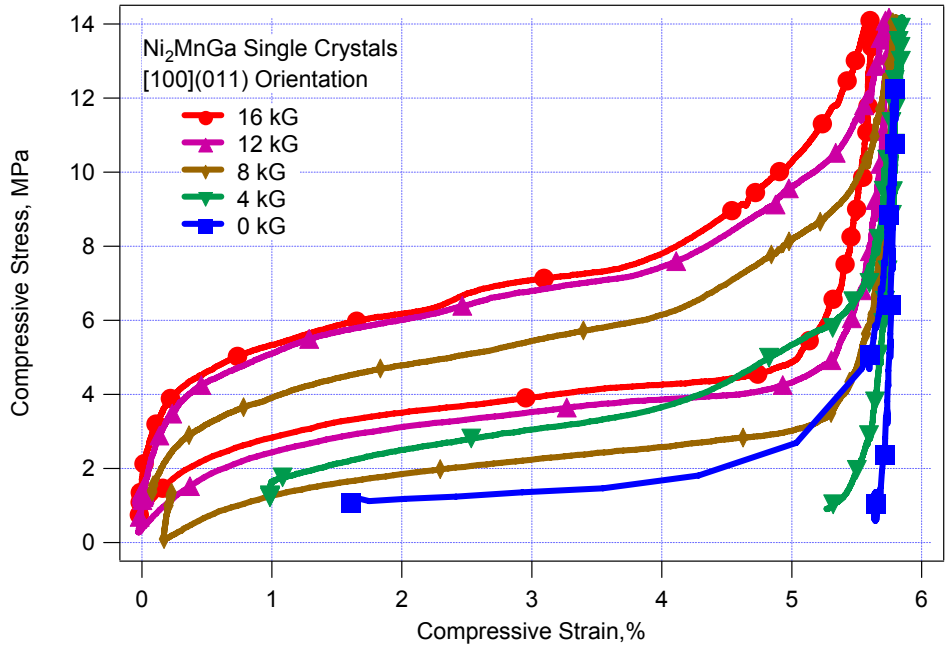


**Figure 3.12** Effect of magnetic field on the stress-strain response the $Ni_{51.1}Mn_{24.0}Ga_{24.9}$ single crystals during martensite reorientation. The test temperature was -95 °C.

The resulting strain due to stress induced variant reorientation is 5.7% which is almost the same strain magnitude obtained by magnetic field induced variant reorientation under constant stress. This would be expected in the case of complete reorientation since the field and stress favors variants with short axes along their applied directions.

The stress induced reorientation in Figure 3.12 occurs with very small hardening up to 4% and then hardening increases considerably, indicating that higher stress levels are needed for further reorientation. This behavior may be correlated with the two-stage reorientation observed in the strain vs. magnetic field response under low field rates. Moreover, for stress-induced reorientation under 12 and 16 kG, at around 2.5 % strain magnitude, there is a kink which could be an indication of the activation of different twin systems.

Figure 3.13 shows the incremental strain experiment under 16 kG at -95 ºC. Loading interrupted at different strain levels in order to determine the effect of strain on unloading response and hysteresis. The reorientation between the variants is fully recoverable in all cases. It is clear that there is no significant training effect and stress-strain response follows the same loading path in each case. During unloading, the stress hysteresis is constant for strain levels up to 3% and then increases with strain magnitude. The change in hysteresis seems to be related with hardening of stress after 3-4 % which could be another indication of interacting different twin system which increases the dissipation energy, thus the stress hysteresis.

Magnetostress is defined as the difference in the stress levels with and without magnetic field at 3% strain. Figure 3.14 shows the magnetostress obtained from Figure 3.11 where other reported MFIS levels are also included for comparison [7, 13, 90, 91].

The magnetostress increases with magnetic field up to 14 kG in the present case and then saturates. The maximum magnetostress observed is 5.7 MPa. The magnetocrystalline anisotropy energy can be determined from Figure 3.10 using [91];

$$K_u = \sigma_{mag} \times \varepsilon_0 \tag{3.4}$$

where $\sigma_{mag}$ is the magnetostress and $\varepsilon_o$ is the reorientation strain. If $\varepsilon_o$ is taken as 5.8 % and $\sigma_{mag}$ as 5.7 MPa , $K_u$ is found to be 3.30 x$10^5$ J/$m^3$ which is higher than the previously determined $K_u$ values (~2.65x$10^5$ J/$m^3$) for NiMnGa [13]. The difference between the present study and previous ones stems from the high $\sigma_{mag}$ values observed here. The high magnetostress can be attributed to the high MAE due to the low operating temperature in the present study.

Another important conclusion from Figure 3.14 is that magnetostress is linearly proportional to the magnetic field up to 10 kG. An empirical linear relation can be written to determine the change in stress as a function of magnetic field for MSMAs considering the magnetocrystalline anisotropy energy, reorientation strain and saturation magnetic field, as follows:

$$\frac{\Delta\sigma_m}{\Delta H} = \frac{K_u}{(H_s * \varepsilon_0)} \tag{3.5}$$

where $\Delta\sigma_m$ is the change in stress with applied field (magnetostress), $\Delta H$ is the change in magnetic field and $H_s$ is the saturation magnetic field. It is important to note that the slope in Figure 3.14 for all reported 10M $Ni_2MnGa$ martensite responses is about the same, 0.55 MPa/kG. Additionally, the slope for the 14M martensite of NiMnGa single crystals (0.23 MPa/kG) in the figure is lower than the 14M martensite cases which can be attributed to the higher reorientation strain of the 14M martensite ($\varepsilon_0$ ~ 10%, Equation 3.5)[47]. These observations support the argument that the slope obtained in Figure 3.13 is a material property which depends on the crystallographic structure and modulation.

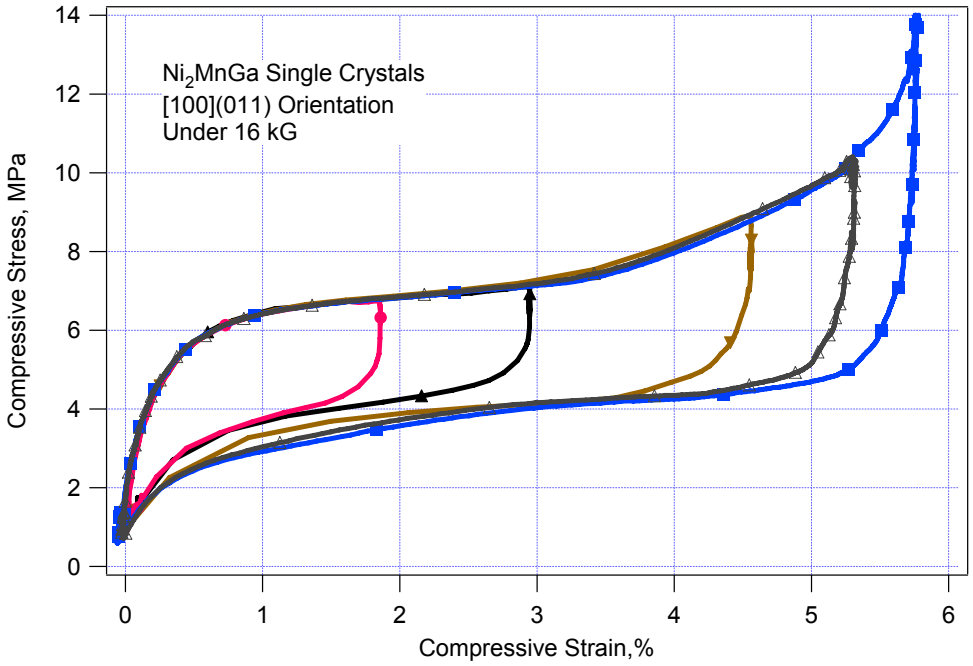


**Figure 3.13** Stress-strain response of the $Ni_{51.1}Mn_{24.0}Ga_{24.9}$ single crystals under a constant magnetic field of 16 kG at -95 °C. The loading was interrupted at selected strain levels for better understanding of strain and hysteresis evolution.

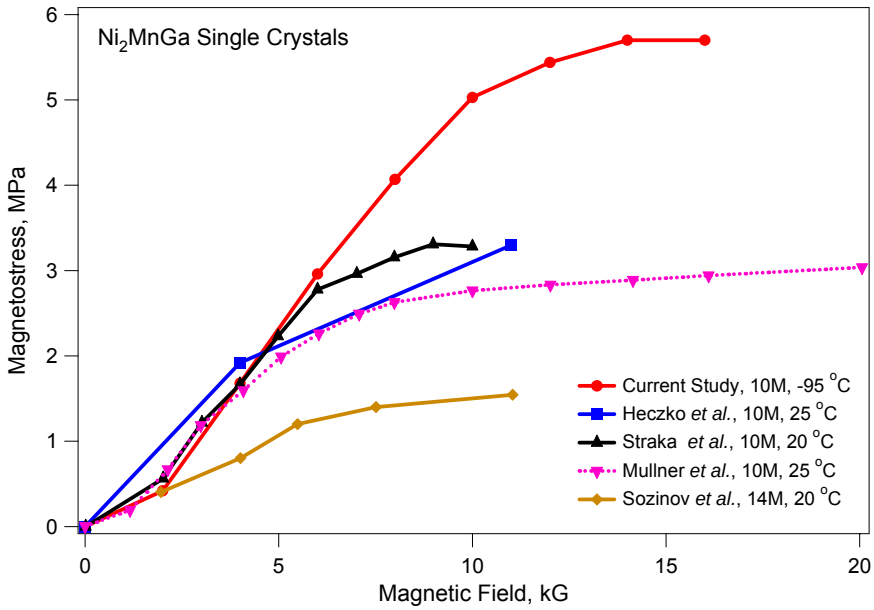


**Figure 3.14** Magnetostress as a function of applied magnetic field for NiMnGa single crystals with different martensite modulation [7, 13, 90, 91].

# CHAPTER IV
# STRESS-ASSISTED FIELD-INDUCED PHASE TRANSFORMATION IN $Ni_2MnGa$ SINGLE CRYSTALS

It is necessary to discuss some of the similarities between the field-induced and temperature-induced phase transformations to better understand the work presented herein. Figure 4.1.a shows the reversible phase transformation response in conventional SMAs under applied stress. The high temperature phase, austenite, transforms to martensite as temperature decreases and since a bias stress is applied, certain martensite variants are selected among others; resulting in an external macroscopic strain. Upon heating, martensite transforms back to austenite and strain is recovered fully in the absence of plastic deformation. The main goal of working with MSMAs is to replace the effect of temperature on phase transformation by a magnetic field, and thus, obtain the same response under stress upon field variation, which would lead to a much faster response. Under a constant stress and temperature, phase transformation can be induced by a magnetic field in $Ni_2MnGa$ single crystals, which results in a response as shown in Figure 4.1.b. As the applied field decreases, single magnetic domain austenite transforms into multi domain martensite and vice versa. This phenomenon is termed stress-assisted field-induced phase transformation and is analogous to stress-assisted thermally-induced phase transformation as shown in Figure 4.1.a.

## 4.1 Pseudoelastic Response

The stress-strain response of the $Ni_{51.1}Mn_{24.0}Ga_{24.9}$ single crystals under zero field was determined under compression along the [100] orientation as a function of temperature as shown in Figure 4.2. Two-stage martensitic transformation occurs during loading at temperatures between -70 and -40 ˚C. At these test temperature interval, the initial phase is the intermediate (I) phase as shown by the magnetization results in Chapter III. Elastic deformation of the I phase is followed by a two-stage stress-induced martensitic transformation. These martensitic phases are fully recoverable upon

unloading, leading to pseudoelasticity. A similar stress– strain response of $Ni_2MnGa$ single crystals was recently observed by Kim *et al.* [92] in which the two-stage transformation was attributed to the I phase to an unknown martensitic phase (called X-phase) to the 10M tetragonal martensite phase transformations. The I phase is thermally induced between the parent and 10M tetragonal martensite that has been reported extensively in the past [29]. The X-phase, on the other hand, is only detected under stress and shows some peculiar behavior, however, its crystallographic structure is not known at this point. At -80 ˚C, I-phase transforms to 10M martensite without transforming first to the X-phase (not shown in the figure). For temperatures higher than -40 ˚C, the first stage transformation vanishes and only one-stage transformation from I phase to 10M martensite (between -40 ˚C to -20 ˚C) and parent (P) to 10M martensite (above -20 ˚C) take place during loading. The critical stress for I-phase to X-phase transformation decreases while critical stresses for X-phase to 10M martensite or parent phase to 10M martensite increase with temperature.

**4.2 Isobaric Thermal Cycling**

Brewer [93] conducted thermal cycling experiments at stress levels ranging from 5 MPa up to 100 MPa to determine the phase transformation strain and temperature as a function of applied stress. He reported that the transformation temperature for the I-phase to 10M martensite transformation increases with increasing stress, resulting in positive Clausius-Clapeyron slope. The X-phase to I-phase transformation occurs at stress levels at or below 20 MPa, while the X-phase to martensite transformation occurs above 25 MPa. The temperatures for X-phase to I-phase transformation decrease with increasing stress level, up to about 25 MPa resulting in a negative Clausius-Clapeyron slope. On the other hand, the transformation temperatures for parent phase to X-phase and I-phase to 10M martensite increase with increasing stress levels.

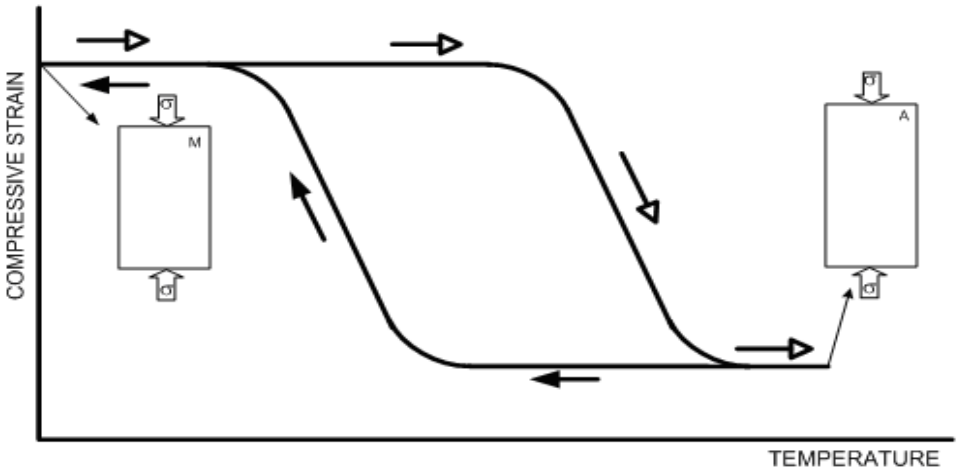


(a)

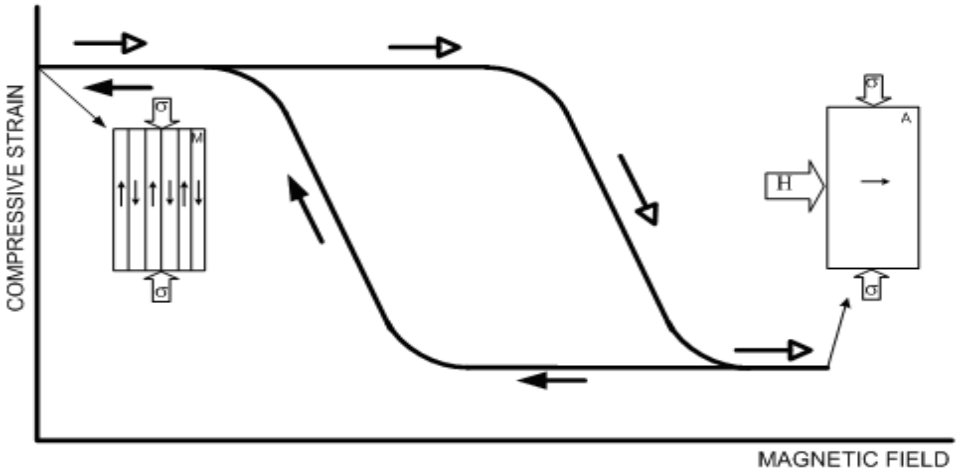


(b)

**Figure 4.1** Schematics of reversible martensitic phase transformation upon cycling (a) temperature in conventional shape memory alloys and (b) magnetic field in magnetic shape memory alloys due to field-induced phase transformation. In both cases the stress is kept constant during the phase transformation.

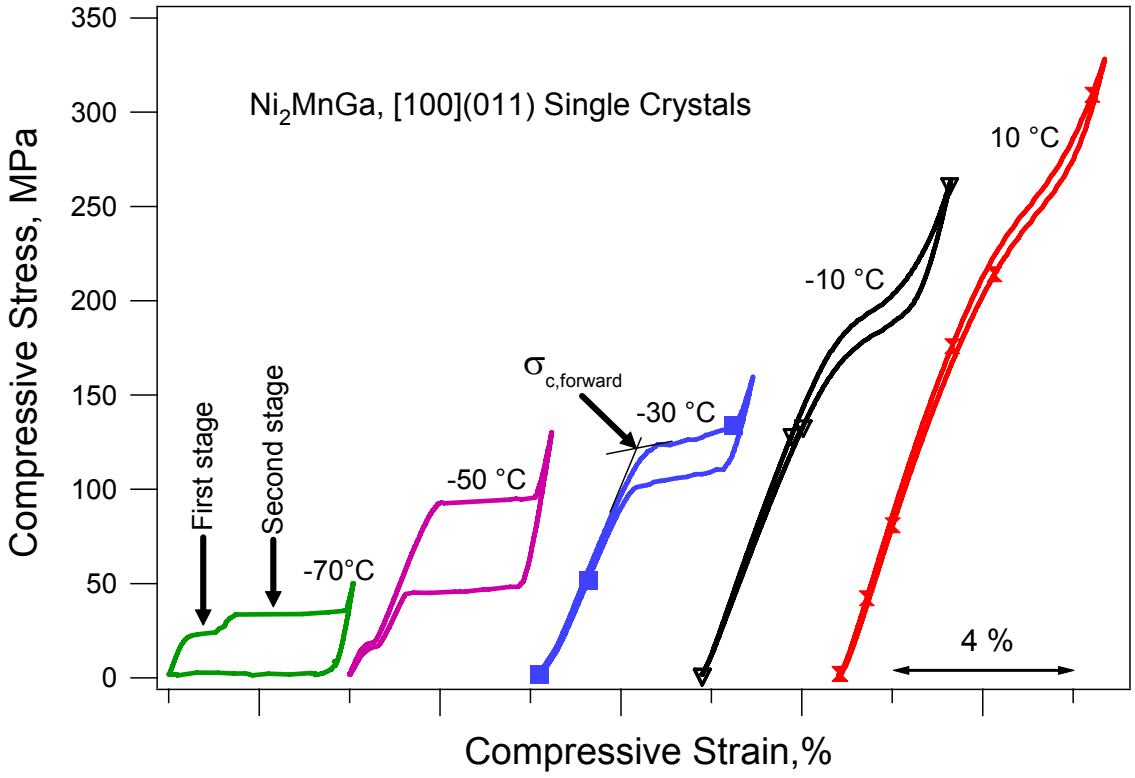


**Figure 4.2** Pseudoelastic response of $Ni_{51.1}Mn_{24.0}Ga_{24.9}$ single crystals as a function of temperature under compression along the [100] orientation. The critical stress for inducing transformation increases with temperature for the second stage while it decreases for the first stage.

Figure 4.3 details the multiple phase transformation sequence that occurs in $Ni_{51.1}Mn_{24.0}Ga_{24.9}$ under 20 MPa [93]. Upon cooling, the specimen transforms from the parent phase to the X-phase. This transformation is denoted by the steadily increasing strain as temperature decreases. The specimen then transforms from the X-phase to the I-phase. Since the I-phase is similar in structure to the parent phase, the X-phase to I-phase transformation results in a tensile strain. Therefore, as the specimen transforms to the I-phase, the strain obtained from the X-phase is diminished. Finally, upon cooling the specimen transforms from the I-phase to 10M martensite.

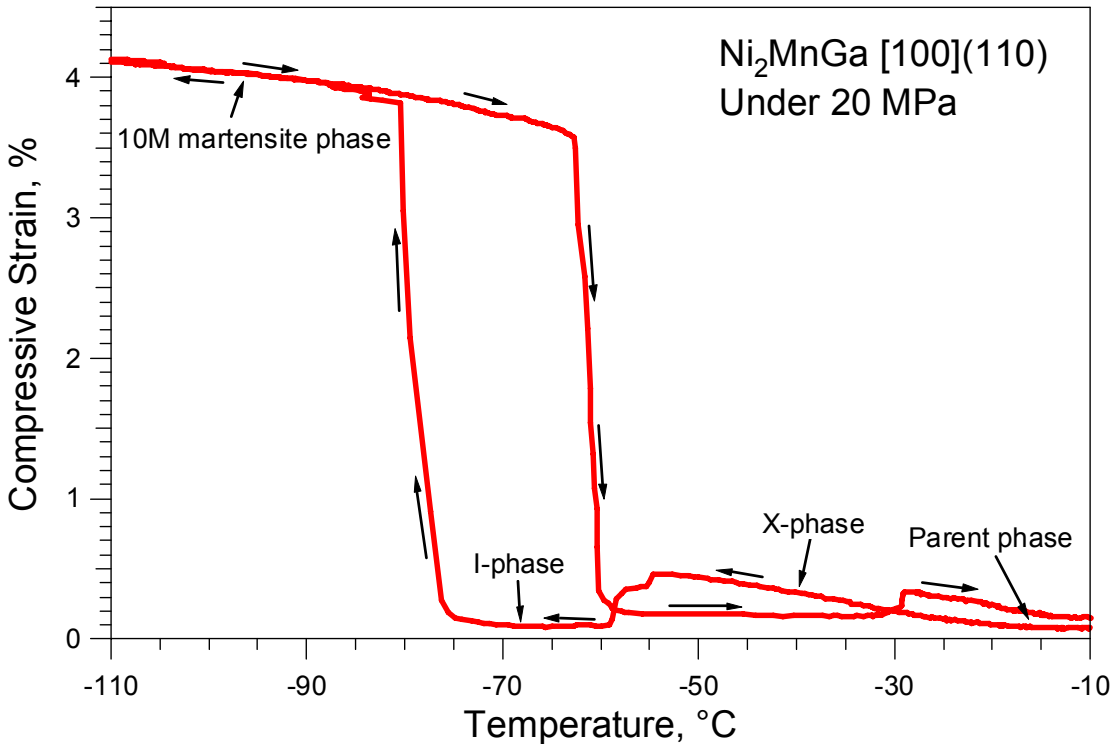


**Figure 4.3** Thermal cycling response under a compressive stress of 20 MPa illustrating the parent phase to X-phase to I-phase to 10M martensite transformation sequence in detail [93].

### 4.3 Stress-Temperature Phase Diagram

Pseudoelasticity and thermal cycling under applied constant stress experiments are used to construct the stress-temperature phase diagram for $Ni_{51.1}Mn_{24.0}Ga_{24.9}$ shown in Figure 4.4. The isobaric cooling-heating experiments are used to determine the transformation temperatures: $M_s$, X-phase start ($X_s$), and the I-phase start ($I_s$) temperatures, as a function of externally applied compressive stress and critical stresses for phase transformations are extracted from pseudoelasticity experiments shown in Figure 4.1 and added to the plot. Figure 4.4 is used to determine the Clausius-Clapeyron relationship of each phase. The solid and hallow markers show the results from the isobaric thermal cycling pseudoelasticity experiments, respectively [93].

Using Figure 4.4, it is possible to determine the stable phase for a given set of stress and temperature. The rate of increase in the critical stress level for the X-phase to 10M and parent phase to X-phase are 2.0 and 8.1 MPa/˚C while the rate of decrease in the one for the I-phase to X-phase transformation is -0.4 MPa/˚C. Kim *et al.* [92] have recently reported similar values of 2.0 MPa/˚C and -0.25 MPa/˚C for the X-phase to 10M and I-phase (or parent phase) to X-phase transformations, respectively.

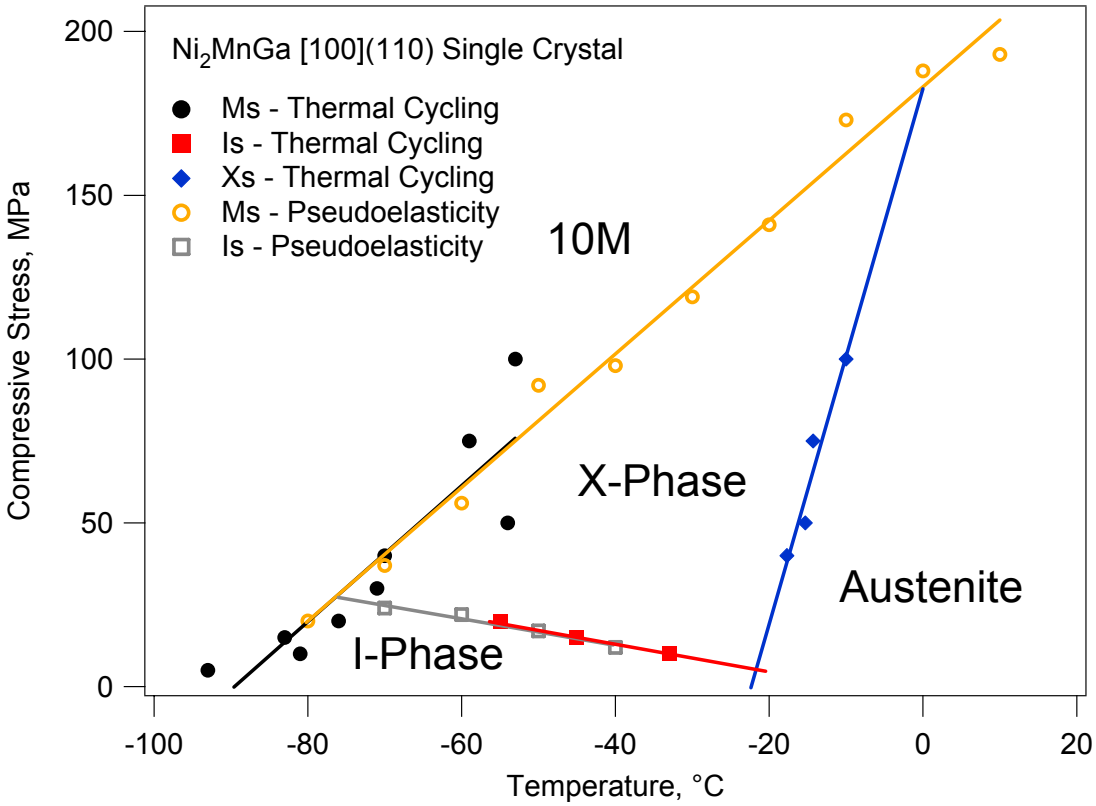


**Figure 4.4** Stress-temperature diagram for $Ni_{51.1}Mn_{24.0}Ga_{24.9}$ illustrating the multiple phase transformations [93].

The transformation sequence during stress loading at a given temperature can be determined by the stress-temperature phase diagram provided. For temperatures lower than -90 ˚C, martensite reorientation takes place in 10M martensite. I-phase transforms

directly to 10M martensite and I phase transforms to X-phase and then 10M martensite at temperatures between -90 ˚C and -70 ˚C and -70 ˚C to -20 ˚C, respectively. Austenite transforms to X-phase and then 10M martensite at temperatures between -20 ˚C and 0 ˚C, while at higher temperatures austenite transforms to 10M martensite only.

**4.4 Effect of Magnetic Field on Pseudoelasticity Response**

Figure 4.5 shows the effect of magnetic field on the pseudoelastic response at -70 ˚C. Prior to each stress cycle in the figure, the external magnetic field was applied along the [011] direction, perpendicular to the loading direction ([100] orientation) and kept constant during the loading. After each stress cycle, the field was increased incrementally in steps of 0.1 Tesla reaching up to 1.6 Tesla (16 kG) in the last cycle. For the cycles during which complete pseudoelasticity was not observed at this temperature (for example under 0, 0.2, and 0.4 Tesla fields shown in the figure), the field was increased to 1.6 Tesla after unloading to recover all residual strain and then reduced down to the field under which the next stress cycle was conducted. The critical stress levels for phase transformation in both stages increase with the magnetic field up to a certain level and then stay constant at higher fields. The inset in the figure shows the change in the critical stresses with applied magnetic field for the first and second stages.

The difference between the plateau stress levels with and without magnetic field is defined as magnetostress. The magnetostress levels for both the first and second stages are determined to be around 7 to 8 MPa at -70 °C. The critical stresses start to increase at magnetic fields above 0.2 Tesla (T). The increase for the first stage is more rapid than the second stage and it saturates at lower magnetic field magnitudes. The saturation magnetic fields for the increase in the critical stress and magnetostress are 0.7 T for the first and 1.0 T for the second stages. The difference in saturation field magnitudes should be related to the different critical magnetic field to reach saturation along the hard axis and possibly different saturation magnetization magnitudes of the product phases. It is important to note that the critical stress levels for the reverse transformation also increase almost the same amount as the forward transformation (except for the stress

cycles in which complete pseudoelasticity is not observed) indicating that the field does not notably affect the energy dissipation at this temperature.

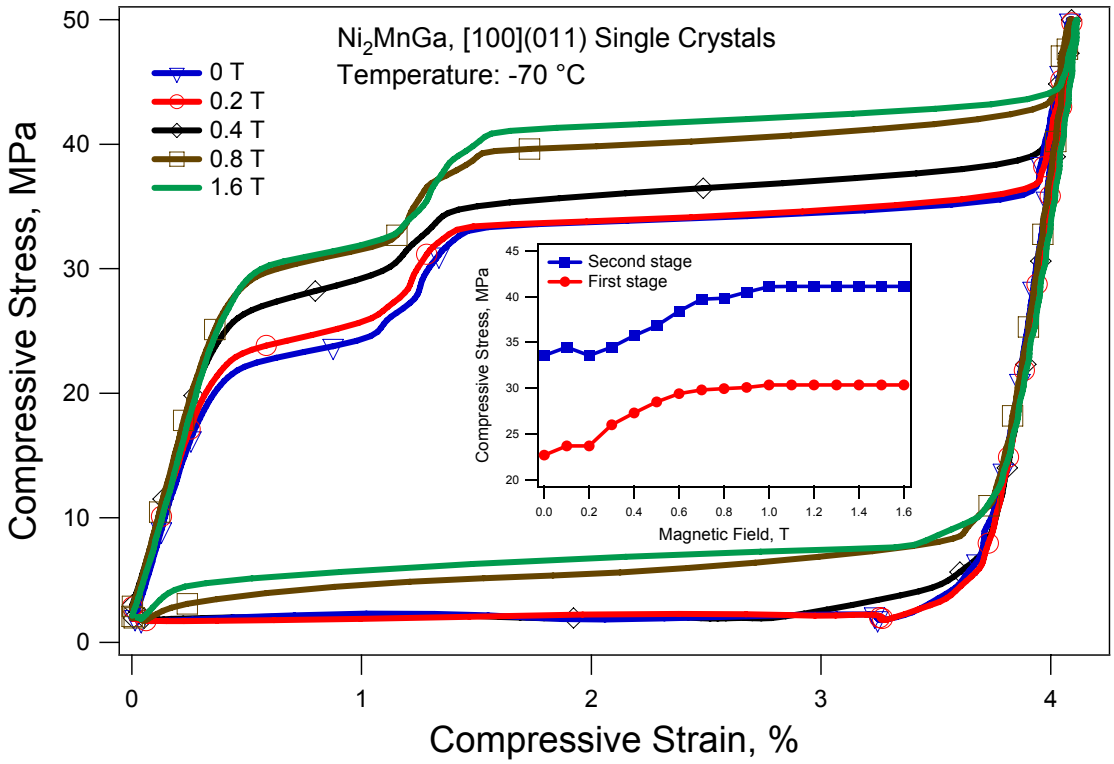


**Figure 4.5** Effect of magnetic field on the pseudoelastic response of the $Ni_{51.1}Mn_{24.0}Ga_{24.9}$ single crystals at -70 ˚C. The critical stress levels for inducing the phase transformation increase with field up to a certain level and saturate at higher fields. The inset shows the change in the critical stresses with applied magnetic field for the first and second stages.

Figure 4.6 shows the effect of temperature on the compressive stress-strain response of the single crystals under zero and 1.6 Tesla, the maximum magnetic field can be applied with the current setup. It is clear in Figure 4.6 that the magnetic field shifts the stress required to induce the phase transformation to higher levels, *i.e.* it stabilizes the initial phase (either X, I or P phases), without noticeably affecting the stress hysteresis and transformation strain. The critical stresses for forward and

backward transformations are shown by $\sigma_{c,forward}$ and $\sigma_{c,reverse}$, respectively under no magnetic field and $\sigma^{H}_{c,forward}$ and $\sigma^{H}_{c,reverse}$, respectively under magnetic field as shown on the figure. The effect of magnetic field vanishes with increasing temperature and both the magnetostress and the transformation strain decreases with increasing temperature. It is important to note that during phase transformation at low temperatures, there is a plateau region without any strain hardening that changes into a region with significant hardening with increasing temperature. This behavior can be attributed to the nucleation of single variant martensite at low temperatures and nucleation of multiple martensite variants at high temperatures. At higher temperatures the elastic mismatch between the parent and product phases increases, which could result in an increase in the stress required for phase front propagation and thus, result in the nucleation of multi martensite phase fronts. The decrease in transformation strain with increasing temperature can be attributed to incomplete transformation/detwinning process under the present applied stress levels. However further investigation is needed to clarify this phenomenon.

Figure 4.7.a shows the pseudoelastic response for both stages at -60 °C with and without magnetic field demonstrating a major difference between the responses of these two stages. If the sample is unloaded when the first stage transformation is completed, a pseudoelastic loop with very small hysteresis is observed. For both stages, the applied field shifts the pseudoelastic loops to higher stress levels. However, in the first stage, the field and the resulting magnetostress is sufficient to completely separate the pseudoelastic loops with and without magnetic field as shown in the figure. In the second stage, $\sigma_{mag}$ level is not sufficient for the complete separation of the loops due to the large stress hysteresis ($\Delta\sigma$ in the figure). Figure 4.7.b presents the effect of magnetic field on the first stage transformation as a function of temperature in more detail. It is clear that the field separates the pseudoelastic loops in a certain temperature interval*, i.e.* whenever the magnetostress is larger than the stress hysteresis.

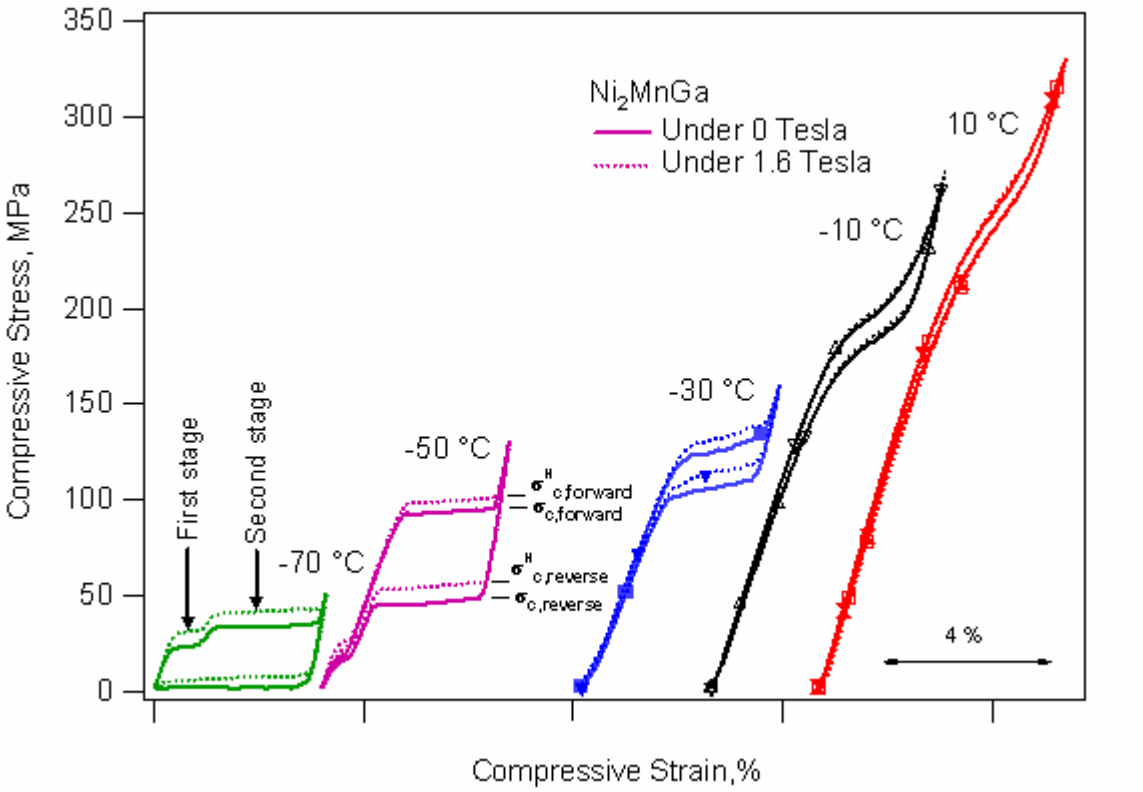


**Figure 4.6** Pseudoelastic response of $Ni_{51.1}Mn_{24.0}Ga_{24.9}$ single crystals as a function of temperature and magnetic field under compression along the [100] orientation. $\sigma_c$: Critical stress for the onset of phase transformation.

## 4.5 Magnetic Field-Induced Phase Transformation for the First Stage Transformation

The separation in pseudoelastic loops with and without magnetic field provides a unique opportunity as one can induce transformation between the phases by switching the field on and off under constant stress levels, which results in a stress-assisted reversible field-induced martensitic phase transformation. The crystal can be loaded under a magnetic field to a stress level lower than $\sigma^{H}_{c,reverse}$ but higher than $\sigma_{c,forward}$. When the magnetic field is removed, forward transformation would occur since the parent phase (the I phase in the present case) is not stable at that stress level under zero field. Using this procedure (Procedure I), the forward and reverse transformation can be

induced cyclically upon switching the field on and off in the stress range between $\sigma_{c,forward}$ and $\sigma^{H}_{c,reverse}$.

Similarly, a magnetic field-induced reverse transformation can also be induced, if the crystal is loaded under zero field to a stress level above $\sigma_{c,forward}$ allowing forward transformation to occur and the stress level is kept constant between the $\sigma^{H}_{c,reverse}$ and $\sigma_{c,forward}$. When the magnetic field is applied, the reverse transformation occurs since the martensite (the X phase in the present case) is not stable at that stress level under the field. Figure 4.8.a demonstrates an example of this procedure (Procedure II) with accompanying MFIS vs. magnetic field response (Figure 4.8.b) at -55 °C. The stress was increased up to point 1 ($>\sigma_{c,forward}$) leading to the I→X transformation and then unloaded to point 2 ($<\sigma^{H}_{c,reverse}$) under zero field. At point 2, the stress was kept constant at 22 MPa and the field was applied, which triggers the reverse transformation to the I phase at around 0.7 Tesla in the first cycle and at 0.5 Tesla in the following cycles.

Switching the field on and off continuously induces forward and reverse transformations without significant change in the field magnitudes (points 3 to 6). Thus, the field can do work against stress levels above 20 MPa. The MFIS was only about 0.5% because of the low transformation strain along the [100] orientation accompanying the I→X transformation. If the stress is reduced incrementally, the field required to trigger the forward and reverse transformations decreases. And at 18 MPa (point 7), the field can only induce reverse transformation at 0.2 Tesla because the stress level is lower than $\sigma_{c,forward}$.

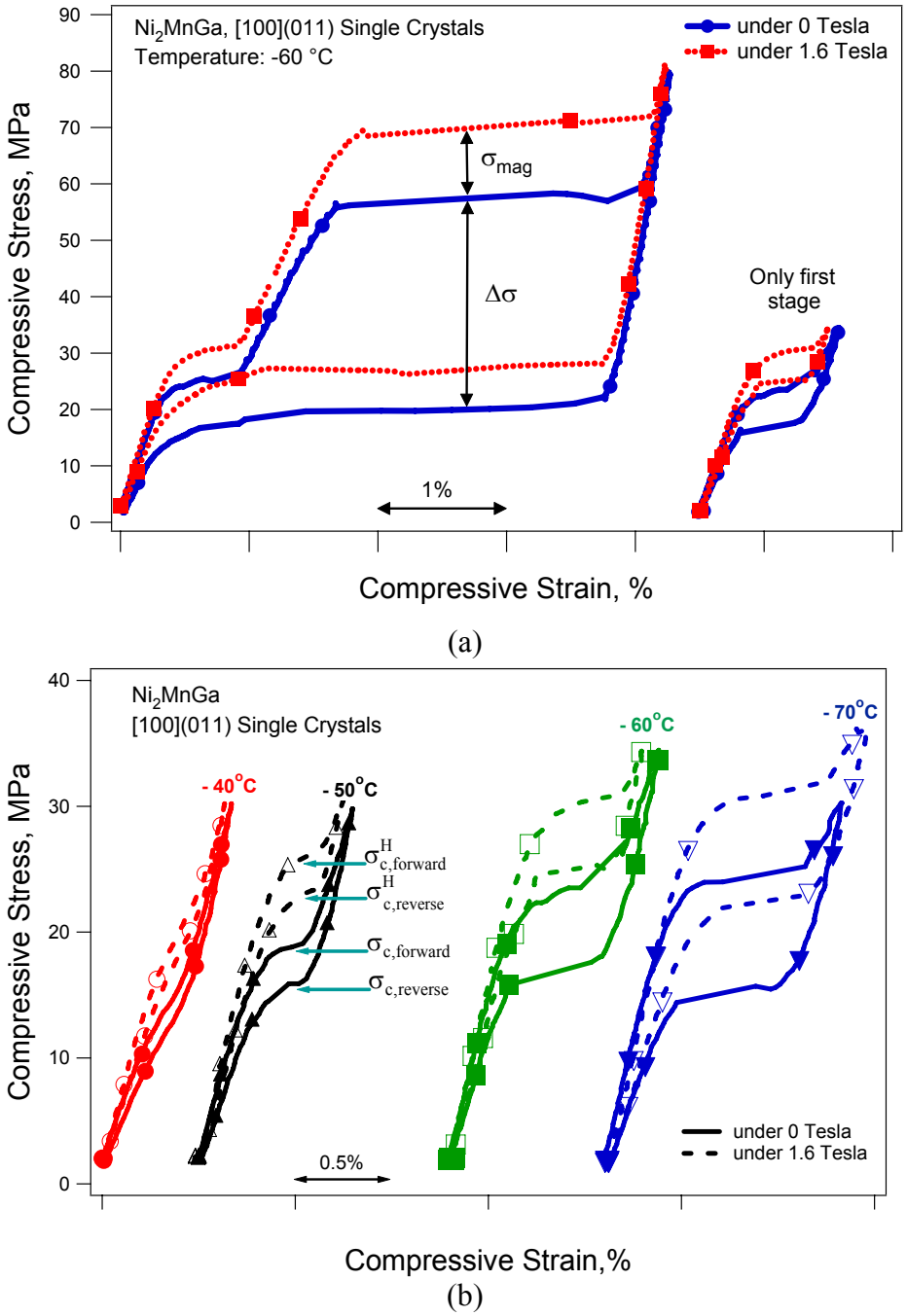


**Figure 4.7** (a) The pseudoelastic response of $Ni_{51.1}Mn_{24.0}Ga_{24.9}$ at -60 ˚C under zero (solid lines) and 1.6 T applied magnetic field (dotted lines), (b) Temperature dependence of the critical stress levels and stress hysteresis during the first stage transformation with and without magnetic field.

Figures 4.9 a and b show the stress vs. strain and strain vs. applied magnetic field response of the $Ni_{51.1}Mn_{24.0}Ga_{24.9}$ [100] single crystals at -50 ˚C, respectively. In this series of experiments, the specimen was loaded under zero magnetic field till the end of the first stage. Then, the magnetic field was cycled twice between 0 and 1.6 T at various descending stress levels and the strain response was recorded. It is clear in the figure that the MFIS and the critical magnetic fields for the onset of reverse transformation are a function of stress. For stress magnitudes higher than 22 MPa, the MFIS is low but fully recoverable without significant magnetic hysteresis. Under 20 and 22 MPa, the MFIS is as high as 0.25 % and fully reversible upon field removal. The reversible MFIS levels shown in Figure 4.9 are lower than the one shown in Figure 4.8 due to higher testing temperature where transformation strain decreases with temperature (Figure 4.7.b). Under 18 MPa, the magnetic field can induce reverse transformation with 0.3 % strain. However, only 0.12 % strain is reversible when the field is cycled. This is because of the fact that the stress level is not high enough for complete forward transformation. It is important to note that the critical magnetic fields for inducing martensite to parent phase transformation decrease with decreasing stress level. This shows that magnetic field needs to provide more energy to overcome the energy barrier to induce phase transformation at higher stress levels. Under 18, 20 and 22 MPa the critical magnetic fields for the reverse transformation are approximately 0.15, 0.23 and 0.32 Tesla, respectively. As temperature decreases, the transformation strain and the critical stress levels for the first stage transformation increase, but at the same time, the difference between $\sigma^{H}_{c,reverse}$ and $\sigma_{c,forward}$ decreases. At -70 ˚C, $\sigma_{c,forward}$ is already higher than $\sigma^{H}_{c,reverse}$ and thus, only one-way field-induced phase transformation is observed.

Reversible MFIS levels are less than 0.1% above 26 MPa in Figure 4.9.b. The small MFIS might be attributed to magnetostriction or elastic strain due to reversible martensite twin motion as observed in other NiMnGa MSMAs [18]. Although the recoverable strain magnitude is low compared to the phase transformation strain, it is still higher than the strain observed in most magnetostrictive materials [18, 94].

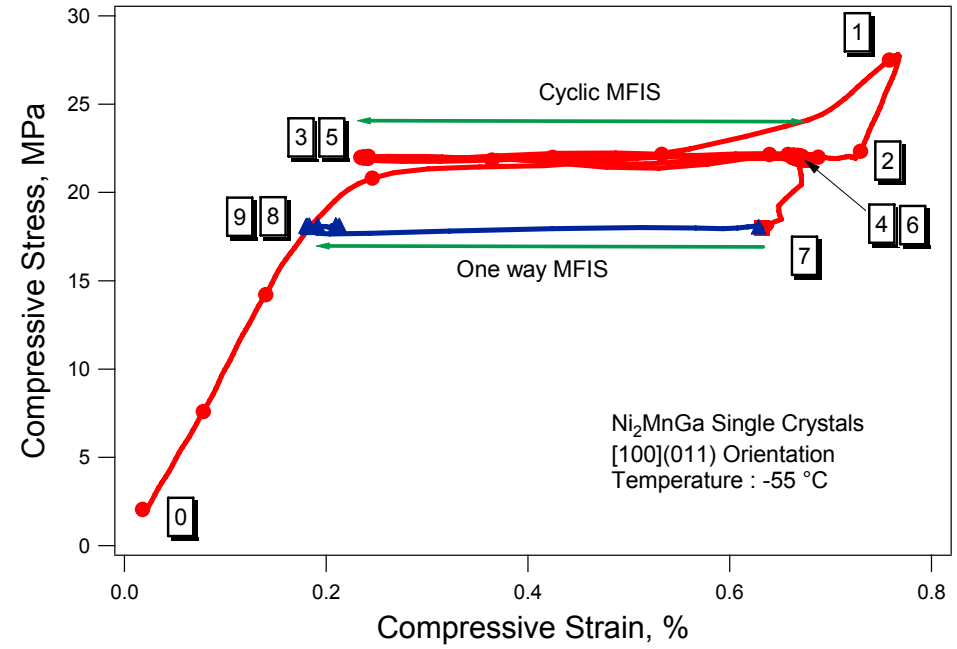


(a)

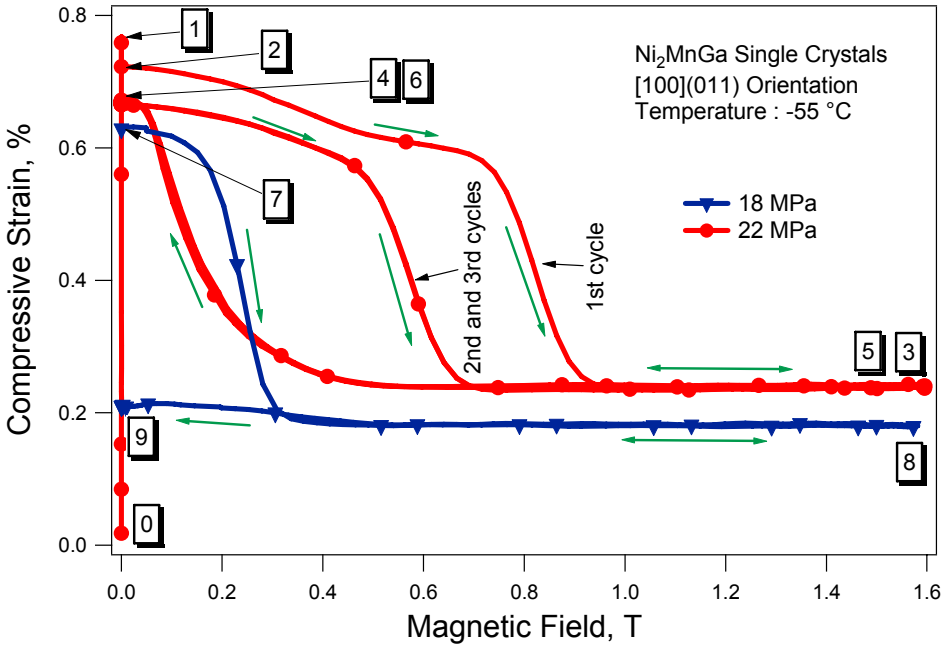


(b)

**Figure 4.8** Demonstration of the stress-assisted reversible (cyclic) field-induced phase transformation at low field magnitudes at -55 ˚C. Data in (a) and (b) are from the same experiments. The number sequence demonstrates the loading path.

## 4.6 Magnetic Field-Induced Phase Transformation for the Second Stage Transformation

Figure 4.10 shows the stress-strain-magnetic field response during the second stage transformation from the X phase to 10M martensite at -60 ˚C demonstrating the field-induced one way shape memory effect with accompanying strain vs. magnetic field response (Figure 4.10.b). The sample was loaded up to 64 MPa under 1.6 Tesla (point 1), *i.e.* below $\sigma^{H}_{c,forward}$ but above $\sigma_{c,forward}$, and then the magnetic field was removed while keeping the stress constant. The forward phase transformation took place resulting in a 2.4% strain (point 2) as the magnetic field was reduced from 0.7 to 0.5 Tesla. The reapplication of the field did not trigger reverse transformation at this stress level (point 3). After the forward transformation, the sample was unloaded to 24 MPa (point 5) under zero field, *i.e.* to a stress level between $\sigma^{H}_{c,reverse}$ and $\sigma_{c,reverse}$. Then, the magnetic field was applied resulting in 3.1 % MFIS (point 6) due to the reverse transformation at the field magnitudes between 0.1 to 0.6 Tesla. When the magnetic field was cycled between 0 to 1.6 Tesla at 24 MPa, a cyclic MFIS of 0.3% was observed due to the reversible field-induced I↔X martensitic phase transformation since the stress level is between $\sigma_{c,forward}$ and $\sigma^{H}_{c,reverse}$ for the I↔X transformation (the first stage). Unloading the sample under 1.6 Tesla completes the pseudoelastic cycle (point 9). This demonstrates that in one pseudoelastic cycle it is possible to activate both reversible and one-way field-induced phase transformation depending on the stress level.

By utilizing the field-induced phase transformation to 10M martensite, the stress at which MFIS is observed can be in the range of 30 to 140 MPa and 5 to 120 MPa for forward and reverse transformations, respectively, in the temperature range of -70 to -10 ˚C. These stress levels achieved in the second stage transformation is significantly higher than the actuation stress levels observed in the first stage transformation and field-induced martensite variant reorientation in NiMnGa MSMAs .

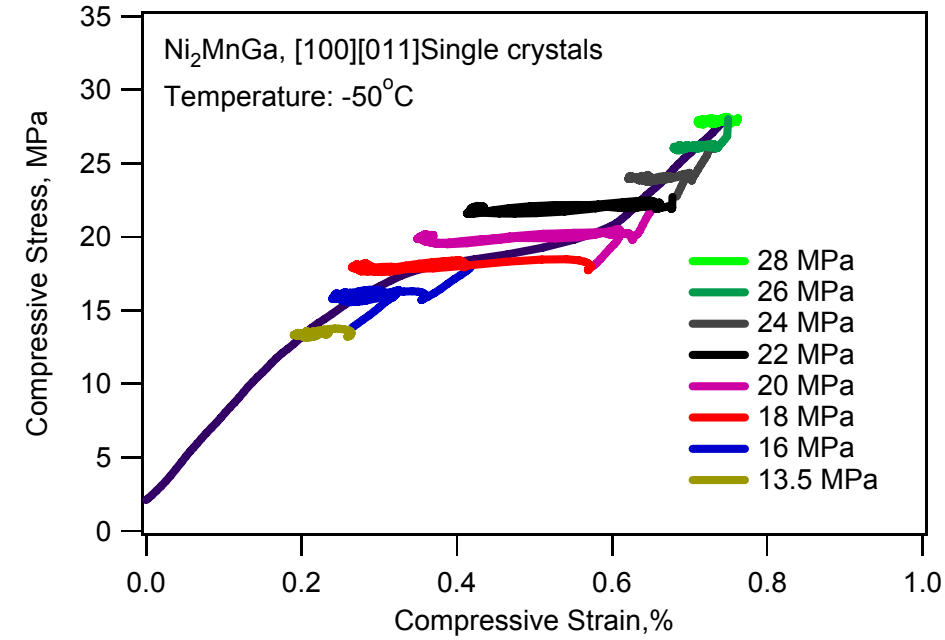


(a)

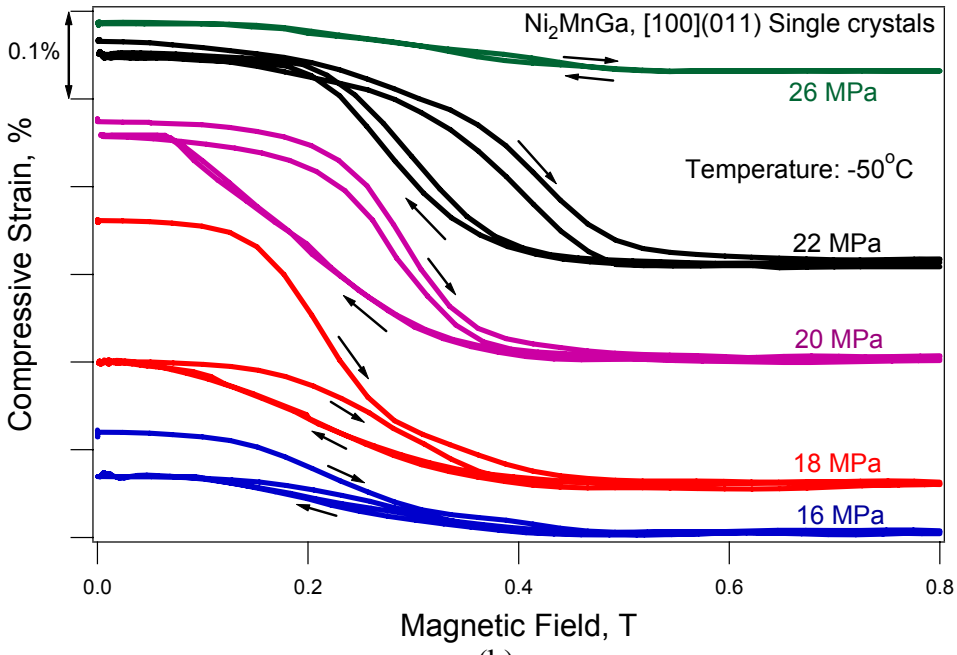


(b)

**Figure 4.9** Demonstration of the reversible (cyclic) field-induced phase transformation at low field magnitudes in $Ni_{51.1}Mn_{24.0}Ga_{24.9}$ single crystals at -50 °C, a) stress vs. strain and b) corresponding strain vs. magnetic field response.

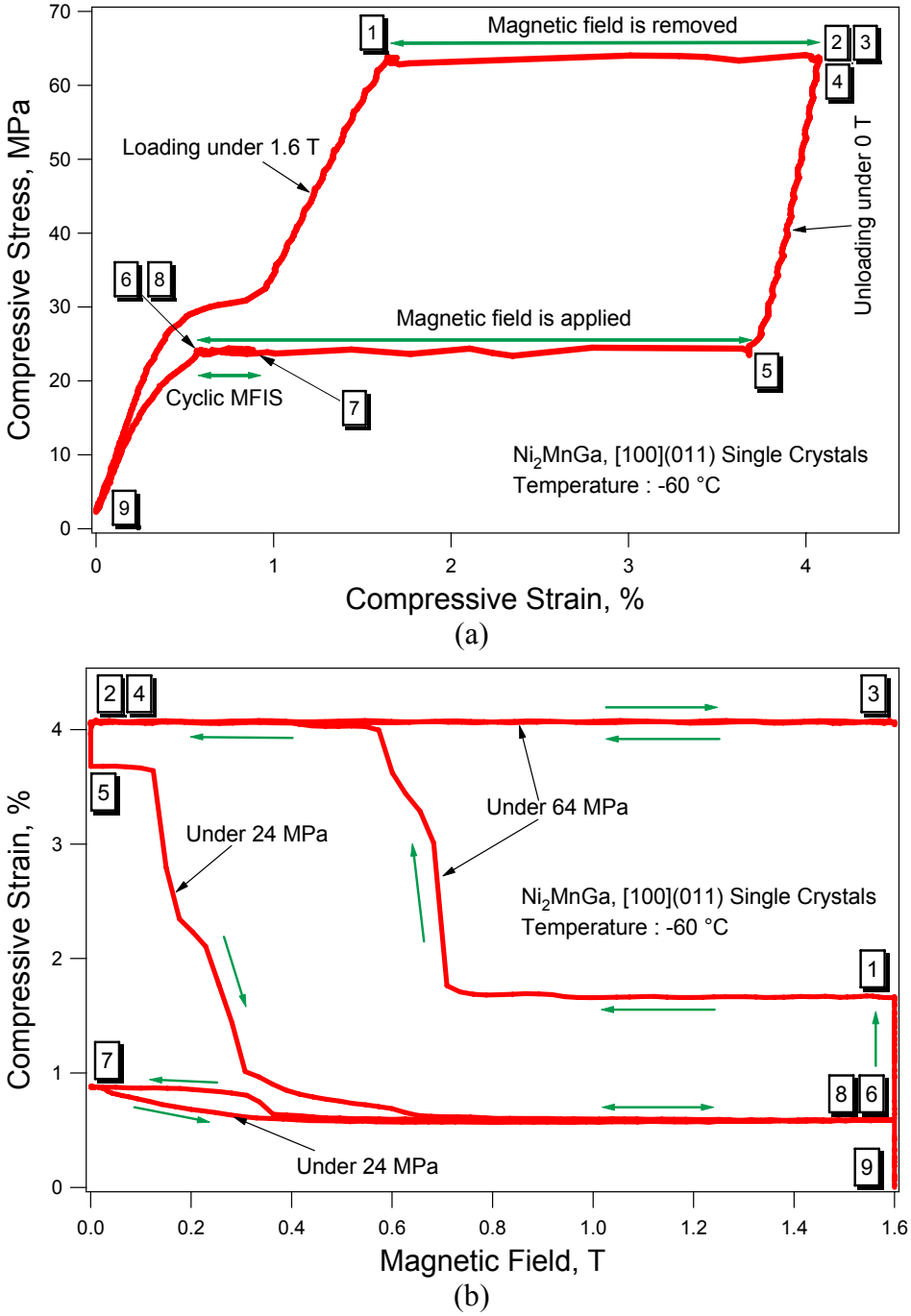


**Figure 4.10** Demonstration of the field-induced one-way shape memory effect via X to 10M martensitic transformation or vice versa at low field magnitudes. Data in (a) and (b) are from the same experiments. The number sequence demonstrates the loading path.

## 4.7 Magneto-Microstructural Mechanisms for Magnetic Field-Induced Phase Transformation

Figures 4.11.a and 11.b are schematics demonstrating a possible magneto-microstructural mechanism for reversible magnetic field-induced phase transformation under constant stress. Initially, the single crystal sample has the parent phase structure (the I phase in the present case) with magnetic domains arranged in such a way that the total magnetization is zero (not shown in the schematic). With the application of a sufficient magnetic field, magnetization direction of the domains rotates towards the applied field direction as shown by 1A in the schematic. When the compressive stress along the $[100]_{parent}$ direction is increased up to a stress level above $\sigma_{c,forward}$ but below $\sigma^{H}_{c,reverse}$, elastic deformation of the parent phase takes place with no change in magnetization direction (1B in Fig. 4.11.a). Similarly, slight decrease in the magnetic field does not change the magnetization direction (1B in Fig. 4.11.b). When the magnetic field is decreased, the parent to martensite (the X phase in the present case) phase transformation is triggered because the parent phase is not stable at that stress level under zero magnetic field. During the phase transformation, the martensite nucleates and grows (1C). Further decrease in the field magnitude leads to the formation of single variant martensite (1D). Removing the magnetic field completely after the transformation, results in multi magnetic domains with magnetization direction along the easy axis (compression direction) to minimize the total magnetization (1D').

After the transformation is completed, reapplication of the magnetic field triggers the martensite to parent phase reverse transformation (Figure 4.11.b). Under the constant stress level, applying field perpendicular to the compression direction causes the rotation of the magnetization direction of martensite towards the field direction. As the field magnitude increases, the rotation angle of the magnetization away from the easy axis increases, so does the stored MAE (1E). When the MAE reaches a critical magnitude the martensite to parent phase transformation takes place instead of further rotation of magnetization (1F), *i.e.* the parent phase with magnetization direction along the field nucleates and grows.

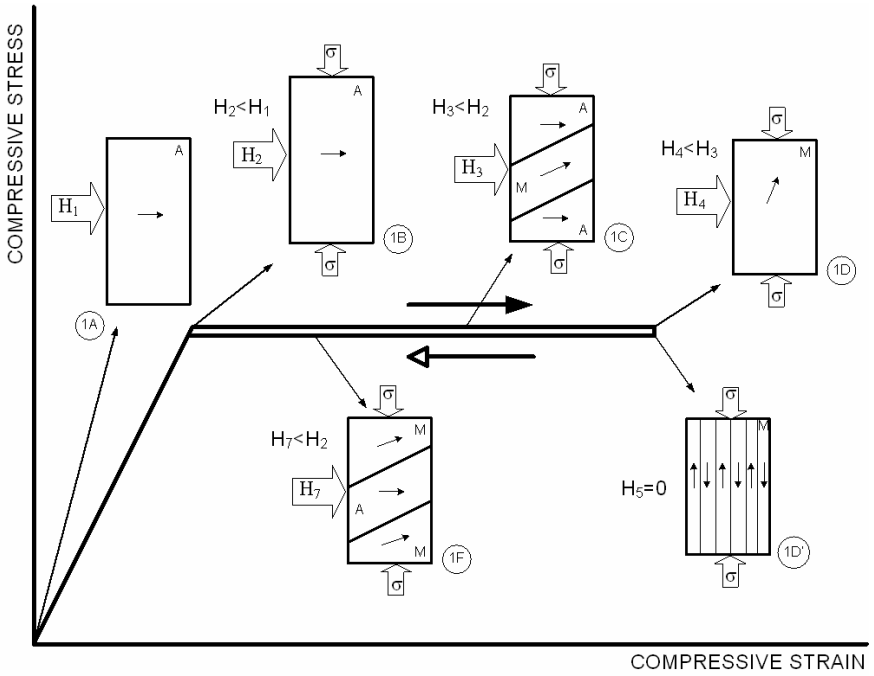


(a)

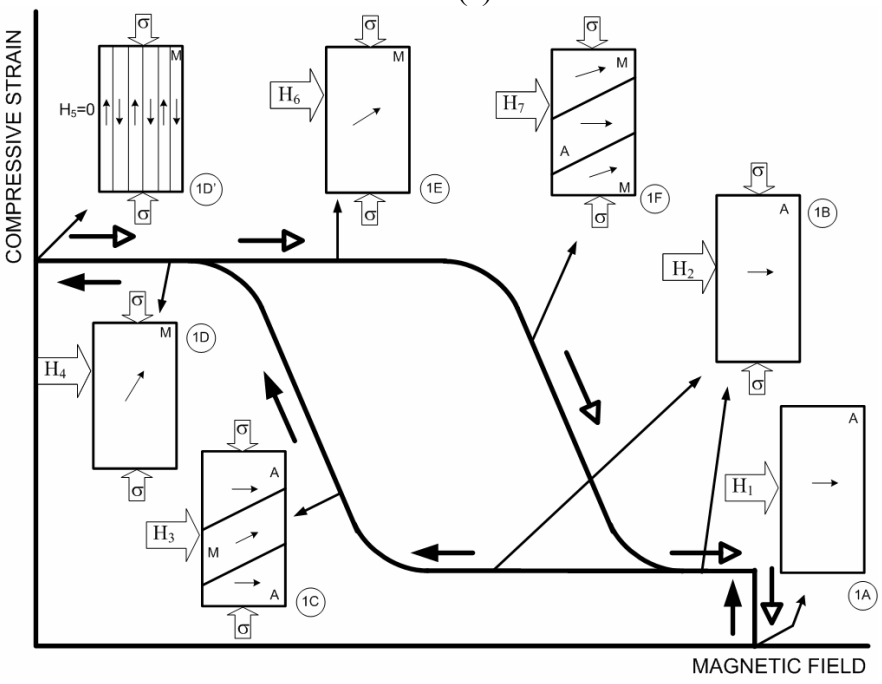


(b)

**Figure 4.11** Schematics of the reversible magnetic field-induced phase transformation under a constant stress level. (a) Stress vs. strain and (b) corresponding strain vs. magnetic field response.

It is important to note that the lower MAE of the parent phase in $Ni_2MnGa$ results in the rotation of the magnetization at lower magnetic field magnitudes than that for the magnetization rotation in martensite. In this mechanism, the evolution of magnetic domains is considered in an average sense, however, the real material behavior could be more complicated than what is presented here, especially if the specimen shape and size, and demagnetization energy are considered.

Figure 4.12 is a schematic demonstrating a possible magneto-microstructural mechanism for one-way magnetic field-induced phase transformation under constant stress levels similar to the experiment shown in Figure 4.10. Initially, the single crystal sample is in the parent phase with magnetic domains arranged in such a way that the total magnetization is zero (not shown in the schematic). With the application of a sufficient magnetic field, magnetization direction of the domains rotates towards the applied field direction as shown by 1A in the schematic. When the compressive stress along the $[100]_{parent}$ direction is increased up to $\sigma_1$, above $\sigma_{c,forward}$ but below $\sigma^H_{c,forward}$, the elastic deformation of the parent phase takes place with no change in magnetization direction as shown by 1B. When the magnetic field is removed under constant stress $\sigma_1$, parent to martensite phase transformation is triggered because the parent phase is not stable at that stress level under zero magnetic field. During the phase transformation, martensite nucleates and grows as shown by 1C. Further decrease in the field magnitudes leads to the formation of single variant martensite as shown by 1D. The magnetization direction of the martensite should be along the compression direction under zero magnetic field since the easy axis of martensite is along that direction. Removing the magnetic field completely after transformation will result in multi magnetic domains with magnetization direction along the easy axis to minimize the magnetization as shown by 1D' in the schematic. After the parent to martensite phase transformation, the reapplication of the field will not result in martensite to austenite phase transformation since $\sigma^H_{c,reverse} < \sigma^H_{c,forward}$. If not, then the stress needs to be unloaded under zero field as in the case of Figure 4. Unloading the stress to $\sigma_2$ ($\sigma^H_{c,reverse}$

$> \sigma_2 > \sigma_{c,reverse}$) will only result in elastic strain without any change in domain structure (1E). At this stress level, applying field perpendicular to the compression direction causes the rotation of the magnetization direction of martensite towards the field direction. As the field magnitude increases, the rotation angle of the magnetization away from the easy axis increases, so does the stored MAE. When the MAE reaches to a critical magnitude, i.e. to the critical energy needed for reverse transformation, martensite to parent phase transformation starts to take place instead of further rotation of the magnetization. The parent phase with magnetization direction along the field nucleates and grows as shown by 1F. It is important to note that the lower MAE of the parent phase results in the rotation of the magnetization at lower magnetic field magnitudes than that for the magnetization rotation in martensite. When the field is increased above a critical value, the reverse transformation is completed and unloading under the field completes the pseudoelastic cycle, shown as 1A.

### 4.8 Mechanical Conditions for Reversible and One-Way Field-Induced Phase Transformation

Figure 4.13.a shows the critical stress levels for phase transformations with and without magnetic field for the first stage phase transformation as a function of temperature. Note that in Figure 4.13 the compressive stresses are shown as positive stresses. In the figure, the stress range between $\sigma_{c,forward}$ and $\sigma^{H}_{c,reverse}$ forms the area in which the reversible field-induced phase transformation can be observed provided that $\sigma^{H}_{c,reverse} > \sigma_{c,forward}$. The stress range for which reversible strain is obtained decreases with decreasing temperature due to the increasing stress hysteresis and nearly constant magnetostress. Above -40 °C, the first stage transformation ceases. As temperature increases, $\sigma^{H}_{c,reverse}$ exceeds $\sigma^{H}_{c,forward}$ because of strain hardening at higher temperatures.

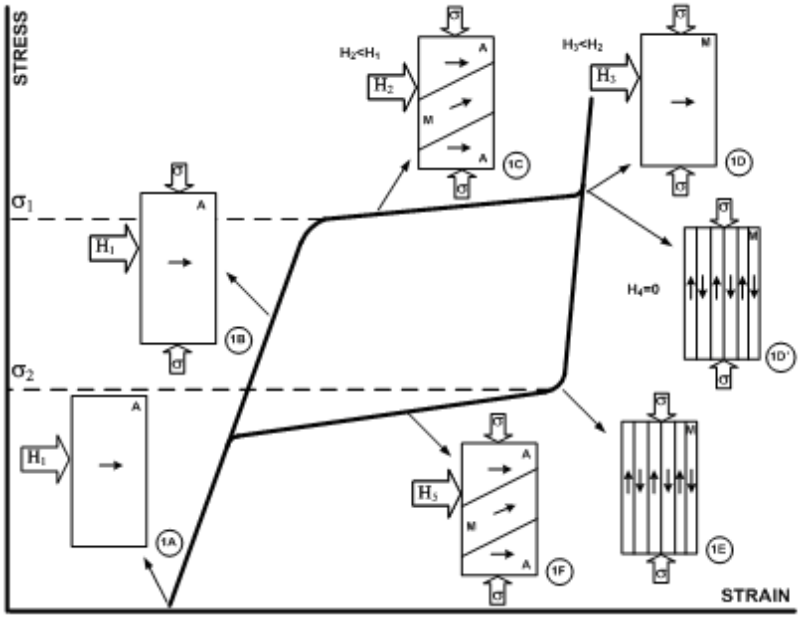


(a)

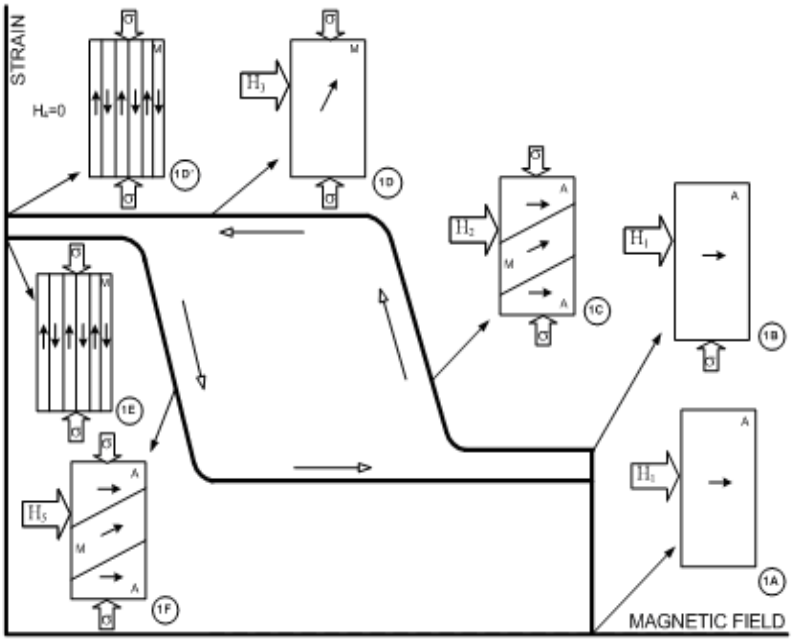


(b)

**Figure 4.12** Schematic of the magnetic field-induced forward and reverse phase transformation under different constant stress levels. (a) stress vs. strain and (b) corresponding strain vs. magnetic field response.

There is no stress or temperature range in which reversible field-induced phase transformation was observed for the second stage phase transformation. Figure 4.13.b shows the stress hysteresis and magnetostress levels as a function of temperature for this stage extracted from experiments similar to the ones shown in Figure 4.7. Stress hysteresis and magnetostress were determined at 50 % of the transformation strain. One-way field-induced phase transformation can occur at temperatures where magnetostress is not zero. The reason for the lack of reversible field-induced phase transformation in this stage is the stress hysteresis being larger than the magnetostress. Even though the stress hysteresis decreases from 32 MPa to 11 MPa by increasing temperature from -70 ˚C to 10 ˚C, the magnetostress also changes with temperature and the variation in stress hysteresis and magnetostress with temperature is not uniform. The figure can be divided into three regions depending on the initial phase, *i.e*. X→10M, I→10M and P→10M phase transformation regions. The first region is between -70 ˚C and -50 ˚C where the stress hysteresis increases while the magnetostress decreases with temperature. The second region is between -50 ˚C and -20 ˚C where stress hysteresis decreases considerably with temperature while magnetostress is constant. The last one is above -20 ˚C where the stress hysteresis is almost constant while magnetostress decreases with temperature and vanishes above 10 ˚C.

The possible reasons for the change in magnetostress with the type of parent phase and temperature will be discussed in the following sections. The same dependence for stress hysteresis can be attributed to different lattice incompatibilities between 10M martensite and X, I and P phases. From Figure 4.13.b, it can be concluded that the X and 10M phases are less compatible while the P and 10M phases are quite compatible. Lattice compatibility also changes with stress due to the difference between the changes in lattice parameters of transforming phases under stress. Since the stress level for the onset of transformation changes with temperature, this indirectly leads to the different temperature dependence of the lattice parameters of the transforming phases, and thus, brings about the temperature dependence of compatibility and stress hysteresis.

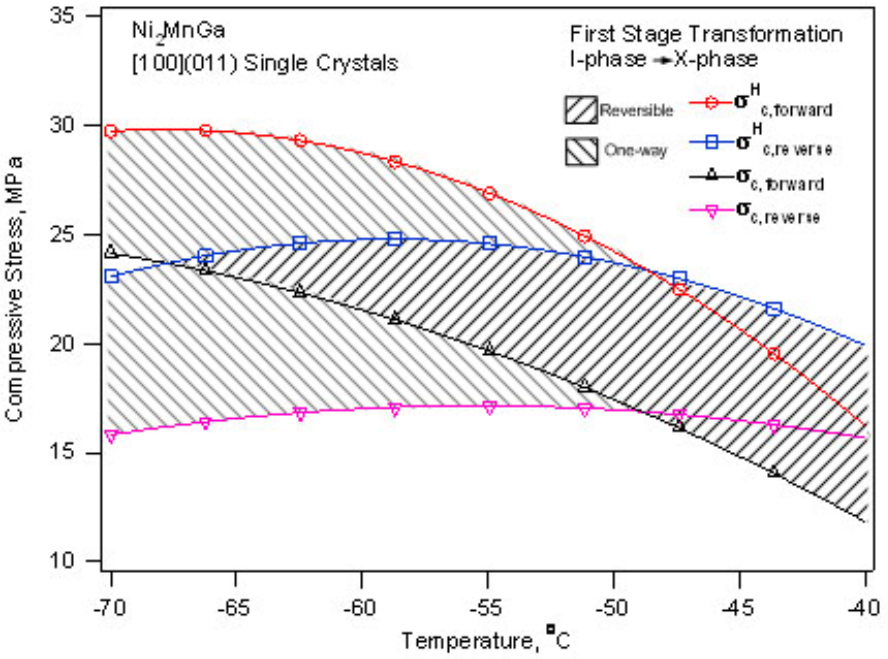


(a)

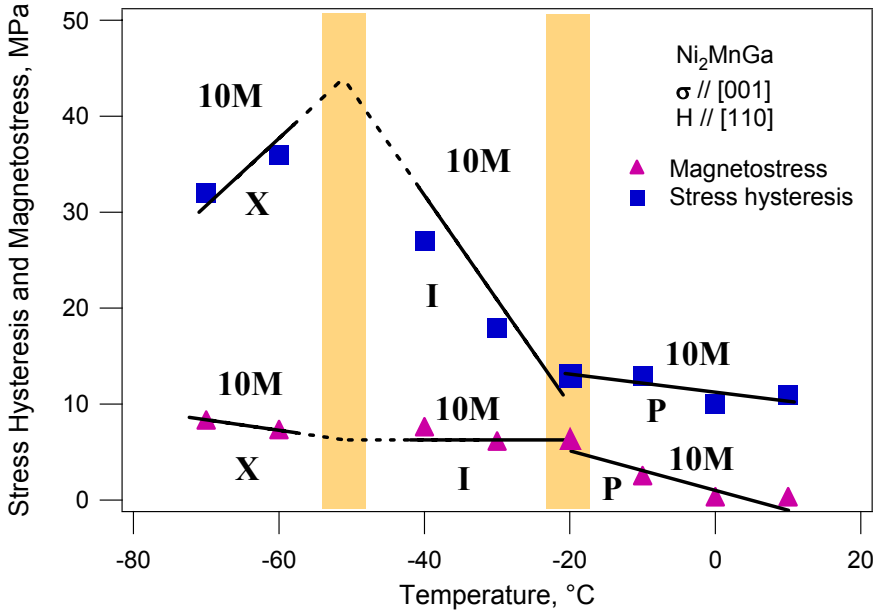


(b)

**Figure 4.13** (a) Actuation stress ranges for the reversible and one-way field-induced phase transformations in between I-phase and X-phase as a function of temperature. (b) Stress hysteresis and magnetostress in the second stage phase transformation as a function of temperature. The figure is divided into three regions depending on the type of the parent phase as X→10M, I→10M and P→10M phase transformation regions.

The following mechanical conditions need to be fulfilled for the realization of one-way and reversible field-induced phase transformations in the pseudoelastic temperature regime:

One-way field-induced phase transformation:

$$\sigma^{H}_{c,forward} - \sigma_{c,forward} \neq 0 \text{ and/or } \sigma^{H}_{c,reverse} - \sigma_{c,reverse} \neq 0 \quad (4.1)$$

Reversible field-induced phase transformation:

$$\sigma^{H}_{c,reverse} - \sigma_{c,forward} > 0 \text{ or } \sigma_{c,reverse} - \sigma^{H}_{c,forward} > 0 \quad (4.2)$$

These equations are valid if the applied magnetic field changes the critical stresses for transformation. If the applied magnetic field decreases the critical stresses, *i.e.* $\sigma^{H}_{c,forward} - \sigma_{c,forward} < 0$, then the field application would result in martensite to parent phase transformation in suitable stress ranges. On the other hand, if the field increases the critical stresses (*i.e.* $\sigma^{H}_{c,forward} - \sigma_{c,forward} > 0$), then the field application would result in parent to martensite phase transformation.

### 4.9 Effect of MAE on Phase Transformations in NiMnGa Alloys

In order to clearly capture the effect MAE on the superelastic response, two different paths to induce austenite to single variant martensite phase transformation are shown by the two schematics in Figure 4.14. In the first case, the magnetic field is applied prior to the stress loading while in the second case, field is applied after stress induced phase transformation. In both cases, the initial phase is austenite with multi domains where the magnetization direction in the domains is along the easy axis of austenite as shown by 1A and 2A. If a magnetic field higher than the critical one for magnetization saturation is applied, perpendicular to the compression axis, domain wall motion and magnetization rotation will result in single magnetic domain of austenite where the magnetization direction is along the field direction. With the application of compressive stress, martensite variant nucleates and propagates as shown by 1C. When martensite variant forms the magnetization direction will be along the applied field

direction since applied magnetic field is higher than the saturation magnetic field of hard axis. Further loading will result in single variant of martensite with magnetization direction parallel to the field direction.

In the second case, the sample will be loaded to induce phase transformation without magnetic field. As shown by 2B, the stress induced martensite will have multi magnetic domains with their magnetization direction along the compressive direction which is also their easy axis of magnetization. The critical stress for phase transformation under zero field will e lass than the on under magnetic field as shown in Figure 4.5. Further loading will result in single variant of martensite with multi magnetic domains as shown by 2C. Application of high magnetic field upon transformation will result in single magnetic domain of martensite with magnetization direction parallel to the field direction where the stress levels in 1D and 2D are same and they are greater than the stress level at 2C, $\sigma_1 = \sigma_3 > \sigma_2$ .

The total energies of the first and second cases are the mechanical energy plus the MAE of austenite and the mechanical energy plus the MAE of martensite, respectively. We can conclude that the increase in critical stresses is due to the difference between MAE of austenite and martensite, $\Delta G_{MAE}$, which can be represented as;

$$\Delta G_{MAE} = \left(K_u \sin\theta\right)_{martensite} - \left(K_u \sin\theta\right)_{parent} \quad (4.3)$$

where $K_u$ represents maximum MAE and $\theta$ is the angle between the applied field direction and easy axis of magnetization of each phase. The schematic in Figure 4.14 presents the fact that the increase of critical stresses under magnetic field is due to the MAE of martensite in cases where the MAE of austenite and the difference between saturation magnetization of phases are both negligible.

The controversy in the results reported in the literature whether applied magnetic field results in martensite or austenite stabilization could be explained now [57, 58]. First of all, it is important to note that martensite is ferromagnetic where austenite is paramagnetic or ferromagnetic depending on the composition and it is important whether single crystals or polycrystals are used in the aforementioned studies [57, 58].

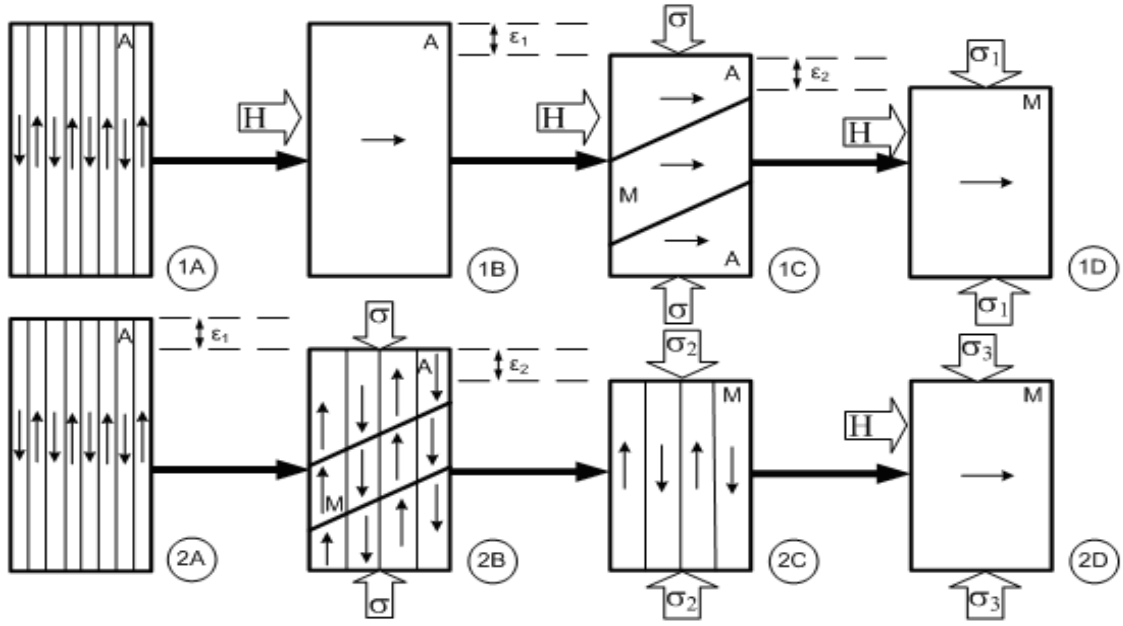


**Figure 4.14** Two schematics showing two different paths to induce austenite to single variant and magnetic domain martensite phase transformation. (a) Magnetic field is applied prior to the stress loading, (b) magnetic field is applied after the stress induced phase transformation.

The increase in TTs with magnetic field is reported when paramagnetic austenite transforms to ferromagnetic martensite [52]. On the other hand, Kim et al. [95] reported that on a single crystal of NiMnGa with both ferromagnetic martensite and austenite, TTs decrease a few Kelvin's with magnetic field under stress resulting in higher critical stress for phase transformation under magnetic field, which is also consistent with the results presented herein.

The schematic in Figure 4.15 will be used to explain the effect of applied magnetic field on phase transformation in NiMnGa polycrystals depending on whether austenite is ferromagnetic (Figure 4.15.a) or paramagnetic (Figure 4.15.b). In the schematic, the area shown as M represents the total volume of the martensite phases in all grains. It is also assumed that the magnetization direction on each martensite grain is along its easy axis due to the high MAE of martensite. Total magnetization direction per unit volume of martensite, shown as $M^m$, is along some arbitrary direction in the

schematic since the direction of the short axis of martensite depends on the individual grain orientation of grains. $M^m_x$ and $M^m_y$ represent the horizontal and vertical components of $M^{m,}$ respectively. The magnetization direction per unit volume of austenite, shown as $M^a$, is along the applied magnetic field direction due to its low MAE. When magnetic field magnitude is increased, the $M^m_y$ is magnetically unfavorable where $M^m_x$ and $M^a$ are favorable. If MAE is large, meaning that the energy for the rotation of the $M^m_y$ component towards the $M^m_x$ direction is large, and $M^a$ is larger than $M^m_x$, phase transformation from martensite to austenite will occur favoring the increase of total magnetization along the applied magnetic field.

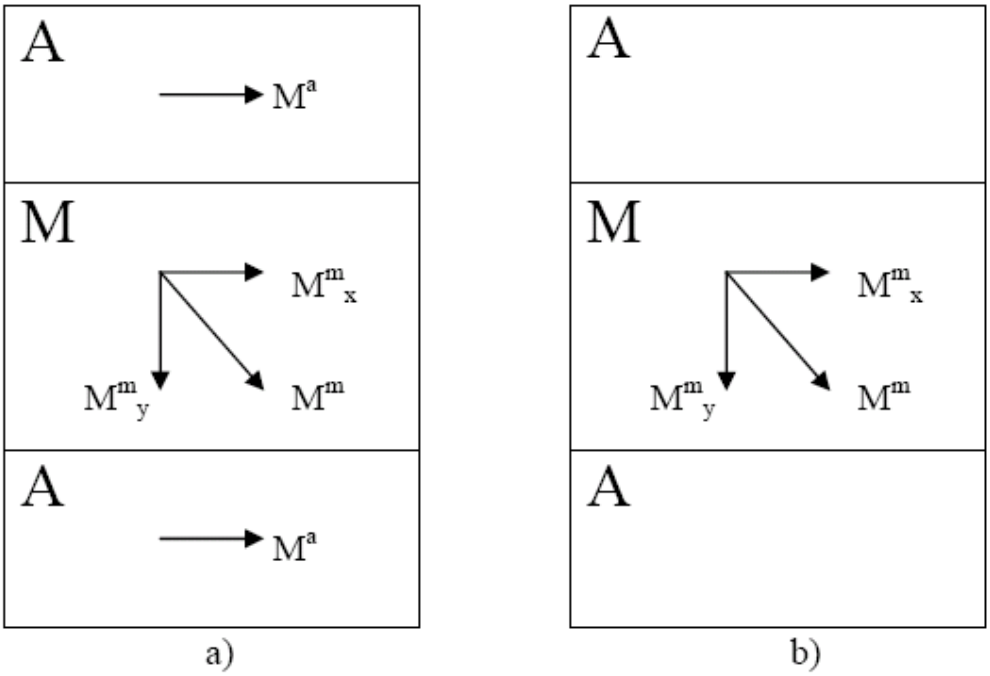


**Figure 4.15** A schematic to explain effect of magnetic field on the phase transformation of MSMA polycrystals with a) ferromagnetic and b) paramagnetic austenite phase.

If austenite is paramagnetic, magnetization of austenite can be neglected with respect to magnetization of martensite. When magnetic field magnitude is increased, $M^m_x$ component of martensite is the only favorable magnetization component. Since magnetization of austenite is neglected, applied magnetic field will result in phase transformation from austenite to martensite to increase the total magnetization along the applied magnetic field. It is also important to note that, in the second case the phase transformation doesn't depend on the MAE magnitude. The field induced austenite stabilization reported by Murray *et al.* [57] and martensite stabilization reported by Jeong *et al.* [58] on NiMnGa polycrystals under applied stress can be explained by the schematics used above where the austenite was ferromagnetic in the former case and paramagnetic in the latter one as shown by the two schematics in Figure 4.15.

Effect of magnetic field perpendicular to the compressive stress in a single crystal with ferromagnetic martensite is shown in Figure 4.14 and on polycrystals is shown in Figure 4.15. Based on those observations, a schematic in Figure 4.16 will be used to demonstrate the effect of magnetic field on a single crystal in three different configurations based on whether austenite is paramagnetic or ferromagnetic and the field is applied parallel or perpendicular to compression axis. Figure 4.16.a corresponds to a case where austenite is ferromagnetic and the field is parallel to the compression direction. In Figure 4.16.b, austenite is paramagnetic and the field is perpendicular to the compression axis, and in Figure 4.16.c, austenite is paramagnetic and the field is applied parallel to the compression axis. In all cases, the product phase, i.e. martensite, is obtained by using two different paths: the field applied first and then loading or vice versa, as in the case shown in Figure 4.14.

In Figure 4.16.a, when magnetic field is applied the domains in austenite will align themselves along the magnetic field by only domain wall motion shown as 3B. When the sample is loaded, a single variant of martensite will form with easy axis along the compression axis which is also the field direction, 3C. Further loading will result in transformation of austenite to martensite without any magnetization rotation, 3D. If we apply stress first, martensite will form with multi domains as shown by 4B and in the

end austenite will completely transform into martensite with multi magnetic domains where their magnetization direction is along the compressive direction, 4C. When magnetic field is applied domain wall motion will take place and a single magnetic domain of single variant martensite will form as shown by 4D. In this two case magnetic field plays a role during domain wall motion of both martensite, 4D, and austenite, 3B, and during the formation of martensite under magnetic, 3C. The energy required for domain wall motion is usually very small with respect to the anisotropy energy and mechanical energy and it will be neglected in this discussion. Also the effect of magnetic field during transformation can be neglected if saturation magnetization of martensite and austenite is close, which is the case when both phases are ferromagnetic. Overall there will be no effect of magnetic field in energy terms and corresponding critical stress terms.

The case shown by Figure 4.16.b is similar to the case shown in Figure 4.16.a, but in this case austenite is paramagnetic. In paramagnetic austenite there will be no magnetic domains as in the ferromagnetic case. The transformation in both paths will be same as explained in the previous case. However, in this case magnetic field will favor the formation of martensite, 5C, since the saturation magnetization of martensite is much higher than austenite. The energy term that originates from the difference between the saturation magnetizations of austenite and martensite is called Zeeman energy difference and expressed as [15];

$$\Delta G_{mag}^{P\rightarrow M} = H.M_{martensite}^{s} - H.M_{parent}^{s} \tag{4.4}$$

The critical stress for austenite to martensite phase transformation will decrease since magnetic field favors martensite in this case.

The case shown by Figure 4.16.c is similar to the previous case but this time the field is applied perpendicular to the compressive axis. Application of magnetic field prior to loading will have no effect in austenite as shown by 7B. However, when martensite forms its magnetization direction will form along the applied field direction due to high magnetic field, 7C. Additionally since austenite is paramagnetic, magnetic field will favor the transformation from paramagnetic austenite to ferromagnetic

martensite and a single variant and single magnetic domain of martensite will be obtained after complete transformation. The second path of the case is same as in the previous case prior to the application of magnetic field. When magnetic field applied, 8D, magnetization rotation and domain wall motion will take place and the final configuration will be a single variant and single magnetic domain of martensite. In this case, two energy terms, MAE and the Zeeman energy difference, will act in opposite ways. MAE favors austenite and results an increase in critical stresses while Zeeman energy favors martensite and results in decrease in critical stresses.

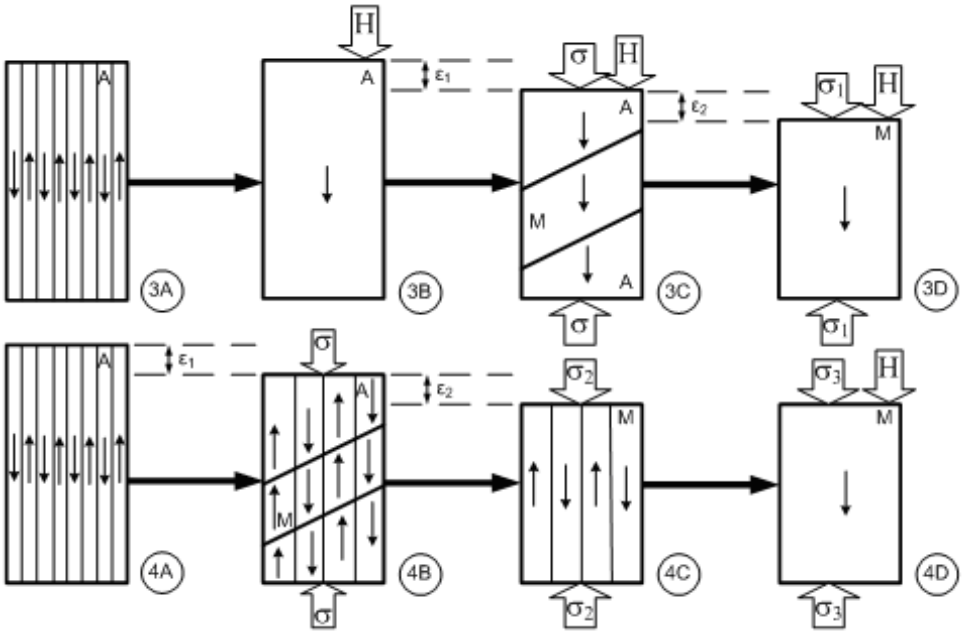


(a)

**Figure 4.16** Effect of magnetic field on a single crystal in three different configurations, (a) austenite and martensite are ferromagnetic and field is applied parallel to compressive stress, (b) austenite is paramagnetic, martensite is ferromagnetic and field is applied parallel to compressive stress, (c) austenite is paramagnetic, martensite is ferromagnetic and field is applied perpendicular to compressive stress.

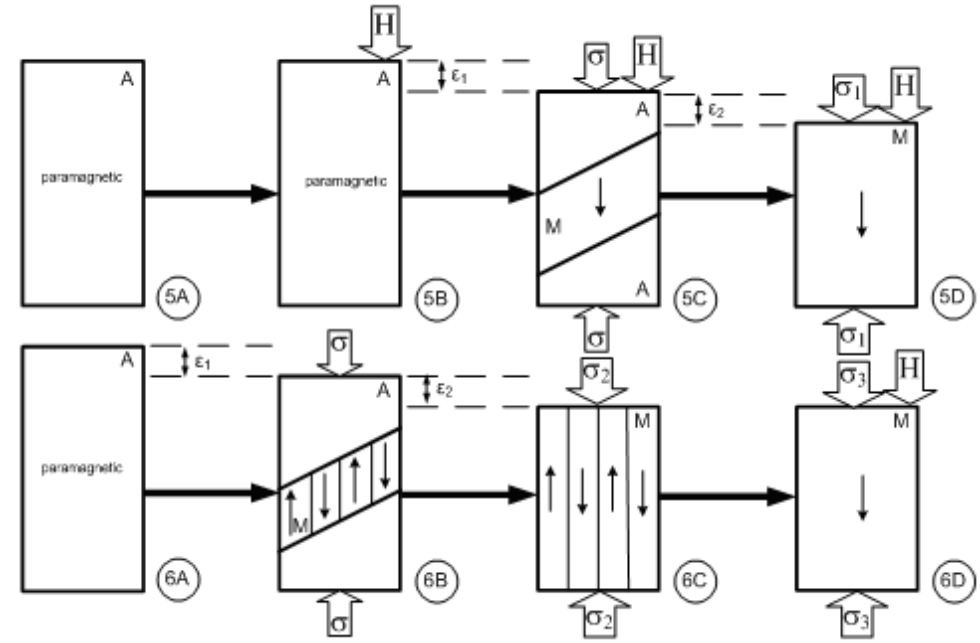


(b)

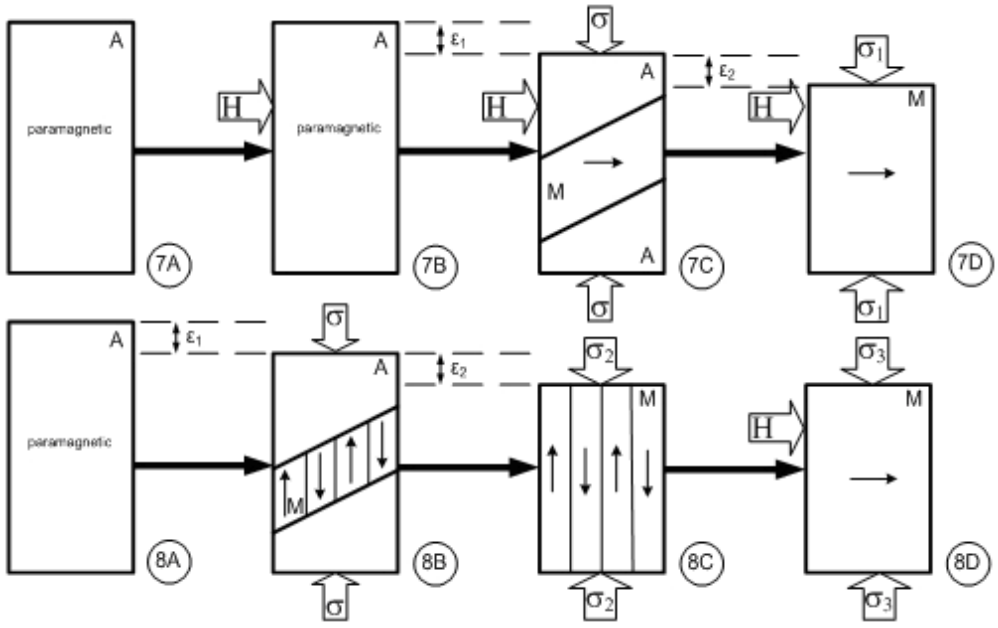


(c)

**Figure 4.16** Continued

**4.10 Actuation Stress and Work Output**

From the present data, the maximum stress level at which the reversible field-induced first stage phase transformation is possible is about 28 MPa, which is almost an order of magnitude higher than the blocking stress levels observed in the field-induced martensite variant reorientation in NiMnGa MSMAs. To compare the actuation performance of some of the published $Ni_2MnGa$ MSMA compositions with the present results, the mechanical work output per unit volume was considered as a figure of merit and constructed Figure 4.17 in logarithmic scale. It should, however, be noted that for the stress assisted field-induced phase transformations, the work output values have contributions from both magnetic ($W^{mag} = \sigma_{mag} \times MFIS_{max}$) and mechanical energy ($W^{mech} = \sigma \times MFIS_{max}$) terms. In other words, external stress and applied magnetic field act in parallel while they act in series in the case of field-induced martensite variant reorientation. Actuation performance due to the stress-assisted field-induced phase transformation is, thus, considered to be the total work output response of the material, triggered reversibly by applied magnetic field.

Figure 4.17 is divided into three regions. The first one marked on the left hand side shows the actuation stress and work output levels due to field-induced martensitic variant reorientation as introduced in Chapter III [26, 31, 46, 48]. The second region marked in the lower right hand corner demonstrates the present results for the reversible field-induced phase transformation in the first transformation stage (X-phase to 10M martensite). The work output in this region is similar to that from the field-induced variant reorientation (the first region), however, the actuation stress is almost one order of magnitude higher in the former. The solid line on the upper right hand corner (the third region) shows the actuation stress, MFIS, and work output levels from the one-way field-induced phase transformation (one-way shape memory effect) in the second transformation stage of the present alloy (*i.e.* between -80 and -40 °C). In this response, the work output increases from 660 to 1848 $kJm^{-3}$ as the temperature increases from -80 to -40 ˚C demonstrating that it is possible to achieve more than one order of magnitude higher work output and actuation stress as compared to that of field-induced variant

reorientation. At higher temperatures up to 10 °C, the stress level increases but the transformation is only one stage and the effect is one-way, thus, corresponding data points were not included in the figure. The third region also includes the area of anticipated performance levels that can possibly be achieved in NiMnGa alloys and other MSMAs. This requires identification of new alloy compositions and phase structures in which magnetic field application would separate the pseudoelastic stress hysteresis loops with and without field.

A work output of 115 $kJm^{-3}$ was obtained for the cyclic MFIS in the first stage transformation under 24 MPa actuation stress. The maximum work output of 1848 $kJm^{-3}$ was obtained in the second stage phase transformation at -40 $^{o}$C under 84 MPa. Note that these work output levels are significantly higher than those of currently available ferroelectrics and magnetostrictive materials [19, 94, 96].

It is clear that for the realization of reversible field-induced phase transformation, the stress and temperature-induced phase transformation characteristics should be well understood in terms of phase structure and temperature dependence of critical mechanical and magnetic properties. This is particularly important for NiMnGa alloys in which composition, orientation and stress state dependent multi-stage martensitic transformations have been reported [55]. As mentioned earlier, the multi-stage phase transformations in off-stoichiometric $Ni_2MnGa$ alloys can be a part of the four stage transformation sequence [55]. The alloy composition studied in this work experiences only the first two among which only the first stage was possible to reversibly induce by field. However, we also presented above that the mechanical and magnetic properties such as pseudoelastic stress hysteresis and magnetostress levels evolve differently with temperature for two different martensitic transformations implying the significance of temperature dependence of these properties. Therefore, it is crucial to explore the possibility of field activation in other transformation stages and clearly understand the effect of temperature and orientation on these stages. Note that the multi-stage martensitic transformation is not a requirement for the field-induced phase

transformation, however, it provides additional parameters to modify, and increases the possibility of observing reversible field-induced phase transformation.

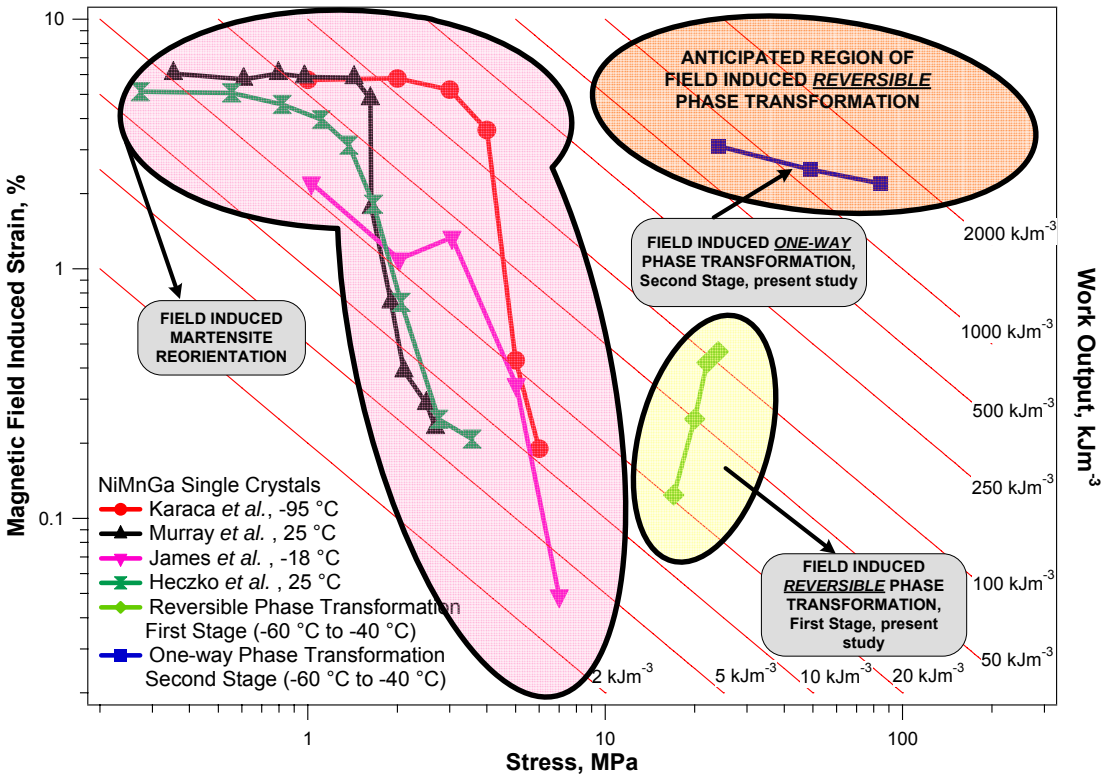


**Figure 4.17** MFIS and total work output vs. the actuation stress plots showing the literature data obtained to date utilizing field-induced martensite reorientation mechanism and the present results of field-induced reversible and irreversible phase transformations in NiMnGa MSMAs. The figure also shows a region of MFIS, actuation stress and work output that might possibly be achieved utilizing the simple guidelines introduced here and optimizing the suggested parameters. A grid of constant mechanical work output hyperbolas ranging from 2 and 2000 $kJm^{-3}$ has been superimposed. Logarithmic scale is used for both axes for easy comparison.

# CHAPTER V
# PHASE TRANSFORMATION IN NiMnCoIn ALLOYS

NiMnCoIn experiments were carried out on two different batches where compression is applied along the [100] crystallographic orientation and magnetic field along the [011] orientation. The single crystals for each batch were grown the same way under the same conditions however, due to Mn evaporation during the crystal growth process [77], the composition of each batch may be different.

## 5.1 Magnetization Results

Magnetization experiments were conducted in order to determine the magnetization of $Ni_{45.7}Mn_{35.6}Co_{4.8}In_{13.8}$ alloy as functions of temperature and magnetic field using SQUID. The change in magnetization as a function of magnetic field was determined cycling the magnetic field from 0 T to 7 T at different temperatures. The thermo-magnetic response of $Ni_{45.7}Mn_{35.6}Co_{4.8}In_{13.8}$ was determined via cycling the temperature from about 390K down to 50K under various magnetic fields. The resulting data was used to determine the effect of magnetic field on the transformation temperatures.

Figure 5.1 shows the change in magnetization with temperature under constant magnetic field for the as cast polycrystal, as grown single crystal and heat treated single crystal (at 900 ˚C for 24 hours). It is clear that heat treatment changes the transformation temperatures and temperature hysteresis decreases. It is essential to find the optimum heat treatment that would result in small stress hysteresis and large difference between the saturation magnetizations of transforming phases.

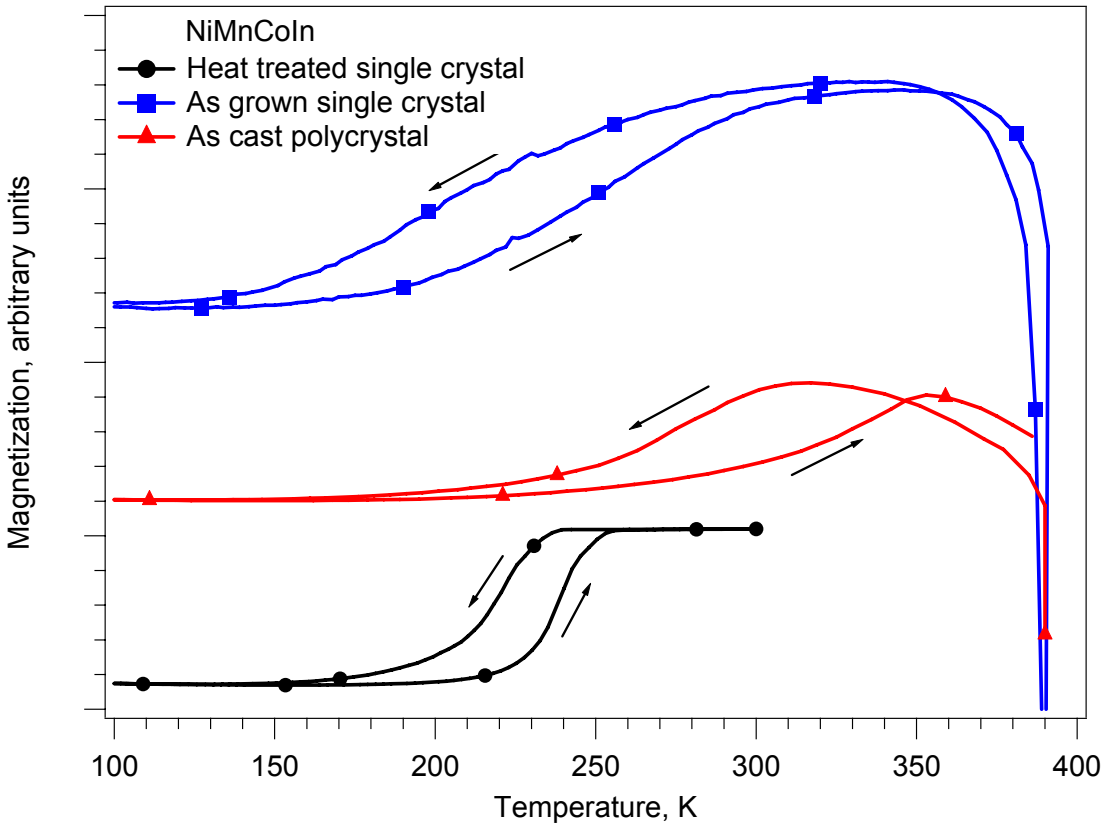


**Figure 5.1** The change in magnetization with temperature under constant applied magnetic field of 500 Oe for the as-cast polycrystal, as-grown single crystal and heat-treated single crystal of $Ni_{45.7}Mn_{35.6}Co_{4.8}In_{13.8}$ alloy. The decrease and increase in magnetization during cooling and heating indicate forward and reverse transformations respectively. The Curie temperature is 390 K.

Figure 5.2.a and 5.2.b shows the magnetization versus temperature and the corresponding dM/dT curves under constant field of the 0.05 T for batch 1 and 2, respectively. dM/dT curves are used to determine the transformation temperatures. The $M_s$, $M_f$, $A_s$ and $A_f$ temperatures are determined as 245, 163, 240 and 284 K for batch 1 and 181, 116, 195 and 248 K for batch 2, respectively. The transformation temperatures for batch 1 is higher than the ones of batch 2. This is attributed to the small compositional variations between the two batches due to evaporation of Mn during crystal growth.

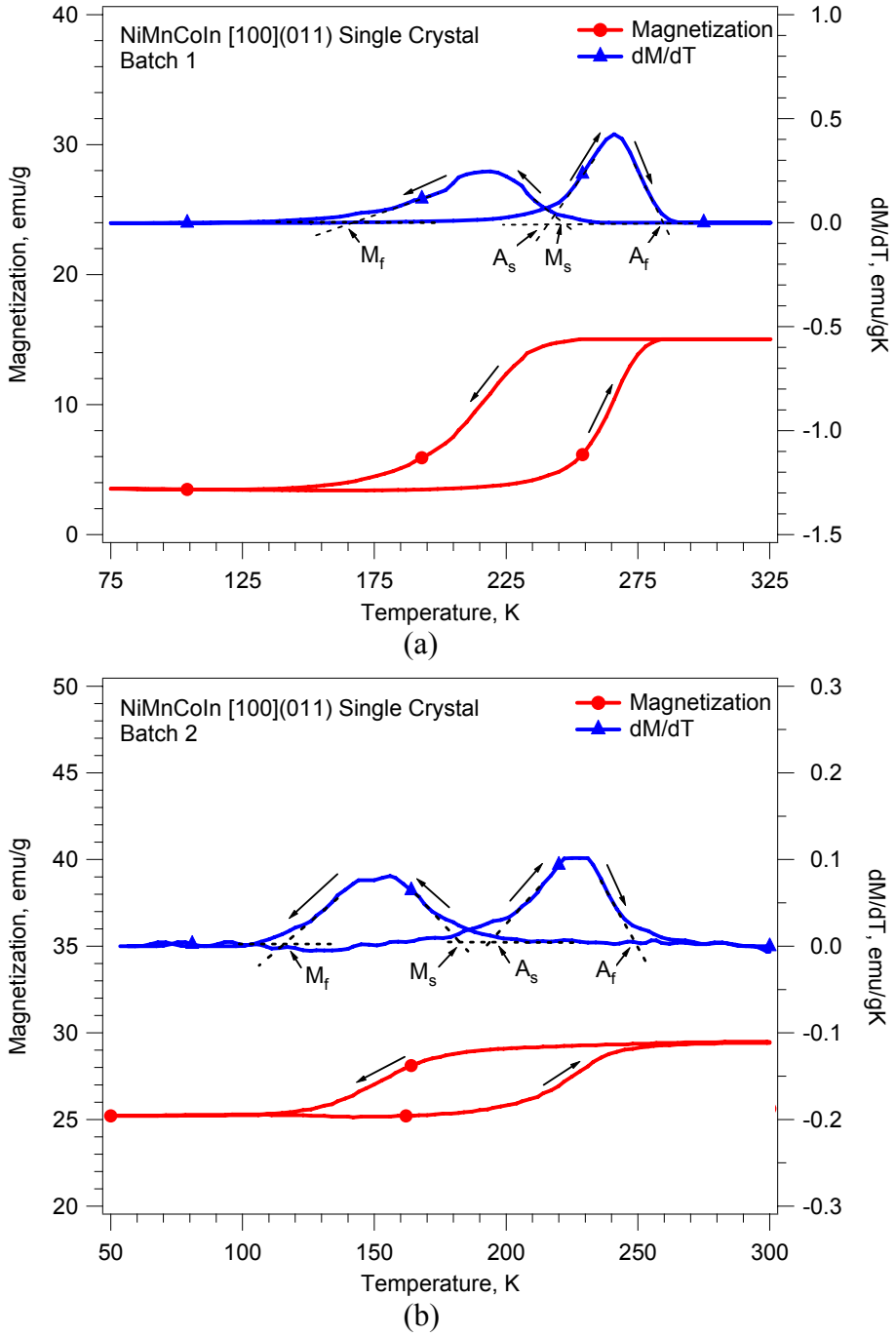


**Figure 5.2** Magnetization as a function of temperature under 0.05 T and its temperature derivative for NiMnCoIn, a) batch 1 and b) batch 2 single crystals. Each batch has grown with the same initial nominal composition of 45Ni-36.5Mn-5Co-13.5In (in at. %).

Figure 5.3.a shows the effect of applied magnetic field on the magnetization response of heat treated (900 ˚C for 24 hours) sample from batch 2. Heat treatment is done to achieve compositional uniformity through out the sample and remove internal stresses if there is any. As the applied magnetic field increases the transformation temperatures decrease. $M_s$ decreases from 230 K to 167 K as field is increased from 0.05 to 5T. This is called austenite stabilization and the reason is attributed to the fact that saturation magnetization of austenite is higher than saturation magnetization of martensite as it will be discussed in details. The shift in transformation temperatures provides us a unique opportunity to induce reversible phase transformation at certain temperature interval. Figure 5.3.b shows the change in magnetization as a function of applied magnetic field at 220 K and 140 K. At 220 K, the initial increase and following plateau till 1.5 T are due to the magnetization of martensite. The following increase in magnetization is due to phase transformation from martensite to austenite where it reaches its saturation at 4 T where martensite fully transforms to austenite. Unloading the magnetic field results in back transformation from austenite to martensite with a magnetic field hysteresis. At 140 K, the required magnetic field for the phase transformation is higher since we are far away from the austenite start temperature under no magnetic field and more magnetic energy is needed for transformation.

Figure 5.4.a shows the effect of applied magnetic field on the magnetization response of heat treated (900 ˚C for 24 hours) sample from batch 1. The effect of magnetic field is similar to one observed on batch 2 sample where transformation temperatures decrease as field strength increases. $M_s$ decreases from 232 K to 160 K as field is increased from 0.05 to 7 T. Figure 5.4.b shows the change in magnetization under the applied magnetic field at 250, 200, 150 and 50 K after cooling down to set temperatures under 0.05 T as shown in Figure 5.4.c. At 250 K, the initial phase is austenite (Figure 5.4.c) and it has a saturation magnetization of 95 emu/g. The increase in magnetization after 4 T is not well understood but it might be attributed to small amount of residual martensite that transforms to austenite. At 200 K, the initial phase is martensite and it transforms to the austenite as field is applied and transforms back to the

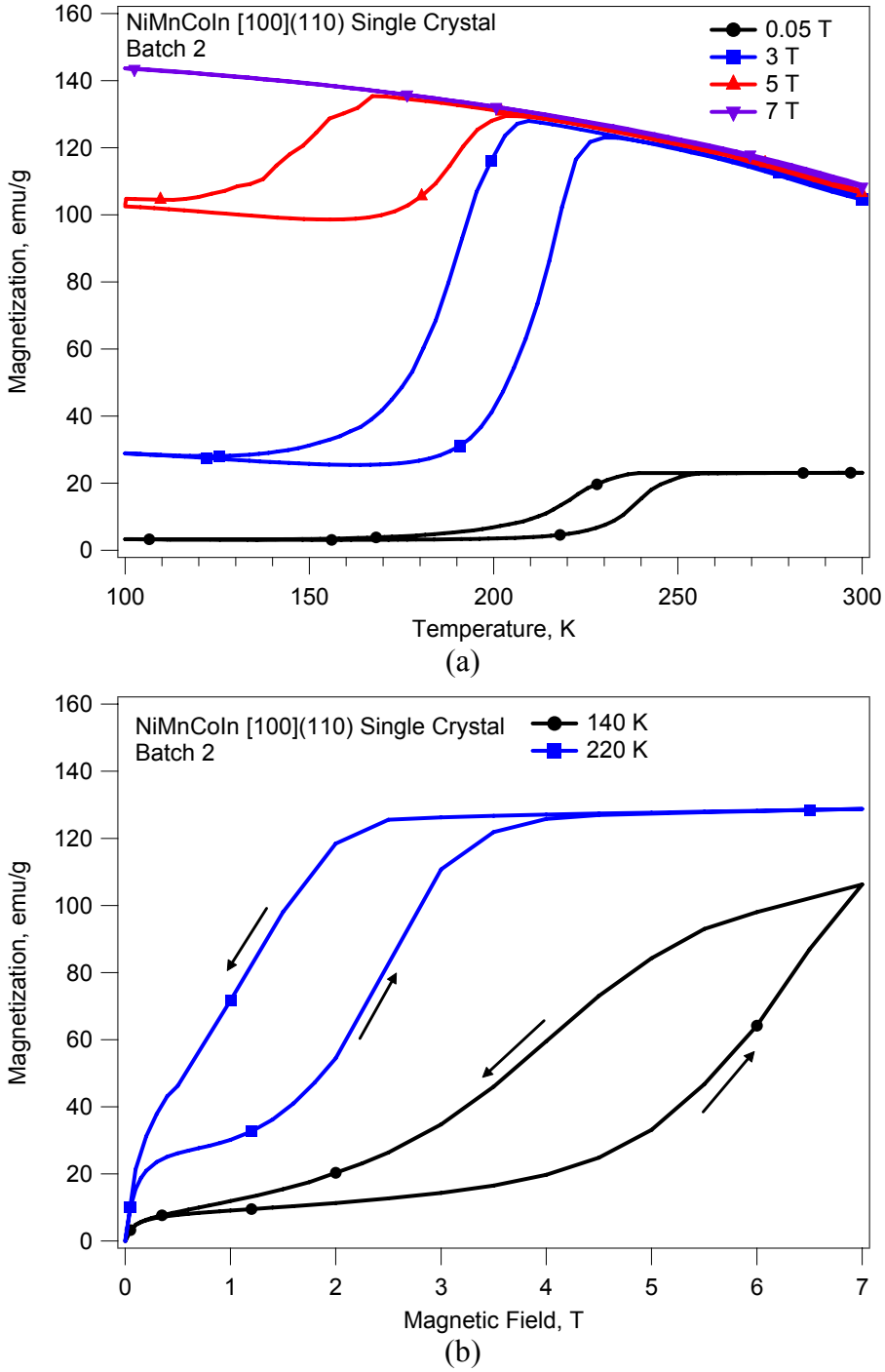


**Figure 5.3** Change in magnetization of batch 2 $Ni_{45.7}Mn_{35.6}Co_{4.8}In_{13.8}$ single crystal as a function of a) temperature under constant applied magnetic field and b) as applied magnetic field at 140 K and 220 K.

martensite when the field is removed and supported by the hysteretic behavior of the magnetization response. At 150 K and 50 K application of field does not result in any phase transformation up to 7 T. Saturation magnetization of martensite is about 15 emu/g. It is important to note that the magnetization of martensite is 135 emu/g after cooling down to 50 K under 7 T while it is 20 emu/g after cooling down to 50 K under 0.05 T and then, ramping the field to 7 T. It indicates that the saturation magnetization of martensite is path dependent.

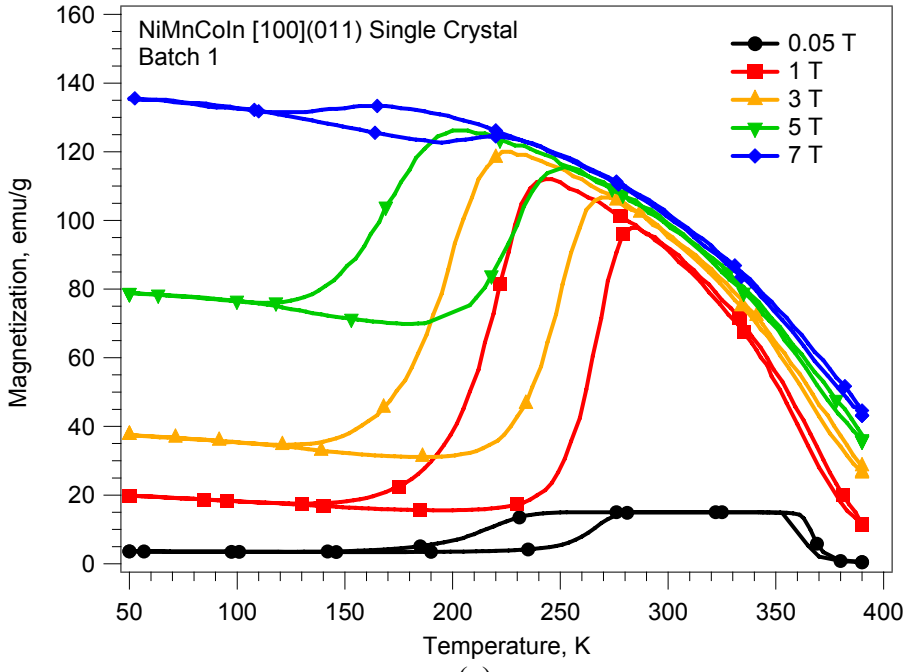


(a)

**Figure 5.4** Change in magnetization of batch 1 $Ni_{45.7}Mn_{35.6}Co_{4.8}In_{13.8}$ single crystals as a function of a) temperature under constant applied magnetic field and b) applied magnetic field at 50, 150, 200 and 220 K, and c) magnetization versus temperature curves for the data shown in (b) where the fields are ramped after cooling down to set temperatures under 0.05T.

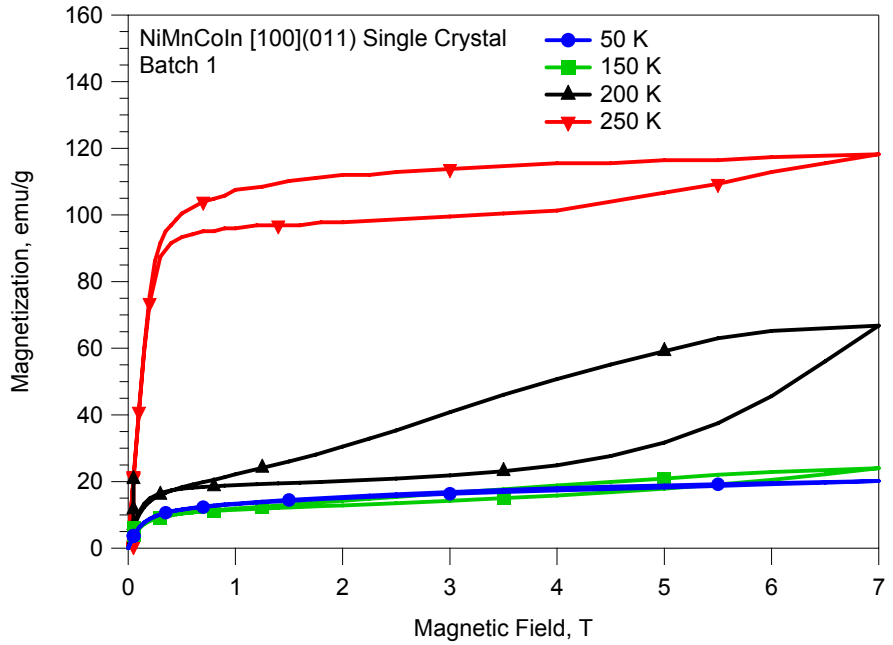


(b)

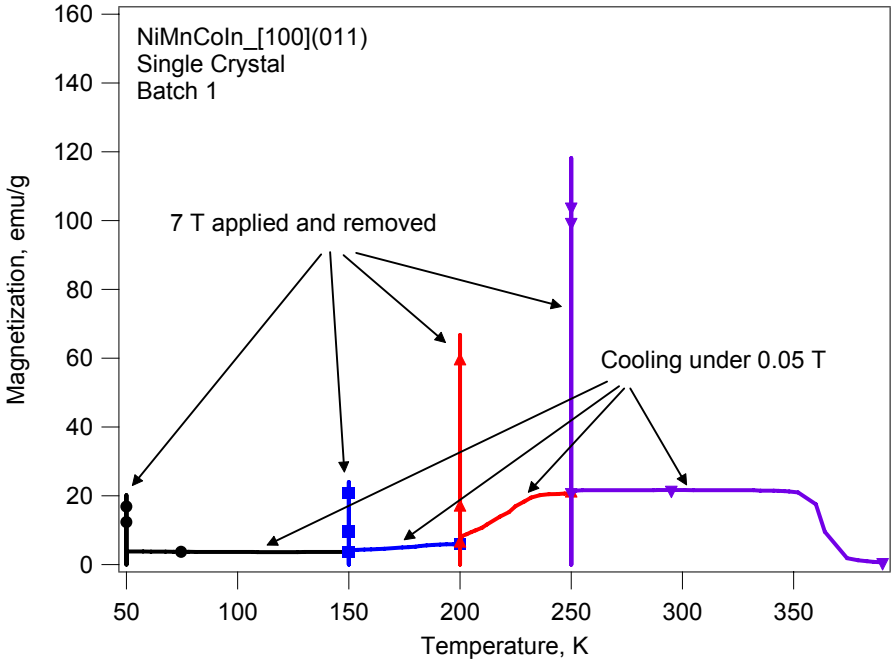


(c)

**Figure 5.4** Continued

Figures 5.5.a and b show the magnetization versus temperature and magnetization versus applied field responses of a batch 1 sample. The sample is cooled from 300 K to 50 K under 7 T, the start and finish points of cooling process are shown by #1 and #2 in the figure. Phase transformation from austenite to martensite occurs between 170 K and 120 K during cooling which could also be seen in Figure 5.4.a. The field is unloaded from 7 T to 0 T and Figure 5.5.b shows that when the field is decreased from 4.5 T to 1 T magnetization decreases substantially from 130 emu/g to 40 emu/g. The decrease is similar to change in magnetization during phase transformation (Figure 5.4.b). The response from 1 T to 0 T (shown by #3) is similar to magnetization response of martensite without any phase transformation due to only magnetization rotation and domain wall motion. When the field of 7 T is reapplied magnetization saturates at about 30 emu/g (<1 T) and there is no abrupt change in magnetization up to 7 T (#4). The increase in magnetization is linear upto 6 T where after 6 T, the magnetization increases more rapidly and reaches to 41 emu/g at 7 T. When the sample is heated under 7 T, the phase transformation from martensite to austenite occurs and magnetization increases from 40 emu/g to 120 emu/g at 220 K when the transformation completes (#5). Further heating results in decrease of magnetization due to thermal effects and at 390 K magnetization drops to 45 emu/g (#6). Similar experiments were done under 5, 3, and 1 T and it has been found that the peculiar behavior shown in Figure 5.5 can be observed for samples cooled down under fields higher than 3 T. The difference in magnetization between cooling down under a high field and cooling down under low field followed by applying high field to reach the same magnetization level as the former might be attributed to formation of another martensite phase. This pheonema can be similar to the formation of the X-phase in NiMnGa which occurs only under certain applied stress. For the NiMnCoIn alloys magnetic field replaces stress and an unknown martensitic phase might be forming at high field at certain temperature range. In situ XRD experiments under high fields are needed to resolve this issue.

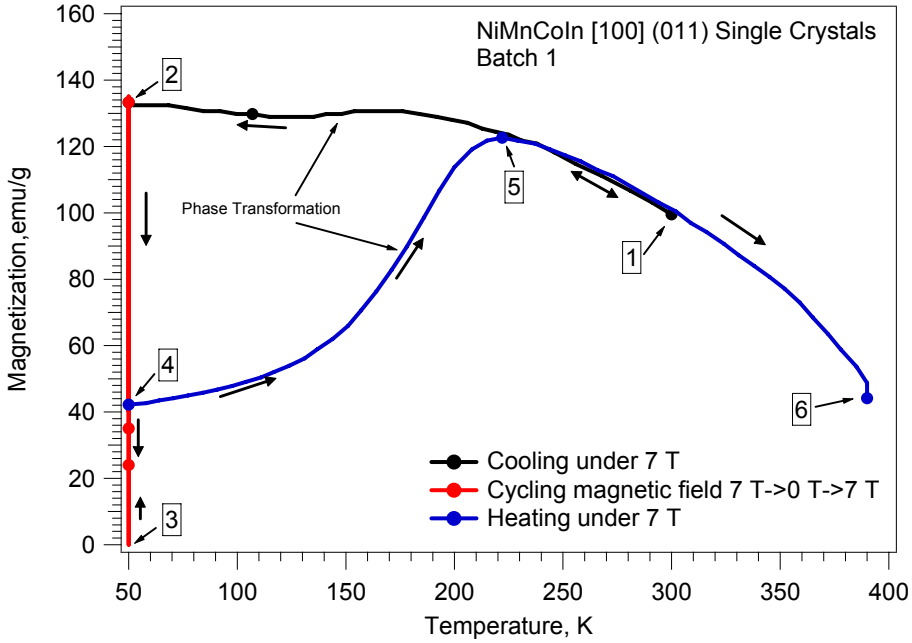


(a)

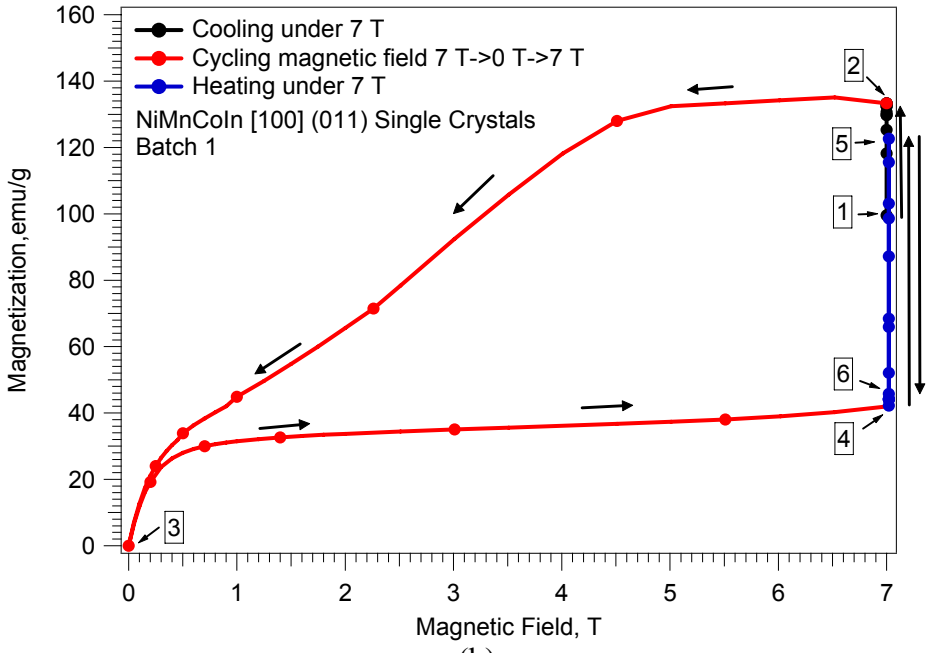


(b)

**Figure 5.5** Change in magnetization of batch 1 $Ni_{45.7}Mn_{35.6}Co_{4.8}In_{13.8}$ single crystal as a function of a) temperature and b) applied magnetic field. Sample is cooled down from 300 K to 50 K. The number sequence demonstrates the loading path.

## 5.2 Effect of Magnetic Field on the Pseudoelastic Response of NiMnCoIn Alloys

Figure 5.6 shows the compression pseudoelasticity experiments conducted at 0 °C, 20 °C, and 50 °C on a NiMnCoIn batch 2 specimen where the stress is applied along the [100] orientation. As expected, the critical stress for transformation increases with increasing temperature. The maximum transformation strain was obtained as 6.5%. The stress hysteresis is approximately 100 MPa at 0°C and increases with temperature. The pseudoelastic response does not show the complete phase transformation at 50 °C since the sample is failed at that temperature.

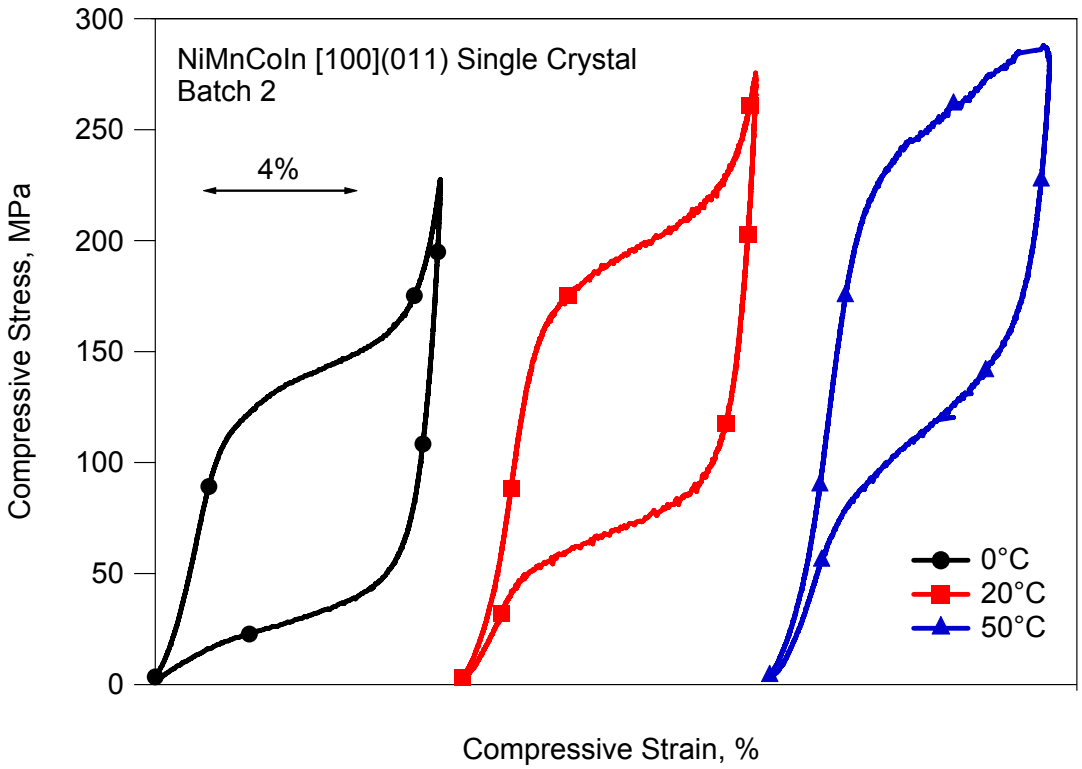


**Figure 5.6** Pseudoelastic response under compression along the [100] orientation of the $Ni_{45.7}Mn_{35.6}Co_{4.8}In_{13.8}$ batch 2 single crystal at 0, 20 and 50 ˚C.

Figure 5.7 shows the effect of magnetic field on the pseudoelastic response of a NiMnCoIn batch 2 single crystal under compression at 0 ˚C. Magnetic field is applied along the [110] orientation, perpendicular to the applied stress direction, prior to loading and kept constant throughout the experiment. Magnetic field magnitudes ranging from 0T to 1.6 T with increments of 0.4 T are applied in order to capture the magnetostress level as a function of applied field. As it can be seen in the figure, the NiMnCoIn single crystal exhibited an increase in the critical stress required for phase transformation with increasing magnetic field magnitudes.

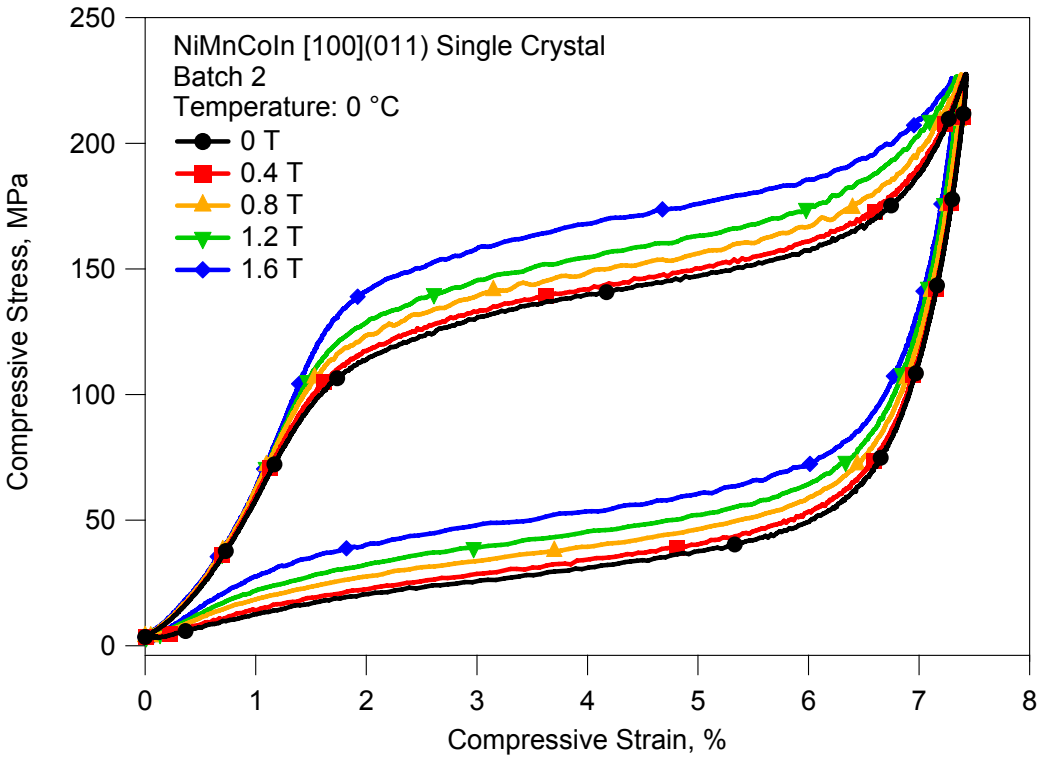


**Figure 5.7** Effect of magnetic field on the pseudoelastic response and the critical stress for the field-induced phase transformation of $Ni_{45.7}Mn_{35.6}Co_{4.8}In_{13.8}$ [100](011) batch 2 single crystal at 0 ˚C.

The magnetostress levels as a function of magnetic field for NiMnCoIn [100](011) batch 2 single crystal are determined at 4% strain from the curves shown in

Figure 5.7. The sample exhibits ~30 MPa magnetostress under 1.6T magnetic field. The magnetostress of 30 MPa under 1.6 T is much larger than other MSMAs (~5 MPa for NiMnGa alloys). The large magnetostress observed under 1.6T indicates that NiMnCoIn alloys as a very promising MSMA with high actuation stress output. It is important to note that there is no limit for maximum magnetostress in NiMnCoIn alloys and it is expected to increase with the field. This is due to the fact that that the available magnetic energy for phase transformation in NiMnCoIn alloys stems from the difference in magnetization magnitudes of austenite and martensite phases not from MAE which is limited by a critical magnetic field. This fact will be discussed in detail in the next chapter.

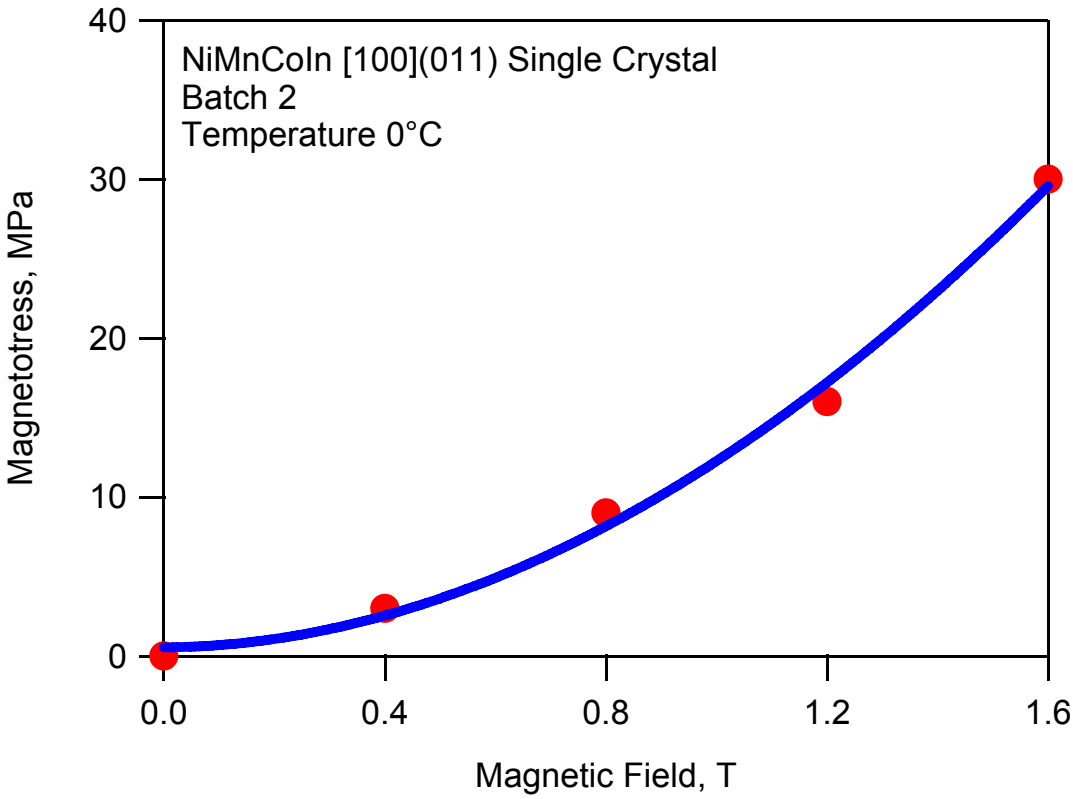


**Figure 5.8** Magnetostress as a function of magnetic field for the $Ni_{45.7}Mn_{35.6}Co_{4.8}In_{13.8}$ [100](011) batch 2 single crystal determined at 4% strain from the curves shown in Figure 5.7. The sample exhibits ~30 MPa magnetostress under 1.6T magnetic field.

### 5.3 Synchrotron X-ray Results

Synchrotron-based high-energy x-ray diffraction techniques provide an *in-situ* tool for advancing the understanding of many physical processes such as deformation, phase transformation, and recrystallization [79]. In the present work, this method is used to capture the structural evolutions in the present NiMnCoIn alloy during the phase transformation with and without applied magnetic field. Figure 5.9 shows the diffraction image plate and the corresponding 2-D intensity versus 2θ graph at 300 K in austenite. A mask is put in the center to remove the effect of a residual peak in the image plate. The arrows show the cubic directions of the austenite phase. The structure is determined to be $L2_1$ with lattice constant of a= 0.5979 nm. The peaks shown in Figure 5.9.a are indexed and shown in Figure 5.9.b. Figure 5.10 shows the diffraction image plate and the corresponding 2-D intensity versus 2θ graph at 180 K in martensite phase. The modulations in the structure are pointed in the graph and the structure is determined to be 12M. The lattice parameters are determined as a=0.441 nm, b=0.556 nm, c= 2.602 nm and ß=96.2°.

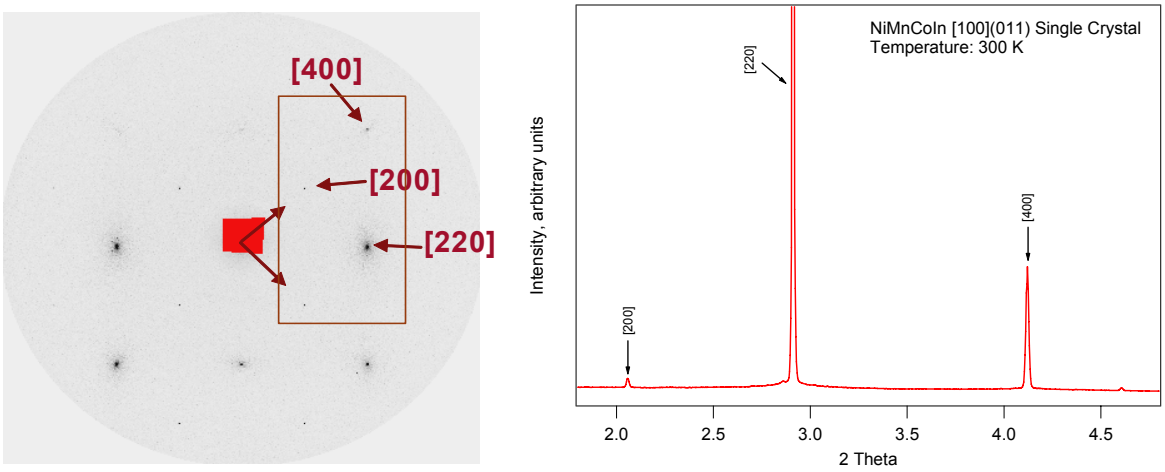


(a)

(b)

**Figure 5.9** a) The diffraction image plate and b) the corresponding 2-D intensity versus 2θ graph of the $Ni_{45.7}Mn_{35.6}Co_{4.8}In_{13.8}$ single crystal at 300 K. The crystal structure is determined to be $L2_1$.

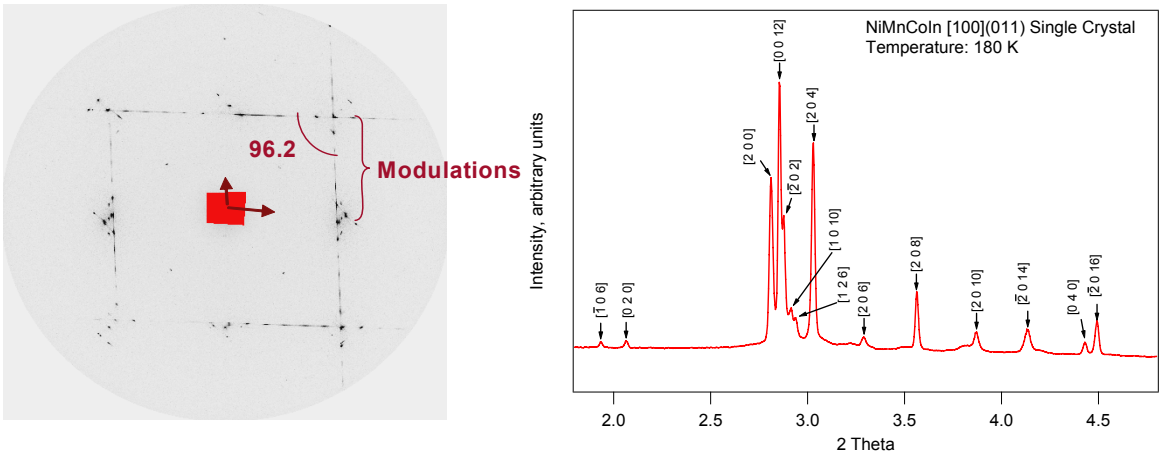


(a) (b)

**Figure 5.10** a) The diffraction image plate and b) the corresponding 2-D intensity versus 2θ graph of the $Ni_{45.7}Mn_{35.6}Co_{4.8}In_{13.8}$ single crystal at 180 K. The crystal structure determined to be 12M where the modulations are marked.

*In-situ* phase transformations with temperature and magnetic field are studied to reveal the microstructural details of phase transformations. The sample was cooled down from 300K to 10 K and heated up back to 300K and at every 10K increments, the x-ray diffraction data is recorded. Figure 5.10 shows the Intensity versus 2θ response during cooling till 200 K. The peaks are determined only in the region shown by a rectangle in Figure 5.9 for clarity. At 240K, the structure is completely austenite and at 230K martensite peaks start to emerge and at 220K it completely transforms to martensite. Further cooling down to 10 K only results in minor changes in lattice parameters and monoclinic angle. During heating as shown in Figure 5.11 back transformation starts at 250 K and at 260 K the martensite transforms completely to austenite.

The same experiments are also conducted under the applied field of 7 T to reveal the effect of applied magnetic field, however, no phase transformation is observed down to 10 K. This provides an opportunity to induce phase transformation by magnetic field similar to the one shown by SQUID experiments (Figure 5.3). The sample is cooled down from 300 K to 200 K under no magnetic field and it transformed to martensite.

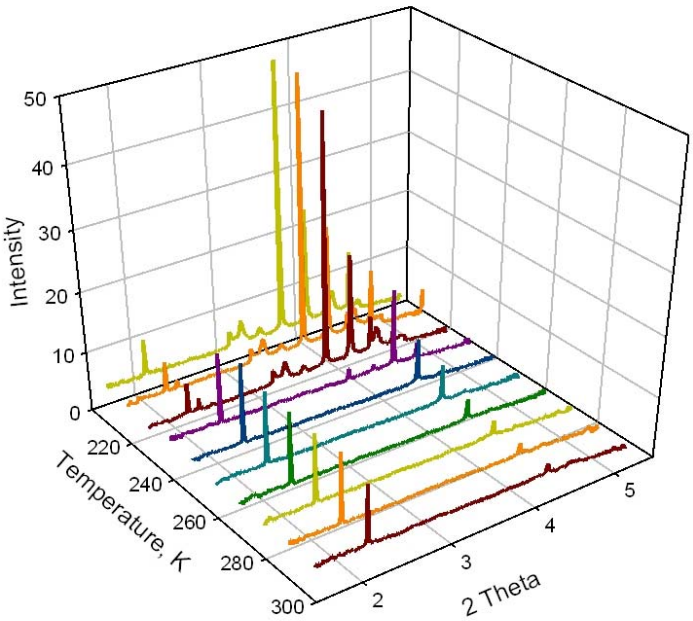


(a)

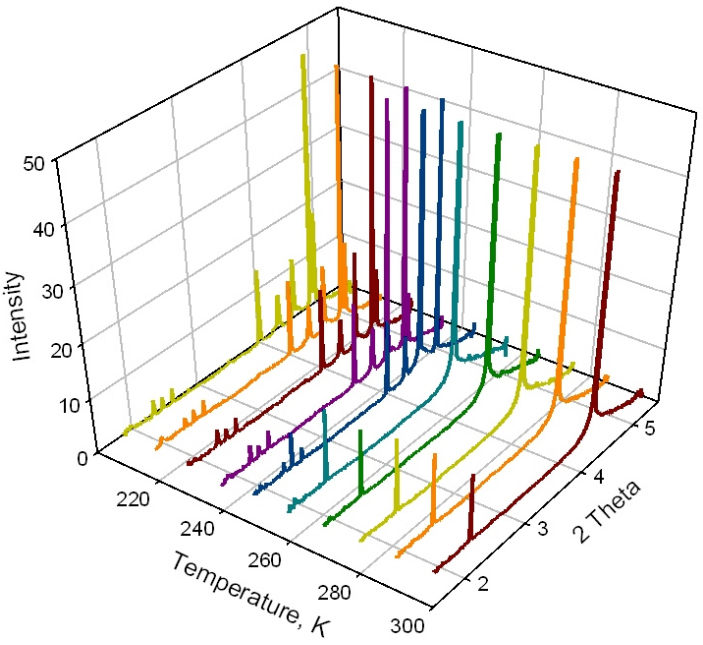


(b)

**Figure 5.11** 2-D intensity versus 2θ plots of the $Ni_{45.7}Mn_{35.6}Co_{4.8}In_{13.8}$ single crystals between 200 K and 300 K during a) cooling and b) heating under no magnetic field.

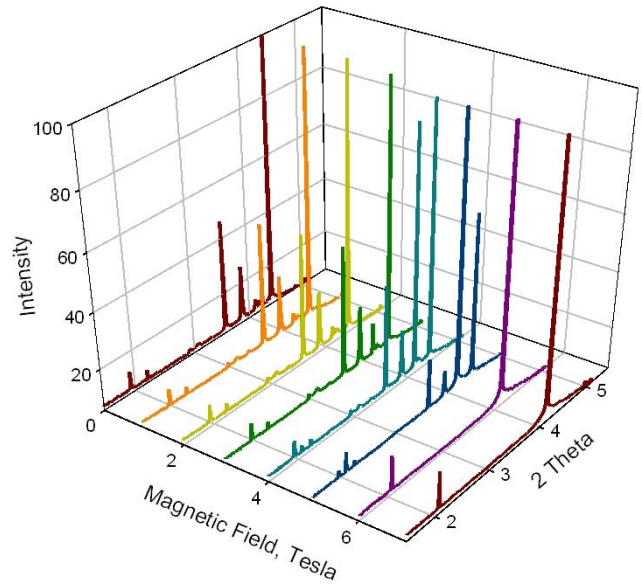


(a)

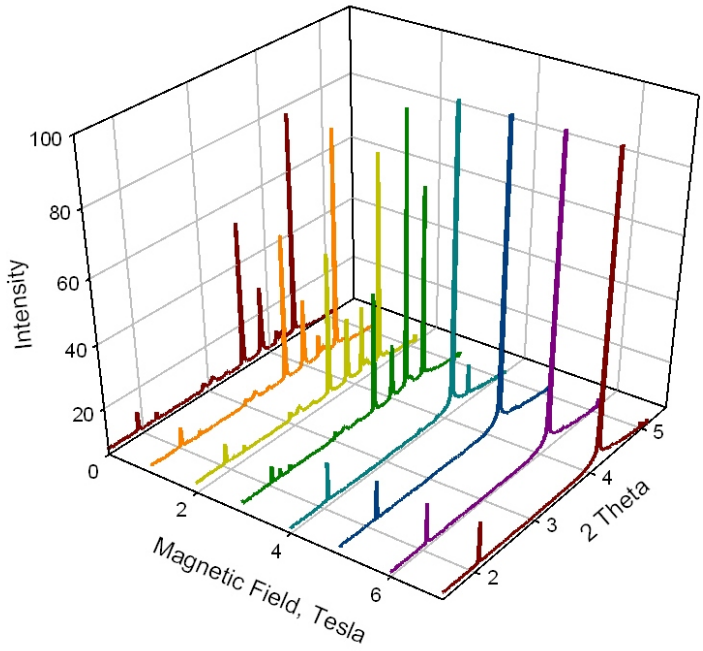


(b)

**Figure 5.12** 2-D intensity versus 2θ plots of $Ni_{45.7}Mn_{35.6}Co_{4.8}In_{13.8}$ single crystals at 200 K a) magnetic field is applied from 0 T to 7 T and b) field is unloaded from 7 T to 0 T with 1 T intervals.

Then, magnetic field is applied with 1 T increments up to 7 T. Corresponding intensity versus 2θ plots are shown in Figure 5.12.a. Martensite starts to transform to austenite at 3T and transformation continues up to 5 T. Between 5 T and 6 T all martensite transforms to austenite. When the field is removed austenite starts to transform back to martensite since it is no longer stable at that temperature range as shown by Figure 5.12.b. At 4 T small volume fraction of austenite transforms to martensite, at 3 T most of the austenite transforms to martensite and at 2 T the structure is completely martensite. Figure 5.12 shows in situ reversible field induced phase transformation in NiMnCoIn single crystals.

### 5.4 Theoretical Transformation Strain and Detwinning Strain in NiMnCoIn Alloys

One of the main actuation properties is the actuation strain. In NiMnCoIn alloys, the actuation strain is the transformation strain and it is orientation dependent as in all the shape memory alloys. The origin of the orientation dependence of the shape memory strain is mainly the crystallographic relation between the applied stress direction and possible crystallographic systems (transformation shear plane - also known as habit plane - and direction) for parent to martensite transformation. By using "Energy Minimization Theory", it is possible to determine habit plane and direction as well as twinning shear and direction for given lattice parameters. For more detailed description of the theoretical framework, please refer to [97, 98].

A CVP is a formal term for two twin related martensite variants and stands for "correspondent variant pair". Each martensite CVP is described by a unique habit plane normal, **m**, and transformation shear, **b** (see Figure 5.13 for a schematic) [97].

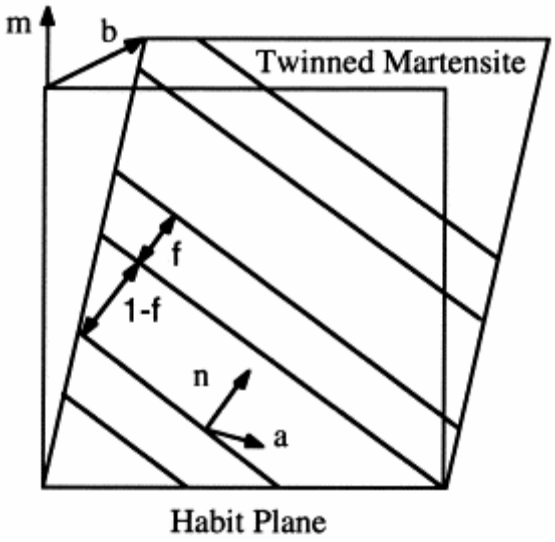


**Figure 5.13** Twin (**n**) and habit (**m**) planes, and twin shear (**a**) and macroscopic shear (**b**) of martensite [97].

In NiMnCoIn alloys; parent phase has $L2_1$ structure while martensite has 10M, 12M or 14M monoclinic crystal structures [14, 80]. There are total of 12 variants for cubic to monoclinic phase transformation [97]. In the parent phase coordinate system, the lattice deformation matrices to obtain these variants can be designated as $\boldsymbol{U_i}$.

For a given variant pair, the twin plane $\boldsymbol{n}$ and twin shear $\boldsymbol{a}$ can be determined provided that the plane is an invariant plane (unrotated and undistorted) using;

$$\boldsymbol{R_{ij}U_j - U_i = a \otimes n} \tag{5.1}$$

where $\boldsymbol{R_{ij}}$ is an orthogonal tensor and represents the relative rotation between the two variants satisfying $\boldsymbol{R_{ij}^T R_{ij} = I}$ ($\boldsymbol{I}$ is second rank identity tensor and the superscript $T$ represents the transpose of a matrix). The $\otimes$ represents a dyadic product. The twinned martensite is composed of variant pairs with a certain volume ratio. When there are finite number of twin layers, the deformation of martensite, $F_M$ is represented as;

$$\boldsymbol{F_M = R_h\left\lfloor fR_{ij}U_j + (1-f)U_i\right\rfloor} \tag{5.2}$$

where $\boldsymbol{U_i}$ and $\boldsymbol{U_j}$ are two variants in the twinned martensite and *(1-f)* and *f* are respective volume fractions. The tensor $\boldsymbol{R_h}$ is the relative rotation between the twinned martensite

and the parent phase. The habit plane $\boldsymbol{m}$ and transformation shear $\boldsymbol{b}$ can be obtained using;

$$\boldsymbol{F_M} - \boldsymbol{I} = \boldsymbol{b} \otimes \boldsymbol{m} \tag{5.3}$$

where $\boldsymbol{I}$ is the identity tensor representing the undeformed austenite. In these equations, the known parameters are $\boldsymbol{U_i}$, $\boldsymbol{U_j}$, and all the other unknowns can be solved from the equations.

Once the habit plane normal and transformation shear are determined, it is possible to find the transformation strain as;

$$\boldsymbol{\varepsilon} = \frac{1}{2}\left(\boldsymbol{F_M^T}.\boldsymbol{F_M} - \boldsymbol{I}\right) = \frac{1}{2}\left[\boldsymbol{b} \otimes \boldsymbol{m} + \boldsymbol{m} \otimes \boldsymbol{b} + (\boldsymbol{b}.\boldsymbol{b})\boldsymbol{m} \otimes \boldsymbol{m}\right] \tag{5.4}$$

The detwinning strain can be found by considering the conversion of the small fraction variant to the large one. The deformation can be determined as

$$F_M^{dt} = R_h U_i \qquad \text{for } f < 0.5 \tag{5.5}$$

$$F_M^{dt} = \mathrm{R_h}.(U_i + a \otimes n) \qquad \text{for } f > 0.5 \tag{5.6}$$

The total strain by detwinning can be determined similar to equation (5.4) once $F_M^{dt}$ is known (Equations 5.5 and 5.6). It is important to note that for NiMnGa alloys (Figure 1.7) the stress required for detwinning is very low compared to NiMnCoIn [93] and NiTi [97] and for these alloys it is better to compare the experimental results with the theoretical results with detwinning.

The resolved shear stress factor (RSSF) is calculated using

$$\mathrm{RSSF} = (\boldsymbol{b}.\boldsymbol{e})(\boldsymbol{m}.\boldsymbol{e}) / |\boldsymbol{b}| \tag{5.7}$$

where $\boldsymbol{e}$ denotes the single crystal loading direction. RSSF can be used to calculate the stress required for SIM along different orientations if the critical RSSF is known.

The lattice parameters determined from high energy X-ray diffraction are used to determine volume fraction, habit plane normal, transformation shear and twinning direction as shown by Table 5.1

The RSSFs for cubic to $L1_0$ transformation are 0.611, 0.377and 0.531 for the [100], [011] and [123] orientations, respectively. From these values, one would expect a

lower applied stress to start SIM in the [100] orientation than that required in other orientations provided that the materials are in the same thermal condition.

**Table 5.1** Volume fraction, habit plane, transformation shear and twinning direction for $Ni_{45.7}Mn_{35.6}Co_{4.8}In_{13.8}$ single crystals determined by energy minimization method.

| | Volume Fraction f | Habit plane normal m | Transformation shear b | Twinning direction a |
|---|---|---|---|---|
| | | | | |
| 12M | 0.232 | (0.121 0.691 -0.712) | <0.101 -0.086 -0.015> | {0 -0.148 -0.165} |
| 12M | 0.221 | (0.121 0.691 -0.712) | <0.101 -0.086 -0.015> | {0 -0.148 -0.165} |
| 12M | 0.219 | (0.073 0.698 -0.712) | <0.001 0.057 0.079> | {0 -0.156 -0.164} |

The experimental and theoretical transformation strains are summarized in Table 5.2. The maximum strain is obtained along the [100] orientation as 6.76 % where the experimental value is 6.5 %. This shows that calculations are in good agreement with the experiments. The transformation strains along the [123] and [110] directions are 4.15 % and 3.37 % for CVP formation. The detwinning strains along the [100], [123] and [110] orientations are calculated as 6.76 %, 4.59 % and 4.57 %, respectively. Along the [100] orientation, detwinning is not expected. The difference between the experimental and theoretical strains might be attributed to the detwinning during superelastic deformation due to high applied stress.

**Table 5.2** Comparison of experimentally observed and theoretically calculated phase transformation strains for $Ni_{45.7}Mn_{35.6}Co_{4.8}In_{13.8}$ single crystals along the three orientations.

| | % Strain for $L2_1$ to 12M phase transformation | | |
|---|---|---|---|
| | Experimental | Theoretical | |
| | SME | Transformation | Detwinned |
| 100 | 6.5 | 6.76 | 6.76 |
| 123 | | 4.15 | 4.59 |
| 110 | | 3.37 | 4.57 |

**5.5 Prediction of Magnetostress in NiMnCoIn Alloys**

It is possible to predict the magnetostress as a function of applied field if the change of critical stress with temperature (the slope of Classius-Clapeyron curves) and the change of transformation temperature with applied field is known. The change in critical stress with temperature can be given as;

$$\frac{\Delta\sigma}{\Delta T} = -\frac{\Delta H_{enth}}{T_o \varepsilon_o} \tag{5.1}$$

where $\Delta H_{enth}$ is the change in enthalpy during transformation, $T_o$ is the chemical equilibrium temperature, and $\varepsilon_o$ is the transformation strain. The transformation strains of single crystals can be calculated as shown in section 5.4 or it can be determined from pseudoelasticity and thermal cycling under stress experiments they have been conducted on NiMnGa alloy.

The change in transformation temperatures with applied field can be determined from magnetization results as shown in Figures 5.3 and 5.4. Then the magnetostress as a function of field can be determined as;

$$\frac{\Delta\sigma}{\Delta H} = \frac{\Delta\sigma}{\Delta T} x \frac{\Delta T}{\Delta H} \tag{5.2}$$

The compressive transformation strains for the [100], [123] and [110] orientations are calculated as 6.76, 4.15 and 3.37 in the previous section and Brewer [93] reported that these values fit well with the experimental values. From Figure 5.6, the change in critical stress with temperature can be determined as 1.72 MPa/ K. Classius-Clapeyron slopes for other orientations can be calculated assuming the same enthalpy and chemical equilibrium temperature for all samples since they are not a function of orientation. The change in transformation temperatures as a function magnetic field can be determined from Figure 5.4 as 12.6 K/Tesla. This is value is also considered to be orientation independent neglecting the effect of MAE if there is any. Table 5.3 shows the calculated magnetostress per applied field as a function of orientation. The experimental values are indicated by "*". The $\frac{\Delta\sigma}{\Delta H}_{theoretical}$ shown in Table 5.3 for the

[100] orientation is 21.6 MPa/Tesla which close to $\frac{\Delta\sigma}{\Delta H}_{experimental}$ magnitude determined as 18.7 MPa/Tesla from Figure 5.8 which shows the good agreement between the experimental and theoretical findings.

**Table 5.3** Orientation dependence of magnetostress as a function of applied field. * indicates the experimental values where all others are theoretical values.

| | $\varepsilon_o$ **%** | $\frac{\Delta\sigma}{\Delta T}$ **MPa/K** | $\frac{\Delta T}{\Delta H}$ **K/Tesla** | $\frac{\Delta\sigma}{\Delta H}_{theoretical}$ **MPa/Tesla** | $\frac{\Delta\sigma}{\Delta H}_{experimental}$ **MPa/Tesla** |
|---|---|---|---|---|---|
| **[100]** | 6.76 | 1.72* | 12.6* | 21.6 | 18.75* |
| **[123]** | 4.15 | 2.8 | 12.6* | 35.3 | |
| **[110]** | 3.37 | 3.45 | 12.6* | 43.5 | |

It is important to note the $\frac{\Delta\sigma}{\Delta H}_{theoretical}$ along the [110] orientation is 43.5 MPa/Tesla two times larger than the one in the [100] orientation. However the transformation strain along the [110] orientation is half of the transformation strain along the [100] orientation. These calculations suggests that if actuation stress is more critical than actuation strain, it would be better to choose an orientation with small transformation strain e.g [110] orientation or if actuation strain is more important, then an orientation with large transformation strain e.g [100] should be chosen. Additionally, it would be possible to induce reversible stress-assisted field-induced phase transformation at lower magnetic fields in [110] orientation compared to [100] orientation by assuming the same stress hysteresis in both orientations. Brewer [93] reported that thermal hysteresis along [123] and [100] orientations are similar which is a good indication that the stress hysteresis of both orientations could be close too. It should be kept in mind that stress hysteresis is a function orientation, transformation

strain, and temperature as well as loading state such as tension, compression, torsion, etc.

### 5.6 Optical Microscopy and Compositional Analysis of NiMnCoIn Alloys

The stress and temperature hysteresis of NiMnCoIn alloys are large when compared to NiMnGa alloys which results in need for high applied magnetic fields for phase transformation although the magnetostress per 1 T applied field is much higher than NiMnGa alloys.

Stress hysteresis in SMAs depends on the compatibility between the phases, lattice parameters, elastic moduli and the strength of the phases. Similar to thermal hysteresis, stress hysteresis or energy dissipation can arise from structural defect formation during transformation such as dislocations due to a large degree of lattice incompatibility between the parent and martensite phases and frictional energy spent on the movement of the phase front which depends on lattice friction and thus the crystal structure. Cui et al. [99] reported a theoretical framework that shows the degree of lattice incompatibility and how lattice parameters and crystal structures of transforming phases affect the incompatibility. They propose two criteria on the transformation matrix (**U**, also known as transformation stretch tensor which maps the martensite lattice to the parent phase lattice) that indicate the degree of lattice incompatibility between the two phases [99]. They have used this approach in search for low thermal hysteresis compositions in the NiTiCu alloy system [99].

The first criterion for the martensite-parent lattice incompatibility is (1/3)Trace(**U**)=1, which signifies no change in volume due to the transformation [99]. The second criterion is that the middle eigenvalue of **U** (that is the one of intermediate magnitude of the three) should be as close to unity as possible. This means that the parent phase is directly compatible with a single variant of martensite. In other words, an undistorted plane exists between the parent phase and martensite. If this condition is met exactly, there is no need for an additional shear, known as the lattice invariant shear, to ensure an invariant plane and only rotation is needed. The tensor **U** is a function of

crystal structures of the phases and the lattice parameters [99]. One can easily find **U** by determining the lattice parameters and crystal structure using XRD. Thus, by variation of compositions, determining the structures and lattice parameters and using these two criteria, one can find out which compositions in an alloy system would result in the minimum hysteresis. If this eigenvalue is exactly one, then the elastic energy storage at the phase front will be small and martensite does not form internal twins to satisfy lattice invariant shear criteria. Therefore, the applied stress or temperature change should not need to be high for phase front to move back and forth.

Note that lattice parameters are a function of temperature, and martensite and parent phase lattice parameters can change differently with temperature. Moreover, the lattice strength of the phases can also show dissimilar trends as a function of temperature. Thus, one also needs to look at how stress hysteresis changes with temperature as the compositions with minimum hysteresis may vary with temperature. This can only be done by physically measuring the stress hysteresis at different temperatures as it is difficult to determine the lattice parameters of two phases at the same temperature. Moreover, lattice strength is also important for stress hysteresis. For example, off-stoichiometric alloys demonstrate higher strength levels. Even though stoichiometric alloys show increase in stress hysteresis with increasing temperature and stress levels due to ease of defect generation (such as in NiTi [100]), off-stoichiometric alloys can demonstrate the opposite due to their high strength levels (such as in CoNiAl and NiTi [38, 39, 100, 101]).

If the composition is fixed, as in this study, stress hysteresis can be changed by heat treatments by forming a second phase (or precipitates) which would have a different composition than the matrix. By changing the volume fraction of second phase, the composition of the matrix can be engineered. Figure 5.14 shows an optical image of NiMnCoIn single crystal heat treated at 900 ˚C for 24 hours. The formation of second phase through out the sample can easily be seen.

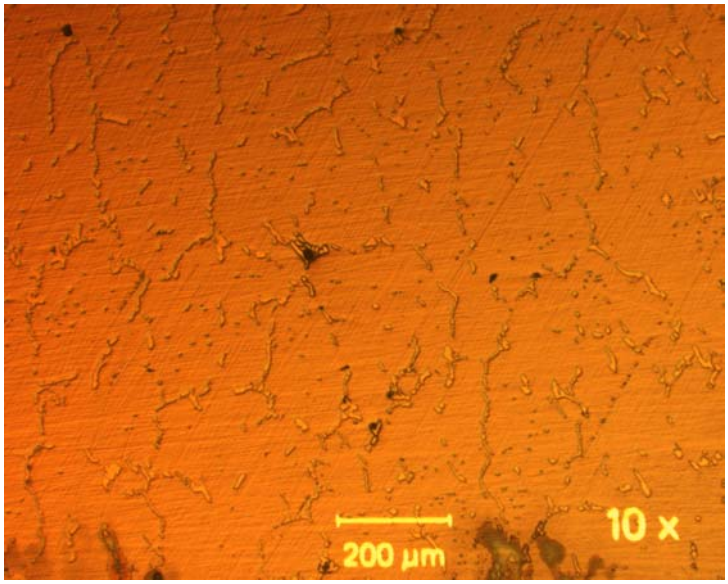


**Figure 5.14** Optical micrograph of the heat treated $Ni_{45.7}Mn_{35.6}Co_{4.8}In_{13.8}$ [100](110) single crystal. Formation of second phase is evident.

Figure 5.15 shows electron back scattering image of a heat treated NiMnCoIn [100](110) single crystal. The formation of the second phase is also evident in this image where the contrast changes mean change in average atomic weight. The gray areas are the second phases and dark areas are related to sulfur inclusion in the matrix. WDS measurements are performed on the sample and the compositions of matrix and second phase are determined as $Ni_{45.7}Mn_{35.6}Co_{4.8}In_{13.8}$ and $Ni_{42.0}Mn_{40.3}Co_{16.0}In_{1.6}$ where the nominal composition is $Ni_{45}Mn_{36.5}Co_{5}In_{13.5}$ (at%). The second phase is found to be cobalt rich. In CoNiAl alloys, formation of Co-rich FCC second phase is found to drastically improve the ductility of the alloy. In NiMnCoIn alloys, it is not clear whether formation of second phase improves the ductility or not. The tested samples with the same heat treatment as the one shown in Figure 5.13 showed brittle behavior in the MTM experiments. A systematic investigation is needed to determine the effect of second phase on the magnetic and conventional shape memory characteristics of NiMnCoIn alloys. However, the possibility of formation of second phase gives us the ability to engineer the material without changing the nominal composition. The amount of Sulfur content in the samples are determined to be 0.005 wt% using the combustion-

infrared absorbance method. The low content of sulfur suggests that it is unlikely to be the primary reason for the brittleness of the samples.

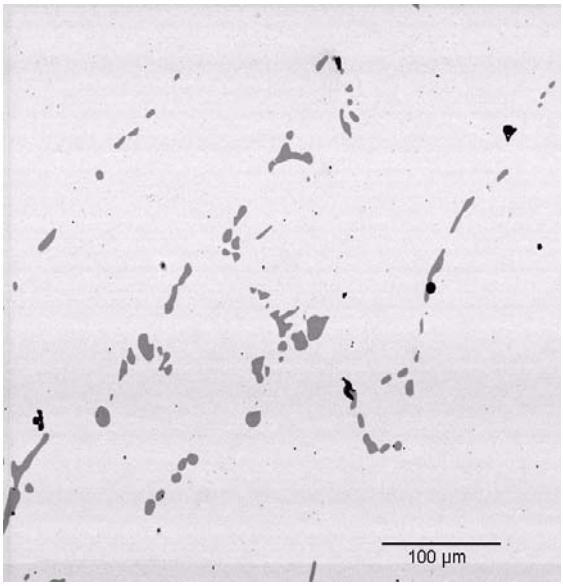


**Figure 5.15** Electron back scattering image of the NiMnCoIn [100](110) heat treated single crystal.

# CHAPTER VI
# A THERMODYNAMICAL FRAMEWORK FOR MAGNETIC FIELD-INDUCED PHASE TRANSFORMATION

In this chapter, a thermodynamical framework based on the thermodynamics of thermoelastic martensitic phase transformations to better understand the energy contributions for the magnetic field-induced phase transformation will be discussed. The Gibbs free energy difference between the parent and product phases during a thermoelastic martensitic transformation can be expressed as [102];

$$\Delta G_{total}^{P\to M}(T,\sigma) = \Delta G_{ch}^{P\to M} - \Delta E_{mech}^{P\to M} + \Delta G_{el}^{P\to M} + \Delta E_{irr} \tag{6.1}$$

where $\Delta G_{total}^{P\to M}(T,\sigma)$ is the total Gibbs free energy difference that needs to be less than zero to trigger the transformation; $\Delta G_{ch}$ is the chemical free energy difference between martensite and parent phases (P→M represents the direction of the transformation, *i.e.* from parent phase to martensite); $\Delta E_{mech}$ is the mechanical energy provided by the externally applied load during the phase transformation; $\Delta G_{el}$ is the stored elastic energy; and $\Delta E_{irr}$ is the dissipation energy due to defect and dislocation generation and frictional energy spent on the movement of phase fronts. $\Delta G_{el}$ and $\Delta E_{irr}$ are also referred to as non-chemical energy terms. The chemical free energy difference can be expressed as

$$\Delta G_{ch}^{P\to M}(T) = \Delta H_{enthalpy} - T.\Delta S = G_{ch}^{M} - G_{ch}^{P} \tag{6.2}$$

where $\Delta H_{enthalpy}$ and $\Delta S$ are the change in enthalpy and entropy, respectively, upon transformation. $G_{ch}^{M}$ and $G_{ch}^{P}$ are the chemical free energies of martensite and parent phase.

Figure 6.1 shows the chemical free energies of austenite and martensite as a function of temperature. Gibbs free energy curves are presented straight assuming $\Delta H$ and $\Delta S$ are independent of temperature.

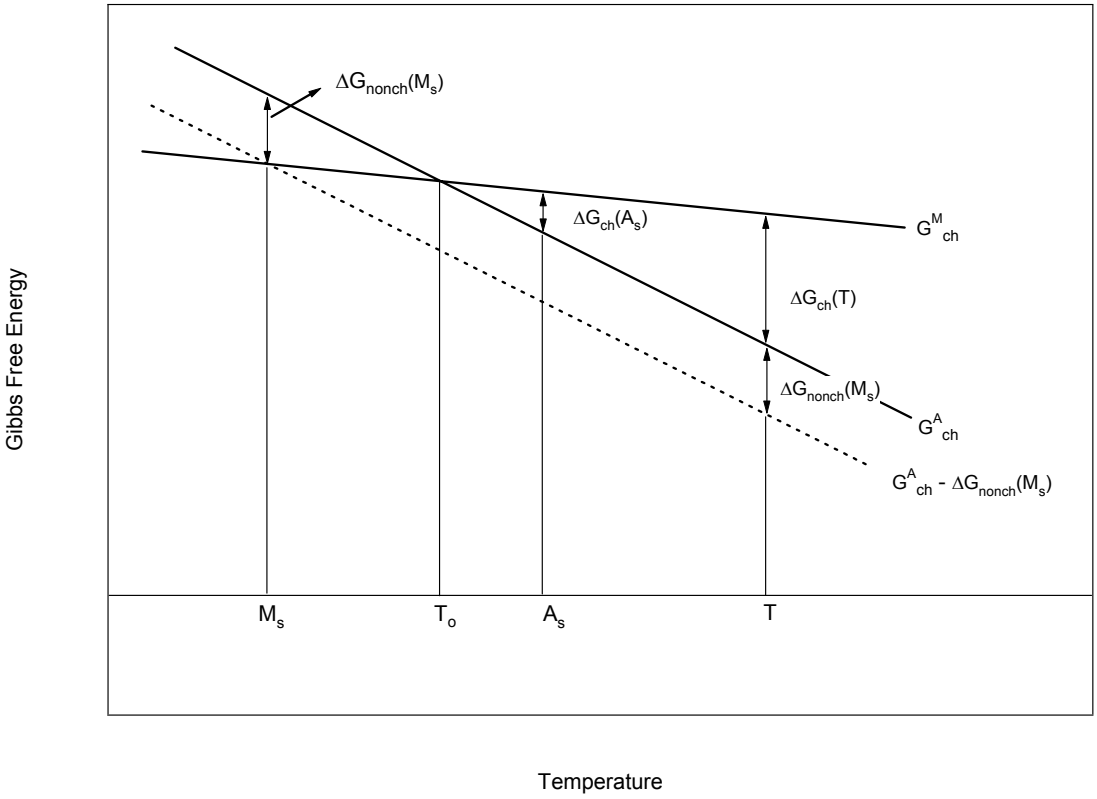


**Figure 6.1** The chemical free energies of austenite and martensite phase as a function of temperature. Gibbs free energy curves are presented straight assuming ΔH and ΔS are independent of temperature.

The equilibrium temperature, To is defined as the temperature where $\Delta G_{ch}^{P\to M}(T_O)=0$. However the transformation does not start at $T=T_o$ because more chemical energy is needed to overcome the friction and elastic energies as shown in Equation 6.1. When the sample temperature is equal to $M_s$ under no mechanical stress, transformation from austenite to martensite occurs and the Equation 6.1 becomes;

$$0=\Delta G_{total}^{P\to M}(M_s)=\Delta G_{ch}^{P\to M}(M_s)+\Delta G_{el}^{P\to M}+\Delta E_{irr}$$

$$\Delta G_{ch}^{P\to M}(M_s)=-\Delta G_{el}^{P\to M}-\Delta E_{irr}=\Delta G_{nonch}^{P\to M}(M_s) \qquad (6.3)$$

In the presence of an external magnetic field, one can modify the Equation 6.1 as follows;

$$\Delta G_{total}^{P\rightarrow M}(T,H) = \Delta G_{ch}^{P\rightarrow M} - \Delta E_{mech}^{P\rightarrow M} + \Delta G_{el}^{P\rightarrow M} + \Delta E_{irr} - \Delta G_{mag}^{P\rightarrow M} + \Delta G_{MAE}^{P\rightarrow M} \qquad (6.4)$$

In the above equation $\Delta G_{mag}$ represents the magnetic driving energy due to the difference between the saturation magnetizations of martensite and parent phase *i.e.* Zeeman energy difference as shown by Equation 4.4. $\Delta G_{mag}^{P\rightarrow M}$ term has a negative sign in Equation 6.4 because the available Zeeman energy difference provides additional energy to overcome the chemical energy difference between transforming phases similar to external mechanical work. This term is more pronounced when the transformation occurs between a paramagnetic parent phase and a ferromagnetic martensite (or vice versa). $\Delta G_{MAE}^{P\rightarrow M}$ is the difference between the magnetocrystalline anisotropy energies of martensite and parent phase and given by Equation 4.3. $\Delta G_{MAE}^{P\rightarrow M}$ term has a positive sign in Equation 6.4 since it represents another energy storage contribution to total free energy similar to $\Delta G_{el}^{P\rightarrow M}$. Magnetoelastic effects can be taken into account in the $\Delta G_{el}^{P\rightarrow M}$ term in Equation 6.4, however, they are usually negligible as compared to $\Delta G_{mag}^{P\rightarrow M}$ and $\Delta G_{MAE}^{P\rightarrow M}$ [58, 103].

The two separate magnetic energies can oppose or help each other depending on the saturation magnetization and MAE differences of the phases, which can be controlled with compositional modifications and temperature. In addition, the lattice correspondence between parent and martensite phases plays a role in dictating the magnitude of $\Delta G_{MAE}^{P\rightarrow M}$. If $-\Delta G_{mag}^{P\rightarrow M} + \Delta G_{MAE}^{P\rightarrow M}$ is positive, then the parent phase is more stable under a magnetic field, in other words, a magnetic field can be used to trigger the martensite to parent phase transformation. If it is negative, the parent to martensite phase transformation can be activated with application of a magnetic field. It is also possible to maximize or minimize $\Delta G_{MAE}^{P\rightarrow M}$ by simultaneously applying an external stress and a magnetic field. This requires the selection of favorable field and axial stress directions such that the stress would orient the easy magnetization axis of martensite

perpendicular or parallel to the applied field direction upon phase transformation. For example, simultaneous application of the field and compressive stress perpendicular to each other in NiMnGa MSMAs, depending on the relationship between magnetic easy axis and martensite twinning crystallography), would maximize $(K_u \sin\theta)_{martensite}$ because the stress would bias the martensite twin variant upon phase transformation with $\theta = 90^\circ$. In summary, $\Delta G_{mag}^{P\rightarrow M}$ mainly depends on composition and temperature, and $\Delta G_{MAE}^{P\rightarrow M}$ depends also on the crystallographic direction of the applied stress and the magnetic field, and the lattice correspondence between the transforming phases.

Figure 6.2 illustrates four schematics for the available magnetic energy contributions for three specific and one more general conditions to observe MFIS via either field-induced martensite variant reorientation or phase transformation in magnetic shape memory alloys. In Figure 6.2.a, the magnetization response of martensite along the easy and hard axes is shown where the area between these two extreme responses is defined as $K_u$, the maximum magnetocrystalline anisotropy energy. $K_u$ is the magnetic energy term which is responsible for field-induced variant reorientation of martensite as in NiMnGa and FePd alloys [8, 26, 104]. Figure 6.2.b shows the case when MAE of transforming phases are negligible and there is a difference in saturation magnetizations of the parent and martensite phases. This is the case for NiMn(In,Sn) alloy systems where ferromagnetic austenite transforms to paramagnetic or antiferromagnetic martensite [14, 53, 54]. The only available energy term is the Zeeman energy due to the difference in saturation magnetizations of the transforming phases as shown by the shaded area in Figure 6.2.b. The third case shown by Figure 6.2.c corresponds to the present case of the stress-assisted field-induced phase transformation in NiMnGa alloys where saturation magnetizations of both transforming phases are equal and MAE of martensite is not negligible as opposed to the MAE of the parent phase. In this case, MAE is the only available magnetic energy term that can be utilized for field-induced phase transformations. Figure 6.2.d represents a more general, arbitrary case with transforming phases having notably different MAEs and saturation magnetizations, in which the shaded area shows the available magnetic energy for the field-induced phase

transformation. At this point, it should be noted that MAE does not increase with magnetic field after the field reaches to a critical level for saturation, however, Zeeman energy term does not consist of any limiting field level and increases continuously with applied magnetic field. Moreover, Zeeman energy does not usually depend on the relationship between the orientations of the crystal and the applied magnetic field direction, thus, it can be utilized to easily trigger phase transformation in polycrystals as well.

Figure 6.3 shows a schematic of the change in Gibbs free energies of parent phase and martensite as a function of temperature considering the effect of an applied magnetic field. This schematic is constructed specifically for $Ni_2MnGa$, however, the contribution of magnetic energy terms on the total energy might be different in other alloy systems as described below. Assuming $\Delta G_{MAE}^{P\rightarrow M}$ is positive, *i.e.* the MAE of martensite is higher than the MAE of the parent phase, and the saturation magnetization difference (or $\Delta G_{mag}^{P\rightarrow M}$) is negligible, thus the total free energy of martensite would shift upward. This results in a new equilibrium and the $M_s$ temperature under a magnetic field ($M_s(H)$) is lower than the $M_s$ without field as shown in the figure. This appears to be the case in the present alloy for the I→X, I→10M, P→10M phase transformations in a certain temperature range since a decrease in $M_s$ also means an increase in the critical stress level for the parent to martensite phase transformation at a given temperature.

Similarly, if $\Delta G_{MAE}^{P\rightarrow M}$ is negative, then the total free energy curve would shift downward. If $\Delta G_{mag}^{P\rightarrow M}$ is positive while $\Delta G_{MAE}^{P\rightarrow M}$ is negligible, then the shift would be again downward. The downward shift means that the new $M_s$ is at a higher temperature ($M_s^*(H)$, Figure 6.3). If both MAE and saturation magnetization differences play a role, then the Gibbs free energy would change by $\Delta G_{MAE}^{P\rightarrow M}$ - $\Delta G_{mag}^{P\rightarrow M}$ and $M_s$ would be between $M_s(H)$ and $M_s^*(H)$. Note that although MAE and saturation magnetizations are temperature dependent, we have assumed temperature independence in the schematic for simplicity.

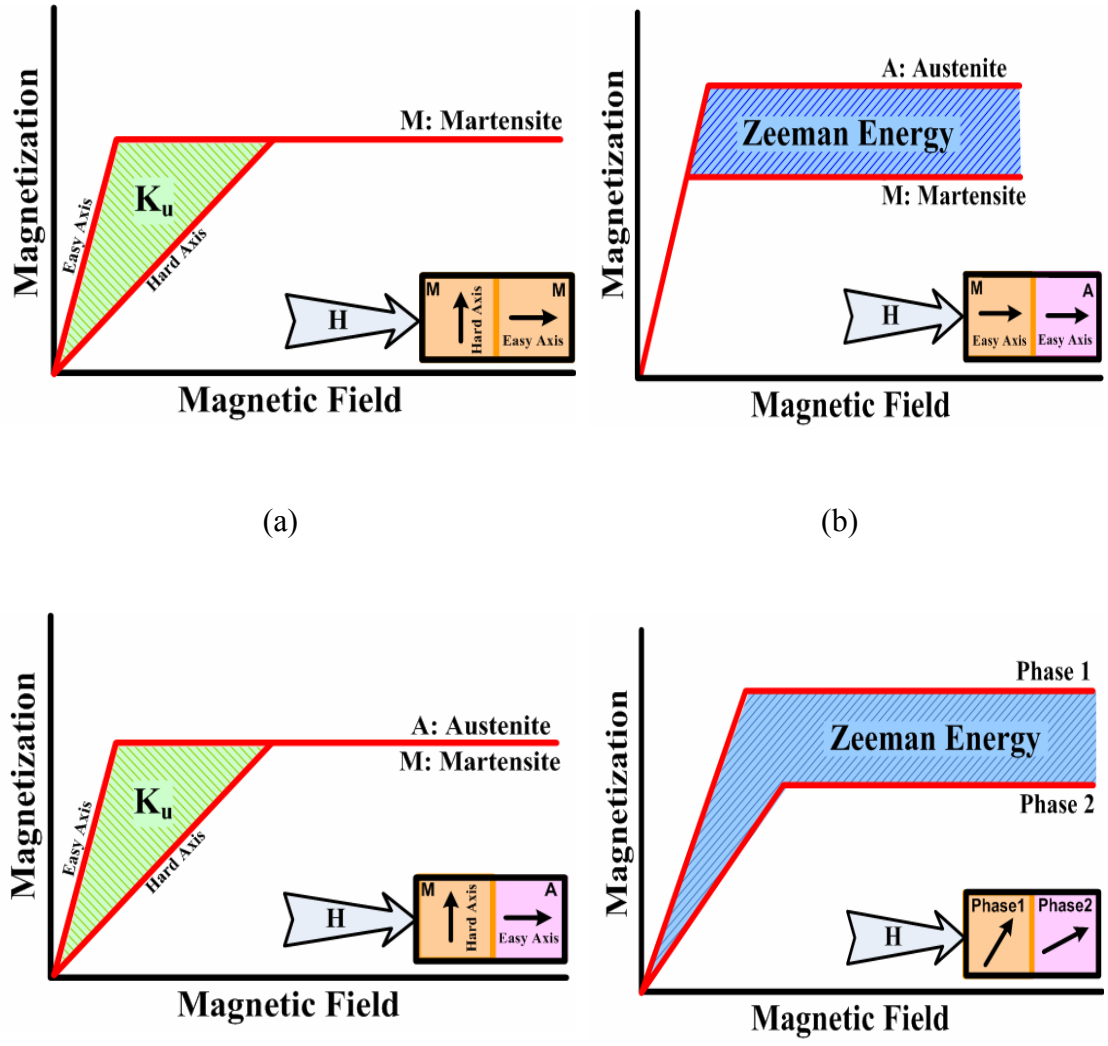


**Figure 6.2** Schematics of possible magnetization vs. applied magnetic field responses and illustration of available magnetic energy contributions for four possible cases in magnetic shape memory alloys, a) martensite variant reorientation as in NiMnGa, b) field-induced phase transformation as in NiMnCoIn alloys, c) stress-assisted field-induced phase transformation as in the present NiMnGa alloys, and d) a more general case for field-induced phase transformation between two phases with different saturation magnetizations and magnetocrystalline anisotropy energies.

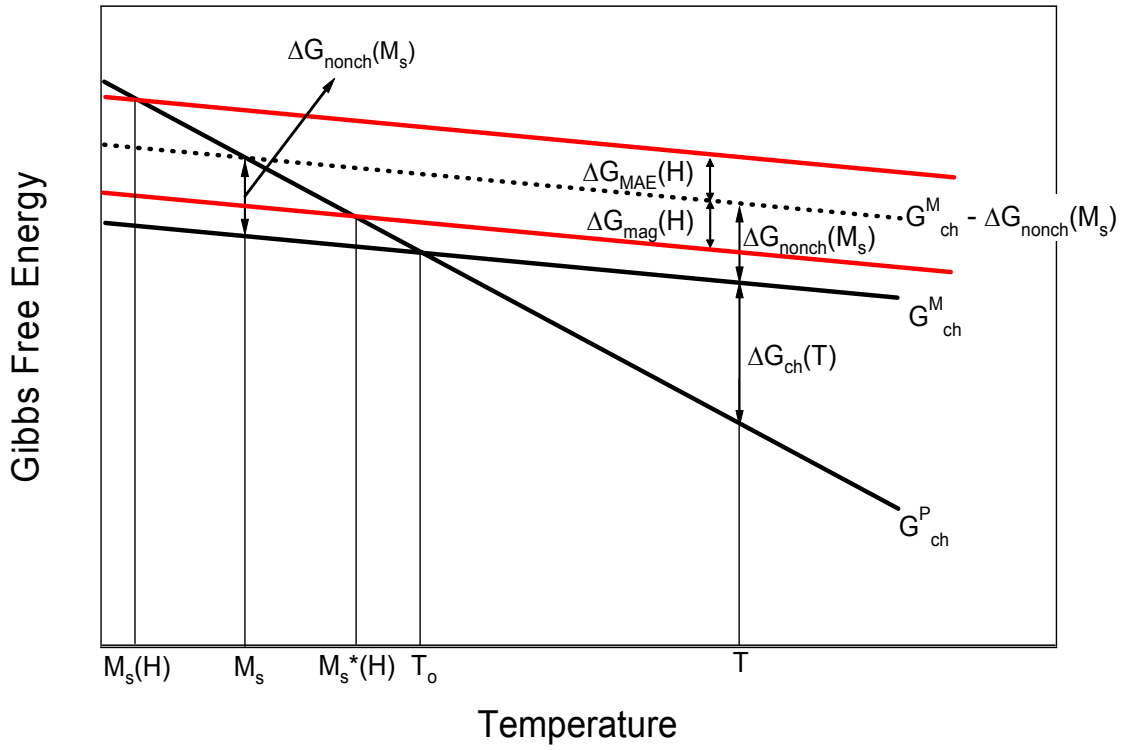


**Figure 6.3** Gibbs free energy curves of parent and martensite phases of NiMnGa alloy as a function of temperature considering the effect of magnetic energy contributions.

For the stress-induced martensitic transformation and pseudoelasticity, the mechanical energy required for forward and recovered from reverse transformations with and without a magnetic field at a temperature above the equilibrium temperature can be written with the help of this schematic as:

$$\Delta E_{mech}^{P\to M}(T,H) = \Delta G_{ch}^{P\to M} + \Delta G_{el}^{P\to M} + \Delta E_{irr} - \Delta G_{mag}^{P\to M} + \Delta G_{MAE}^{P\to M} \quad (6.5)$$

$$\Delta E_{mech}^{M\to P}(T,H) = \Delta G_{ch}^{M\to P} + \Delta G_{el}^{M\to P} + \Delta E_{irr} - \Delta G_{mag}^{M\to P} + \Delta G_{MAE}^{M\to P} \quad (6.6)$$

$$\Delta E_{mech}^{P\to M}(T,0) = \Delta G_{ch}^{P\to M} + \Delta G_{el}^{P\to M} + \Delta E_{irr} \quad (6.7)$$

$$\Delta E_{mech}^{M\to P}(T,0) = \Delta G_{ch}^{M\to P} + \Delta G_{el}^{M\to P} + \Delta E_{irr} \quad (6.8)$$

In these equations, the difference between the required mechanical energies for the onset of the forward transformation with and without magnetic field stems from the

available magnetic energies assuming that the magnetic field does not significantly effect the dissipation and stored elastic energy. Considering that the supplied mechanical energy can be expressed in terms of the stress level and transformation strain in case of no hardening, this difference can be written as,

$$\Delta E_{mech}^{P\to M}(T,H) - \Delta E_{mech}^{P\to M}(T,0) = -\Delta G_{mag}^{P\to M} + \Delta G_{MAE}^{P\to M}$$

$$\sigma_{c,forward}^{H}.\varepsilon_o - \sigma_{c,forward}.\varepsilon_o = -\Delta G_{mag}^{P\to M} + \Delta G_{MAE}^{P\to M} \tag{6.9}$$

where $\varepsilon_o$ is the transformation strain which is about the same with and without magnetic field (Chapter IV). Then, the magnetostress ($\sigma_{mag}$) can be expressed as

$$\sigma_{mag} = \sigma_{c,forward}^{H} - \sigma_{c,forward} = \frac{-\Delta G_{mag}^{P\to M} + \Delta G_{MAE}^{P\to M}}{\varepsilon_o} \tag{6.10}$$

For the reversible field-induced phase transformation to take place, the recovered mechanical energy upon reverse transformation under magnetic field ($\sigma_{c,reverse}^{H}.\varepsilon_o$) should be more than the required mechanical energy for forward transformation under zero field ($\sigma_{c,forward}.\varepsilon_o$). Then, the energy condition for the reversible field-induced phase transformation can be written as;

$$\Delta E_{mech}^{M\to P}(T,H) + \Delta E_{mech}^{P\to M}(T,0) = 2\Delta E_{irr} - \Delta G_{mag}^{M\to P} + \Delta G_{MAE}^{M\to P} > 0 \tag{6.11}$$

which results in the following universal criterion

$$-\Delta G_{mag}^{P\to M} + \Delta G_{MAE}^{P\to M} > 2\Delta E_{irr} \tag{6.12}$$

From Equation 6.12, the magnetostress requirement can be written, by dividing both sides with the phase transformation strain, as

$$\sigma_{mag} > 2\sigma_{friction} = \Delta\sigma_{hys} \tag{6.13}$$

where $\sigma_{friction}$ is frictional stress against the motion of martensite-parent phase interface and $\Delta\sigma_{hys}$ is the pseudoelastic stress hysteresis ($\sigma_{c,forward} - \sigma_{c,reverse}$).

For the NiMnGa alloy, the difference between the saturation magnetizations of the martensite and parent phase where the parent phase is the I-phase and the MAE of the I phase are negligible [95]. Therefore, $\sigma_{mag}$ arises only from the MAE of martensite

(X or 10M phases) in the present case up to -20 °C. The MAE of martensite ($K_u$) was found to be 3.30 x$10^5$ J/$m^3$ at -95 °C for the present single crystals. If we use this $K_u$ with a total transformation strain of 3.8 % for both transformation stages, then the magnetostress can be calculated as 8.7 MPa using Equation 6.10, which is close to the experimentally observed values of 7 MPa.

The positive magnetostress means that the parent phase (I-phase) is more stable under a magnetic field than both the X and 10M martensite phases, *i.e.* the field suppresses the $M_s$ temperature. Since the magnetostress increases up to 1 Tesla for both transformation stages and then saturates, the transformation temperatures should follow a similar trend. In other words, they should drop up to an applied magnetic field of 1 Tesla and then stay constant with further increase in magnetic field provided that $\Delta G_{mag}^{P\rightarrow M}$ is negligible. Indeed, the recent results by Kim *et al.* [95] showing the effect of a magnetic field on the $M_s$ temperature of $Ni_2MnGa$ as a function of transforming phase structures and field level support the general trends observed in this work for the I→X, I→10M, and P→10M phase transformations.

As temperature increases, the MAE of martensite decreases due to the decrease in the saturation magnetization [13]. Moreover, there is a difference between the saturation magnetizations of the parent phase (P phase) and martensite (10M) at higher temperatures [95]. For example, Heczko and Straka [13] reported a 15% difference in saturation magnetizations of stress-induced martensite and parent phase at room temperature. Thus, the decrease in MAE of martensite and the increase in the difference between saturation magnetizations of transforming phases in the present case resulted in vanishing magnetostress at 10 ˚C for the P→10M transformation . In other words, $\Delta G_{MAE}^{P\rightarrow M} - \Delta G_{mag}^{P\rightarrow M}$ became negligible.

It was shown for a polycrystalline NiMnGa MSMA that the applied field had a small effect on the transformation temperatures if the parent phase is ferromagnetic [54] demonstrating that $\Delta G_{MAE}^{P\rightarrow M} - \Delta G_{mag}^{P\rightarrow M}$ is small. An increase in transformation temperatures with magnetic field was reported when the paramagnetic parent phase

transforms to ferromagnetic martensite [95] emphasizing the effect of $\Delta G_{mag}^{P\rightarrow M}$. The field-induced parent phase stabilization (decrease in $M_s$) reported by Murray *et al.* [46] and field-induced martensite stabilization (increase in $M_s$) reported by Jeong *et al.* [36] on NiMnGa polycrystals under stress could, then, be due to the ferromagnetic parent phase in the former and the paramagnetic parent phase in the latter study.

In NiMnCoIn alloys, the transformation temperatures decrease with applied field when ferromagnetic austenite transforms to paramagnetic martensite or martensite with lower saturation magnetization. The decrease in transformation temperatures is due to the large negative $\Delta G_{mag}^{P\rightarrow M}$ and negligible MAE of the parent and martensite phases or small MAE of martensite. In other words, $\Delta G_{MAE}^{P\rightarrow M}$ - $\Delta G_{mag}^{P\rightarrow M}$ becomes very large. In this case, both the MAE and $\Delta G_{mag}^{P\rightarrow M}$ terms result in stabilization of austenite. Figure 6.4 shows a schematic of the change in Gibbs free energies of parent phase and martensite as a function of temperature considering the effect of an applied magnetic field in the NiMnCoIn alloy. Both the MAE and $\Delta G_{mag}^{P\rightarrow M}$ can be considered as additions to the free energy of martensite.

In the pseudoelastic experiments, the large $\Delta G_{MAE}^{P\rightarrow M}$ - $\Delta G_{mag}^{P\rightarrow M}$ value results in large and continuous shift in critical stress for phase transformation with applied field. Additionally, $\Delta G_{MAE}^{P\rightarrow M}$ is limited to a critical field where the saturation magnetization along the hard axes reaches to saturation magnetization, however there is no limit for $\Delta G_{mag}^{P\rightarrow M}$ as far as there is a difference between the saturation magnetization of austenite and martensite phases. This suggests that for any temperature it might be possible to separate the pseudoleastic loops in NiMnCoIn alloys and observe reversible stress-assisted field-induced phase transformation provided that test temperature is below the Curie Temperature. The key point here is to decrease the critical field for this reversible phase transformation.

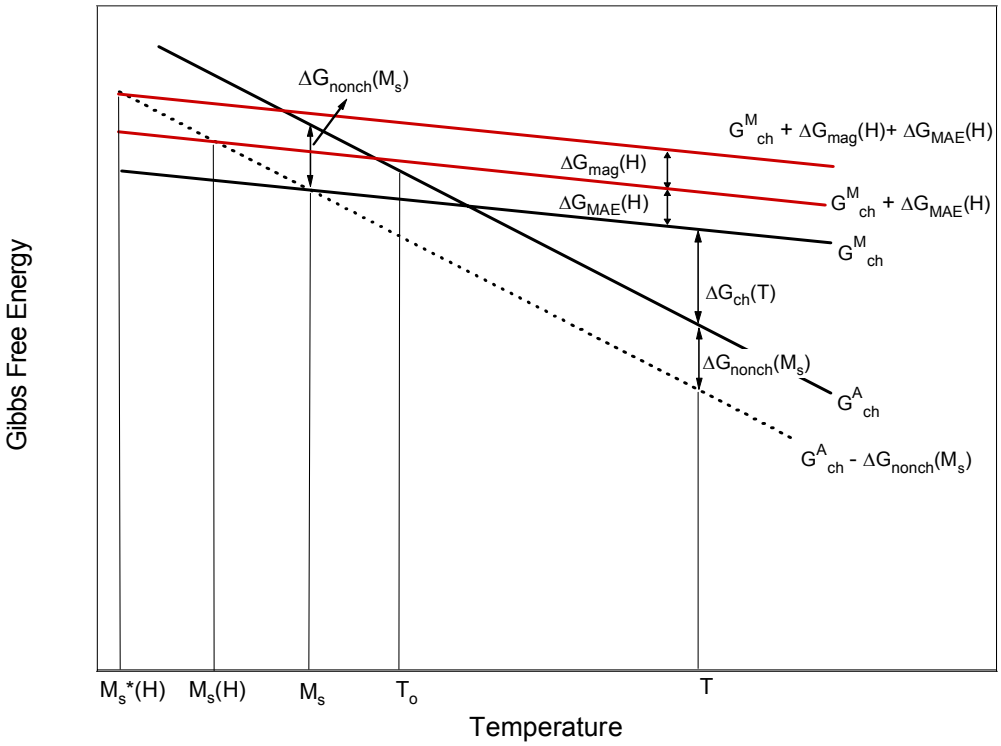


**Figure 6.4** Gibbs free energy curves of parent and martensite phases of the NiMnCoIn alloy as a function of temperature considering the effect of magnetic energy contributions.

It is clear in Equations 6.12 and 6.13 and from the above discussion that the stress range ($\sigma^{H}_{c,reverse} - \sigma_{c,forward}$) for reversible field-induced phase transformation can be increased by either increasing $\Delta G^{P\rightarrow M}_{MAE}$ - $\Delta G^{P\rightarrow M}_{mag}$, or decreasing dissipation (*i.e.* pseudoelastic stress hysteresis). $\Delta G^{P\rightarrow M}_{MAE}$ depends on temperature, applied magnetic field and stress directions with respect to the easy axis of magnetization and composition [13, 30] while pseudoelastic stress hysteresis depends on temperature, crystal orientation, loading type (tension vs. compression), composition, resistance to dislocation generation (matrix strength), compatibility between parent and martensite phase boundary and transformation strain. Similiarly, it is also possible to maximize $\Delta G^{P\rightarrow M}_{mag}$ by selecting a system where one of the transforming phases is paramagnetic as in the case of

NiMnCoIn. Clearly, there are many parameters that can be optimized to observe field-induced phase transformation, which makes this class of alloys promising candidates for future research.

One challenge, however, is to find alloys in which both magnetic energy terms promote the phase transformation instead of opposing each other. For example, if a composition is selected for transformation from a ferromagnetic austenite to paramagnetic martensite for maximizing $\Delta G_{mag}^{P\rightarrow M}$, $\Delta G_{MAE}^{P\rightarrow M}$ will always oppose $\Delta G_{mag}^{P\rightarrow M}$ if MAE of austenite is not negligible. In such a case, it is more desirable that $\Delta G_{MAE}^{P\rightarrow M}$ is negligible. Similarly, in transformations where $\Delta G_{MAE}^{P\rightarrow M}$ is large, then the parent phase usually has lower saturation magnetization than martensite making the $\Delta G_{mag}^{P\rightarrow M}$ contribution opposite to $\Delta G_{MAE}^{P\rightarrow M}$. Therefore, it is necessary to find alloy compositions that would maximize one of the magnetic energy terms while the other one is negligible for achieving wide stress ranges for reversible field-induced phase transformation.

In the above thermodynamics consideration, it has been assumed a very simple domain structure both in martensite and parent phases and suggested that the domain walls vanishes when a small magnetic field is applied. In other words, effects of the specimen size and shape effect, domain wall motion and demagnetization energy are neglected. This appears to be a valid approximation for NiMnGa alloys as suggested by O'Handley [8], but in other alloys the demagnetization energy should be taken into account in the Gibbs free energy formulation. Similarly, one could carefully determine the effect of temperature on $\Delta G_{MAE}^{P\rightarrow M}$ and $\Delta G_{mag}^{P\rightarrow M}$, and construct more accurate Gibbs free energy representation which is a challenging task. It is possible though to find out, indirectly and relatively more easily, the trends in the temperature dependence of the $\Delta G_{MAE}^{P\rightarrow M}$ - $\Delta G_{mag}^{P\rightarrow M}$ term either by determining the change in $M_s$ temperature under a magnetic field above the saturation field like Kim *et al.* [95] did or by determining the magnetostress as a function of temperature as in the present study.

# CHAPTER VII
# SUMMARY AND CONCLUSIONS

The magneto-thermomechanical response of the $Ni_2MnGa$ single crystals oriented along the [100] direction was investigated under the simultaneous application of external stress and magnetic field considering the effect of field cycles, temperature and field rate on the magnetic field induced strain, blocking stress and magnetostress, magnetoelasticity and magnetoplasticity. The magnetic field and external stress were applied perpendicular to each other. The present work demonstrated that magnetic field-induced phase transformation is possible in $Ni_2MnGa$ single crystals under low field magnitudes and the effect is repeatable under cyclic field applications. This mechanism can overcome the current limitations of MSMAs by easily increasing the actuation stress levels by at least one order of magnitude. The field-induced phase transformations and shape memory characteristics of NiMnCoIn alloys were also studied. High magnetostress levels are reported however reversible field-induced phase transformation can be only achieved under high magnetic fields. The following conclusions can be drawn from this study:

1. The maximum MFIS level is a function of constant bias stress. Increasing stress decreases the MFIS and no MFIS is observed above the blocking stress. The blocking stress in the present study was about 5 MPa two times higher than the maximum MFIS reported in the literature. The maximum MFIS was 5.8% which is close to the theoretical maximum reorientation strain for the 10M tetragonal martensite.
2. The cyclic MFIS evolution is different than the one observed during the first field cycle and significant irrecoverable MFIS may exist in the first cycle depending on the stress level. These were attributed to the competition between the stress and magnetic field favored martensite variants during the forward and backward reorientation. The MFIS in the first cycle is considerably higher than the one in the following cycles at low stress values.

3. The magnetic field rate has a significant effect on the MFIS evolution. At lower field rates (< 150 kG/sec), a rate dependent two stage reorientation was observed where the maximum MFIS magnitude increased with the field rate. This was attributed to the difference between the nucleation and propagation barrier strength for twins.
4. The stress induced martensite reorientation under constant magnetic field led to the observation of magnetoelasticity, i.e recoverable martensite reorientation, similar to the pseudoelasticity due to the recoverable stress induced phase transformation in conventional shape memory alloys. The constant magnetic field caused an increase in the stress levels during reorientation, i.e. magnetostress. The maximum magnetostress was 5.7 MPa in the present study, highest reported to date.
5. The high magnetostress (5.7 MPa), high blocking stress (5 MPa) and the maximum MFIS (5.8%) combination of this study is the highest reported to date for NiMnGa alloys with 10M martensite structure. This was a consequence of both the large gap between the operating temperature (-95 °C) and the Curie temperature and the small difference between the operating temperature and the martensite start temperature. The former leads to increase in the magnetocrystalline anisotropy energy and the latter provides low detwinning stress which are what is needed to maximize the blocking stress and magnetostress. The magnetocrystalline anisotropy energy was calculated to be $3.30 \times 10^5$ J/m$^3$ at -95 °C which was reported as $2.65 \times 10^5$ J/m$^3$ at room temperature.
6. A magnetic field applied perpendicular to the compressive stress increases the flow stress levels during the two-stage phase transformation. The magnetostress levels were on the order of 7 to 10 MPa. The pseudoelastic stress hysteresis loops with and without magnetic field were separated in the temperature range of -60 °C to -40 °C for the first stage transformation. The separation of the pseudoelastic loops with and without magnetic field was identified as the

necessary mechanical condition for the reversible field-induced phase transformation in MSMAs.

7. A magneto-microstructural mechanism is proposed to better understand the mechanisms responsible for the reversible field-induced phase transformations. The proposed mechanism can capture the evolution of magnetic field-induced strain vs. magnetic field response of the present alloy under constant stress during cyclic field applications.
8. Actuation stress and work output levels achieved by employing stress-assisted field-induced phase transformation in this study are more than one order of magnitude higher than the results previously reported for NiMnGa MSMAs.
9. The field-induced reversible phase transformation in NiMnCoIn alloys is determined by both measuring the change in magnetization and using high energy x-ray diffraction with *in situ* magnetic field capability. The required magnetic fields for reversible phase transformation were found to be high (>4 T) compared to field-induced variant reorientation and stress-assisted field-induced phase transformation in NiMnGa alloys (<1.5 T)
10. The crystal structure of austenite and martensite phases of NiMnCoIn single crystals used in this study is determined to be $L2_1$ and 12M, respectively. 12M structure is determined for the first time in NiMnCoIn alloys.
11. Theoretical transformation strains by CVP formation and detwinning are determined for NiMnCoIn alloys employing "Energy Minimization Theory". The transformation strains along the [100], [123] and [110] directions are 6.76 %, 4.15 % and 3.37 %, respectively for CVP formation. The detwinning strains along the [100], [123] and [110] orientations are calculated as 6.76 %, 4.59 % and 4.57 %, respectively.
12. Theoretical magnetostress levels for any direction can be calculated if the transformation strain and Classius-Clapeyron slope along the one orientation and rate of change of transformation temperatures with applied field are known. Theoretical calculation of magnetostress along the [100] orientation (21.6

MPa/Tesla) fits well to the experimental value (18.75 MPa/Tesla). The predicted magnetostress level along the [110] orientation is 43.5 MPa/Tesla for CVP formation.

13. A thermodynamical framework is developed considering the available magnetic energies to understand the magneto-mechanical conditions for reversible field-induced phase transformation. The Zeeman and magnetocrystalline anisotropy energies are responsible for the separation of the pseudoelastic hysteresis loops. The framework can be used to understand the energetics of the field dependence of transformation temperatures for any phase transformation.
14. Necessary magnetic and mechanical conditions, and materials design and selection guidelines are proposed to search for field-induced phase transformation in other ferromagnetic materials that undergo thermoelastic martensitic phase transformation. MAE, Zeeman energy, the differences between the TTs, Curie temperature and $T_o$, stress and temperature hysteresis, the lattice parameters of transforming phases, relative directions of applied magnetic field and stress, and stress state are important parameters for selection of new materials.

# REFERENCES


[1] Sozinov A, Likhachev AA, Lanska N, Ullakko K, Lindroos VK. Proceedings of SPIE 2002;4699:195.

[2] Henry CP, Bono D, Feuchtwanger J, Allen SM, Handley RCO. J Appl Phys 2002;91:7810.

[3] Murray SJ, Marioni MA, Kukla AM, Robinson J, O'Handley RC, Allen SM. J Appl Phys 2000;87:5774.

[4] Marioni MA, O'Handley RC, Allen SM, Hall SR, Paul DI, Richard ML, Feuchtwanger J, Peterson BW, Chambers JM, Techapiesancharoenkij R. J Magn and Magn Mater 2005;290-291:35.

[5] James RD, Wuttig M. Philos Mag A 1998;77:1273.

[6] Ullakko K, Huang JK, Kantner C, O'Handley RC, Kokorin VV. Appl Phys Lett 1996;69:1966.

[7] Mullner P, Chernenko VA, Kostorz G. J Magn and Magn Mater 2003;267:325.

[8] O'Handley RC. J Appl Phys 1998;83:886.

[9] Likhachev AA, Sozinov A, Ullakko K. Mater Sci Eng A 2004;378:513.

[10] Koho K, Vimpari J, Straka L, Lanska N, Soderberg O, Heczko O, Ullakko K, Lindroos VK. J de Phys IV 2003;112 II:943.

[11] Albertini F, Pareti L, Paoluzi A, Morellon L, Algarabel PA, Ibarra MR, Righi L. Appl Phys Lett 2002;81:4032.

[12] Vasil'ev AN, Bozhko AD, Khovailo VV, Dikshtein IE, Shavrov VG, Buchelnikov VD, Matsumoto M, Suzuki S, Takagi T, Tani J. Phys Rev B 1999;59:1113.

[13] Heczko O, Straka L. Mater Sci Eng A 2004;378:394.

[14] Kainuma R, Imano Y, Ito W, Sutou Y, Morito H, Okamoto S, Kitakami O, Oikawa K, Fujita A, Kanomata T, Ishida K. Nature 2006;439:957.

[15] O'handley RC. Modern Magnetic Materials: Principles and Applications. New York, NY: John Wiley & Sons, 2000.

[16] Schwartz M. Encyclopedia of Smart Materials. New York: Wiley-Interscience, 2002.

[17] Tzou HS, Lee HJ, Arnold SM. Mech Adv Mater Struct 2004;11:367.

[18] Faidley LE. Ph.D. Dissertation. The Ohio State University, 2006.

[19] Kellogg RA, Flatau AB, Clark AE, Wun-Fogle M, Lograsso TA. J Appl Phys 2002;91:7821.

[20] Cullity BD. Introduction to Magnetic Materials. Reading, MA: Addison-Wesley, 1972.

[21] Funakubo H. Shape Memory Alloys. Amsterdam: Gordon & Breach Publishing Group, 1987.

[22] Liu Y, Liu Y, Van Humbeeck J. Acta Mater 1998;47:199.

[23] Buehler WJ, Wiley RC, Gilfrich JV. J Appl Phys 1963;34:1475.

[24] Monner H. http://www.dlr.de/fa/PortalData/17/Resources/dokumente/ institut/2005/2005_01_nov_monner.pdf. Accessed 6/01/07

[25] Callister WD. Materials Science and Engineering: An Introduction. New York, NY: John Wiley & Sons, 2006.

[26] Tickle R. Ph.D. Dissertation. University of Minnesota; 2000.

[27] Callen HB, Callen E. J Phys and Chem Solids 1966;27:1271.

[28] Sozinov A, Likhachev AA, Ullakko K. IEEE Trans Magnetics 2002;38:2814.

[29] Zhao P. Ph.D. Dissertation. University of Maryland, 2006.

[30] Straka L, Heczko O, Ullakko K. J Magn and Magn Mater 2004;272-276:2049.

[31] James RD, Tickle R, Wuttig M. Mater Sci Eng A 1999;273-275:320.

[32] Likhachev AA, Sozinov A, Ullakko K. Proceedings of SPIE 2002;4699:553.

[33] Ge Y, Heczko O, Soderberg O, Lindroos VK. J Appl Phys 2004;96:2159.

[34] Pan Q, James RD. J Appl Phys 2000;87:4702.

[35] Likhachev AA, Sozinov A, Ullakko K. Journal De Physique. IV 2004;115:95.

[36] Kakeshita T, Takeuchi T, Fukuda T, Saburi T, Oshima R, Muto S, Kishio K. Mater Trans 2000;41:882.

[37] Muto S, Oshima R, Fujita FE. Scripta Metall 1987;21:465.

[38] Karaca HE, Karaman I, Lagoudas DC, Maier HJ, Chumlyakov YI. Scripta Mater 2003;49:831.

[39] Karaca HE, Karaman I, Chumlyakov YI, Lagoudas DC, Zhang X. Scripta Mater 2004;51:261.

[40] Oikawa K, Wulff L, Iijima T, Gejima F, Ohmori T, Fujita A, Fukamichi K, Kainuma R, Ishida K. Appl Phys Lett 2001;79:3290.

[41] Oikawa K, Ota T, Imano Y, Omori T, Kainuma R, Ishida K. J Phase Equilib Diffus 2006;27:75.

[42] Liu Y, Zhou WM, Qi X, Jiang BH, Wang WH, Chen JL, Wu GH, Wang JC, Feng CD, Xie HQ. Appl Phys Lett 2001;78:3660.

[43] Oikawa K, Ota T, Sutou Y, Ohmori T, Kainuma R, Ishida K. Mater Trans 2002;43:2360.

[44] Oikawa K, Ota T, Ohmori T, Tanaka Y, Morito H, Fujita A, Kainuma R, Fukamichi K, Ishida K. Appl Phys Lett 2002;81:5201.

[45] Imano Y, Omori T, Oikawa K, Sutou Y, Kainuma R, Ishida K. Mater Sci Eng A 2006;438-440:970.

[46] Murray SJ, Marioni M, Allen SM, O'Handley RC, Lograsso TA. Appl Phys Lett 2000;77:886.

[47] Sozinov A, Likhachev AA, Lanska N, Ullakko K. Appl Phys Lett 2002;80:1746.

[48] Heczko O, Sozinov A, Ullakko K. IEEE Trans on Magn 2000;36:3266.

[49] Hao XJ, Ohtsuka H. Mater Sci Forum, 2005; 475-479;301.

[50] Kakeshita T, Shimizu K, Funada S, Date M. Acta Metall 1985;33:1381.

[51] Shimizu Ki, Kakeshita T. ISIJ International 1989;29:97.

[52] Cherechukin AA, Dikshtein IE, Ermakov DI, Glebov AV, Koledov VV, Shavrov VG, Takagi T, Tulaikova AA. Int J Appl Electromagn Mech. 2001;14:405.

[53] Kainuma R, Imano Y, Ito W, Morito H, Sutou Y, Oikawa K, Fujita A, Ishida K, Okamoto S, Kitakami O, Kanomata T. Appl Phys Lett 2006;88.

[54] Oikawa K, Ito W, Imano Y, Sutou Y, Kainuma R, Ishida K, Okamoto S, Kitakami O, Kanomata T. Appl Phys Lett 2006;88.

[55] Chernenko VA, Pons J, Cesari E, Ishikawa K. Acta Mater 2005;53:5071.

[56] Brown PJ, Crangle J, Kanomata T, Matsumoto M, Neumann KU, Ouladdiaf B, Ziebeck KRA. J Phys Condens Matter 2002;14:10159.

[57] Murray SJ, Farinelli M, Kantner C, Huang JK, Allen SM, Handley RCO. J Appl Phys 1998;83:7297.

[58] Jeong S, Inoue K, Inoue S, Koterazawa K, Taya M, Inoue K. Mater Sci Eng A 2003;359:253.

[59] Webster PJ, Ziebeck KRA, Town SL, Peak MS. Philos Mag B 1984;49:295.

[60] Tickle R, James RD. J Magn and Magn Mater 1999;195:627.

[61] Mullner P, Chernenko VA, Kostorz G. Mater Sci Eng A 2004;387-389:965.

[62] Soderberg O, Straka L, Novak V, Heczko O, Hannula SP, Lindroos VK. Mater Sci Eng A 2004;386:27.

[63] Sozinov A, Likhachev AA, Ullakko K. Proceedings of SPIE 2001;4333:189.

[64] Wedel C, Itagaki K. J Phase Equilib 2001;22:324.

[65] Overholser RW, Wuttig M, Neumann DA. Scripta Mater 1999;40:1095.

[66] Khovailo VV, Takagi T, Vasilev AN, Miki H, Matsumoto M, Kainuma R. Phys Status Solidi A 2001;183:R1.

[67] Vasil'ev AN, Buche'nikov VD, Takagi T, Khovailo VV, Estrin EI. Physics-Uspekhi 2003;46:559.

[68] Chernenko VA. Scripta Mater 1999;40:523.

[69] Pons J, Chernenko VA, Santamarta R, Cesari E. Acta Mater 2000;48:3027.

[70] Soderberg O. Ph.D Dissertation. Helsinki University of Technology, 2004.

[71] Gonzalez-Comas A, Obrado E, Man?osa L, Planes A, Chernenko VA, Hattink BJ, Labarta A. Phys Rev B 1999;60:7085.

[72] Manosa L, Gonzalez-Comas A, Obrado E, Planes A, Chernenko VA, Kokorin VV, Cesari E. Phys Rev B 1997;55:11068.

[73] Chernenko VA, Pons J, Segui C, Cesari E. Acta Mater 2002;50:53.

[74] Kokorin VV, Chernenko VA, Cesari E, Pons J, Segui C. J Phys Condens Matter 1996;8:6457.

[75] Zheludev A, Shapiro SM, Wochner P, Tanner LE. Phys Rev B 1996;54:15045.

[76] Murakami Y, Yano T, Shindo D, Kainuma R, Oikawa K, Ishida K. Scripta Mater 2006;55:683.

[77] Sutou Y, Imano Y, Koeda N, Omori T, Kainuma R, Ishida K, Oikawa K. Appl Phys Lett 2004;85:4358.

[78] Wachtel E, Henninger F, Predel B. J Magn and Magn Mater 1983;38:305.

[79] Wang YD, Ren Y, Huang EW, Nie ZH, Wang G, Liu YD, Deng JN, Zuo L, Choo H, Liaw PK, Brown DE. Appl Phys Lett 2007;90.

[80] Krenke T, Duman E, Acet M, Wassermann EF, Moya X, Manosa L, Planes A, Suard E, Ouladdiaf B. Phys Rev B 2007;75.

[81] Vasil'ev A, Bozhko A, Khovailo V, Dikshtein I, Shavrov V, Seletskii S, Buchelnikov V. J Magn and Magn Mater 1999;196-197:837.

[82] Lynch CS. Acta Mater 1996;44:4137.

[83] Mullner P, Chernenko VA, Wollgarten M, Kostorz G. J Appl Phys 2002;92:6708.

[84] Kiefer B. Ph.D. Dissertation. Texas A&M University, 2006.

[85] Glavatska N, Glavatsky I, Ge Y, Lindroos VK. Journal De Physique. IV 2003;112:1009.

[86] Heczko O. J Magn and Magn Mater 2005;290-291:787.

[87] Likhachev AA, Sozinov A, Ullakko K. Proceedings of SPIE 2004;5387:128.

[88] Kato H, Sasaki K. Scripta Mater 2003;48:31.

[89] Sullivan MR, Chopra HD. Phys Rev B 2004;70:094427.

[90] Straka L, Heczko O. IEEE Trans Magn 2003;39:3402.

[91] Sozinov A, Likhachev AA, Lanska N, Soderberg O, Ullakko K, Lindroos VK. Mater Sci Eng A 2004;378:399.

[92] Kim JH, Fukuda T, Kakeshita T. Scripta Mater 2006;54:585.

[93] Brewer A. M.S Thesis: Texas A&M University, 2007.

[94] Wun-Fogle M, Restorff JB, Leung K, Cullen JR, Clark AE. Magnetics, IEEE Transactions on 1999;35:3817.

[95] Kim JH, Inaba F, Fukuda T, Kakeshita T. Acta Mater 2006;54:493.

[96] Fan J, Stoll WA, Lynch CS. Acta Mater 1999;47:4415.

[97] Sehitoglu H, Karaman I, Anderson R, Zhang X, Gall K, Maier HJ, Chumlyakov Y. Acta Mater 2000;48:3311.

[98] James RD, Hane KF. Acta Mater 2000;48:197.

[99] Cui J, Chu YS, Famodu OO, Furuya Y, Hattrick-Simpers J, James RD, Ludwig A, Thienhaus S, Wuttig M, Zhang ZY, Takeuchi I. Nature Mater 2006;5:286.

[100] Otsuka K. Wayman CM. Shape Memory Materials. Cambridge; New York: Cambridge University Press, 1998.

[101] Sehitoglu H, Jun J, Zhang X, Karaman I, Chumlyakov Y, Maier HJ, Gall K. Acta Mater 2001;49:3609.

[102] Wollants P, Roos JR, Delaey L. Prog Mater Sci 1993;37:227.

[103] Heczko O. J Magn and Magn Mater 2005;290-291 PART 2:846.

[104] Kakeshita T, Fukuda T. Mater Sci Forum, 2002; 394-395:531.

# VITA

Haluk Ersin Karaca, son of Muzaffer and Seyide Karaca and younger brother of Erdem Karaca, was born in Canakkale, Turkey in 1979. He graduated from Bogazici University, Department of Mechanical Engineering, in May 2001. In Fall 2001, he enrolled in Texas A&M University to pursue a graduate degree, where he worked under the guidance of Dr. Ibrahim Karaman. He completed his research and received a Master of Science in Mechanical Engineering in December of 2003. Following graduation, Haluk continued his studies at Texas A&M University as a Doctor of Philosophy candidate in the same department and received his Doctor of Philosophy degree in August 2007. During his graduate career, he continuously held a research assistantship. His research interests include characterization of magnetic shape memory alloys and microstructure-mechanical property relations in shape memory alloys. Haluk also had the opportunity to serve as a lecturer in Materials Science (MEEN 222) and as a teaching assistant in Principles of Materials Engineering (ENGR 213) and Materials and Manufacturing Selection in Design (MEEN 360) courses. During his study, he was an author of 13 journal publications and more than 15 conference presentations. Upon graduation he will be an Assistant Professor in the Mechanical Engineering Department at University of Kentucky. His permanent address is:

Hurriyet Mahallesi
Cami Sokak, No:22
16800
Orhangazi, Bursa, TURKEY
Email: karacahaluk@gmail.com